Symmetry breaking in Suspensions of Anisotropic Colloids

phase transitions, diffusion and effective interactions

ISBN: 978-94-6191-779-9

Symmetry breaking in Suspensions of Anisotropic Colloids

phase transitions, diffusion and effective interactions

Symmetriebreking in Suspensies van Anisotrope Colloïden:
faseovergangen, diffusie en effectieve interacties

(met een samenvatting in het Nederlands)

Proefschrift

ter verkrijging van de graad van doctor aan de Universiteit Utrecht op gezag van de rector magnificus, prof.dr. G.J. van der Zwaan, ingevolge het besluit van het college voor promoties in het openbaar te verdedigen op woensdag 26 juni 2013 des middags te 2.30 uur

door

Simone Belli

geboren op 2 april 1985 te Cles (Italië)

Promotoren: Prof. dr. ir. M. Dijkstra
Prof. dr. R.H.H.G. van Roij

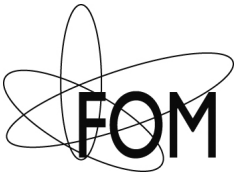

This work is part of the research programme of the Foundation for Fundamental Research on Matter (FOM), which is part of the Netherlands Organisation for Scientific Research (NWO).

Contents

Chapter 1
Introduction

Abstract

The aim of this chapter is to introduce the reader to the basic concepts of colloid science. By answering questions like "what are colloids?", "why do we study them?" and "how do we describe them?", we explain our interest in investigating symmetry breaking in equilibrium phases of anisotropic colloids.

1.1 Colloids

Explaining in a concise way what *colloids*, a.k.a. *colloidal particles*, are is always challenging. Due to their wide presence in everyday life, colloidal particles are often termed ubiquitous. Nevertheless, a precise definition is complicated for a number of reasons, among which the following three are the most evident examples.

First of all, if we wonder what colloids are made of, the answer is unsatisfactorily simple: everything. Of course, ultimately we can trace back their fundamental building blocks to atoms and molecules. However, atoms and molecules in colloidal particles appear in a variety of different forms [1–3]: as single very long molecules (polymers and proteins), small molecules arranging in loosely-bound composite structures (micelles and microemulsions), or even as atomic and molecular bulk equilibrium phases like gas (foams), liquid (aerosols, emulsions) and solid (sols). The latter will be the main subject of this thesis. In fact, the defining properties of colloids are not linked to their constituents, rather on their size. Colloids are stable aggregates of atoms and molecules whose size roughly varies between the nanometer (approximately the size of atoms and molecules) and the micrometer [4]. Therefore, ascertaining what colloids are made of does not help us understand what colloids are.

The second complication arises from the fact that colloids are never thought of in isolation. In fact, colloidal particles manifest their characteristic behavior only when they are dispersed in another phase, typically a molecular solvent like water.

Without the solvent, colloidal particles behave in a completely different and harder-to-describe way. The combined system of colloidal particles and solvent is therefore named *colloidal suspension* or *colloidal dispersion*.

Etymology provides the third and final complication in defining colloids. The term "colloid" comes from the Greek $\kappa o \lambda \lambda \alpha$, meaning "glue", and was coined by the Scottish chemist Thomas Graham in the 1860s. Graham was among the first who conducted systematic studies on colloidal suspensions, and proposed this name after observing the characteristic sticky behavior of some polymeric colloids [5]. However, the defining features of what we call now colloids have a conceptual meaning much deeper than that, a meaning which would have been unveiled only about 50 years after Graham's work [6–8]. Nonetheless, the term "colloid" survived.

So far we introduced colloids as aggregates of atoms and molecules with dimensions smaller than the micrometer suspended in a solvent. However, we have not yet explained what changes if the particles considered were bigger than the micrometer scale, nor have we addressed what occurs when we dispense with the solvent. The answers to those questions will give us the best way of understanding colloids and we will address them in the following sections. Nevertheless, before this is addressed it is worth examining the reasons why colloids are studied.

As previously mentioned, colloidal systems are ubiquitous in everyday life, therefore their study has strong practical motivations. Applications of colloid science range from food (mayonnaise, milk, jam) to cosmetics (creams and gels) and printing industry (ink, e-ink); from biology (blood, cell content) to medicine (controlled drugs release); from oil industry (extraction process) to agriculture (soil properties) and environmental science (air and water recovery) [1, 2].

However, the fundamental motivations behind colloidal science should not be underestimated. For reasons that will be made clearer in the following sections, in many ways colloids have properties resembling those of atoms, with the main difference that their size is appreciably bigger and their dynamics appreciably slower. Therefore, understanding colloids makes us understand the atomic and molecular world around us. Moreover, the physics of colloids can in a way be even more interesting than that of atoms and molecules. In fact, the mutual interactions between atoms and molecules are fixed and determined by their electronic structure. Instead, the interactions between colloids can be adjusted in different ways [9]: from isotropic to strongly *anisotropic*, from long to short range. Such a wide tunability of the interparticle interactions allows for the huge variety of the possible macroscopic colloidal assemblies.

1.2 Brownian motion and diffusion

Let us now address the important question we did not answer in the previous section: "why are the micrometer upper size limit and the presence of the solvent so relevant?" The quick answer is "because they are necessary conditions for the colloids to perform Brownian motion".

The physical phenomenon of Brownian motion takes its name from the Scottish botanist Robert Brown. Thanks to his pioneering use of the optical microscope, Brown was among the first who observed in 1827 the continuous and apparently chaotic motion of microscopic particles in water [10]. Although Brown himself ruled out that such a phenomenon could be related to the motion of microorganisms, its physical origin would not have been understood until 1905. In his *annus mirabilis* Albert Einstein [6], together and independently from the Australian physicist William Sutherland [7], showed that Brownian motion could be explained by the thermal equilibrium of the Brownian particles with the molecules of the surrounding solvent. In other words, the Brownian particles perform their chaotic motion as a consequence of the continuous exchange of momentum with the molecules of the solvent, which are in permanent thermal agitation. Such an explanation is clearly based on the kinetic theory of thermal systems, developed in the second half of the 19th century within a framework that would come to be called "statistical mechanics". A few years later the French physicist Jean Baptiste Perrin experimentally confirmed Einstein's theory [11], thus giving an unambiguous demonstration of the existence of atoms and the first strong validation of the kinetic theory.

In conclusion, small particles in a solvent perform a continuous chaotic motion, allowing them to *diffuse* all over the region of space occupied by the solvent. It is reasonable to expect that the bigger the mass, i.e., the size, of the Brownian particle, the less noticeable the effect of the solvent on its motion. This is what sets the approximate upper limit for the size of colloids. At room temperature the diffusion of particles with a size appreciably bigger than the micrometer is in practice negligible. In this case we do not talk about colloids anymore, but about granular matter. Now that we have seen that colloids are essentially particles that diffuse in a solvent, we will show what important consequences this brings to their physical description.

1.3 Statistical mechanics and effective interactions

One of the great achievements of 19th century physics was the development of *statistical mechanics* as a result of the remarkable insights of the Scot James Clerk Maxwell, the Austrian Ludwig Boltzmann and later on the American Josiah Willard Gibbs. Statistical mechanics is the branch of physics aimed at furnishing a description of systems composed by many (i.e., billions of billions of billions...) degrees of freedom [12–14]. The basic idea of its foundation consists of abandoning a deterministic description in terms of *microscopic* states, impossible in practice, in favor of a probabilistic one in terms of *macroscopic* states. The development of this theory followed from the need to unify within a single framework the microscopic dynamics of atoms and molecules, obeying Newtonian dynamics, with the then freshly developed ideas of thermodynamics.

In spite of the wide generality of the theory, there are precise conditions that limit the applicability of statistical mechanics. More specifically, the time evolution of the system must satisfy the "ergodic hypothesis". Roughly speaking, this means that the

system is supposed to occupy all the possible microscopic states within observation time [15]. Such an assumption has huge implications. This is because it allows the system to be described independently of its starting configuration, which for many-particle systems is practically impossible to know. Colloidal systems satisfy this condition thanks to the Brownian motion, and their equilibrium macroscopic (thermodynamic) behavior can be studied by means of the well-established concepts of statistical mechanics. On the other hand, this is not the case for granular matter, for which such a macroscopic description is at present impossible.

A further important feature of colloidal suspensions concerns the wide separation of the length and time scales characterizing the dynamics of the solvent and the colloids. This fact makes a global description of the suspension a complex task to achieve, since it should account for the superposition of effects developing on these very different scales. The typical approach aimed at a simplified statistical mechanical description of colloidal suspensions therefore involves a partial integration of the degrees of freedom of the solvent. This allows us to disentangle the effects related to the two basic length and time scales of the system. In practice, we forget about the solvent, while taking into account its presence only in terms of the *effective interactions* arising between the colloids [3].

Colloids experience various types of interactions. Among these, those that are purely repulsive and very short range are particularly important. These interactions can be realized experimentally by, e.g., coating the surface of the colloids with polymers [9]. In such cases we can model the colloid-colloid interaction as a hard repulsion, which is nothing but a non-overlap condition between the volumes of the colloids. The relevance of such models is due to the fact that energy (and therefore temperature) does not play any role, and the thermodynamics of the system is solely governed by the entropy. In other words, hard-body models allow to investigate the thermodynamics of colloids independently of energetic considerations. For this reason they have become a primary object of research in soft condensed matter [16].

1.4 Phase transitions and symmetry breaking

Now, let us leave for a moment colloidal suspensions and focus instead on something more familiar, like water. Water is a relatively simple system, since it is a collection of one single type of molecule, the water molecule H_2O. In spite of this apparent simplicity, we know well that water manifests a non-trivial macroscopic behavior. We experience everyday the fact that water can assume different states, or *thermodynamic phases*, with extremely different properties: *gas* (the vapor), *liquid* and *crystal solid* (the ice). We can achieve a *phase transition* between these very different states by modifying the thermodynamic state, that is, by bringing water below or above a given temperature (or pressure, density, ...). Even though there are not many other compounds whose full *phase behavior* we experience so much in our daily life, water is not an exception. Most of the systems composed by one single species of atoms or small molecules show similar phase transitions as water. The

statistical mechanical explanation for these phenomena is based on the fact that the equilibrium thermodynamic behavior of a system is determined only by the mutual interactions of its particles. The presence of gas, liquid and crystal phases follows from very general features, that is, that the pair interaction between two particles must have a short range repulsion and a long range attraction. This happens to be precisely the case for atoms and small molecules [9].

Let us focus more in detail on these phases of matter. If we could zoom into the atoms and molecules of a system in the gas or liquid phase, the only difference we would observe would be that in the liquid the particles are much closer to each other than in the gas. In both cases we would see the particles bouncing around in a chaotic manner, without showing any particular order in their average positions. This is because gas and liquid are actually a manifestation of the same phase, the *fluid*. The fluid is defined as a phase which is both *homogeneous* (its properties are the same in any point of the space) and *isotropic* (its properties are the same along any direction). On the other hand, gas and liquid strongly differ from the crystal phase, where particles tend to form ordered patterns in space (the crystal lattice), while rattling only a little around their preferred position. Due to the existence of these preferred positions, the crystal is an *inhomogeneous* and *anisotropic* phase. This implies that its structure is not symmetric with respect to an arbitrary translation or rotation. In this case we talk about translational and rotational spontaneous *symmetry breaking*. This crucial difference between fluid and crystal explains their extremely different properties, that is, for example, the ability of fluids to flow easily or the characteristic scattering patterns of electromagnetic radiation when interacting with a crystal.

The list of the possible phases of matter is not limited to fluid and crystal. So far, we implicitly thought that the only degrees of freedom of the particles were related to their positions. In other words, we assumed that the interaction between any couple of particles is isotropic and depends on their distance only. However, we can find in nature many examples of big enough molecules characterized by a strongly non-spherical distribution of atoms, and therefore by anisotropic interactions depending also on the molecular orientations. These molecules can develop phases whose properties are in between those of fluid and crystal and are therefore known as *mesophases* (meaning "phases in between"), or *liquid crystals* [17]. The characteristic feature of liquid crystals is that the spontaneous breaking involves only some of the spatial symmetries. In other words, the distribution of particles in a liquid-crystal phase is more ordered than in the fluid, but less than in the crystal. A typical example of liquid-crystal phase is the *nematic* phase, where particles tend to take preferred orientations in space, while developing no preference for the position of their centers of mass. The nematic phase is therefore anisotropic, like the crystal, and homogeneous, like the fluid. Other notorious examples of liquid-crystal phases are the *smectic* and *columnar* phases, where the positions of the particles tend to order only along one or two directions, respectively. Due to their peculiar properties, like that of flowing like a fluid while diffracting light like a crystal, liquid crystals have found wide industrial applications, especially in the fields of switching devices

and electro-optics [18].

At this point we can go back to the subject of this thesis, colloids. What do we expect from their macroscopic behavior? In the previous section we said that thanks to Brownian motion colloids behave like big atoms and molecules. Therefore, we deduce that they develop all the thermodynamic phases of atoms and molecules, that is, fluid, crystal and liquid crystals. However, unlike atoms and molecules, colloids have the great advantage that the features of their interactions can be manipulated with much more freedom. This gives the possibility to impose given properties on a macroscopic colloidal assembly by simply tailoring the interactions between its particles. As a consequence, understanding the relation between thermodynamic phases and interparticle interactions becomes a crucial problem of colloidal physics. This is the goal of this thesis.

1.5 Overview

The aim of this thesis is to shed new light on the properties of the equilibrium phases of anisotropic colloids in the presence of symmetry breaking. By referring to the colloids as anisotropic, we mean that they cannot be modeled simply as spherically symmetric particles. Consequently, the interaction between two such colloids is anisotropic and depends explicitly on their orientations in space. Throughout this thesis we model the colloids as hard bodies with a non-spherical shape, and we therefore focus on the role of entropic effects on their phase behavior. In Chapter 3 we study the effect of polydispersity on the liquid-crystal phase behavior of colloids having the shape of bricks (boardlike particles), and we compare it in Chapter 4 with that due to the effective attractive interaction induced by a non-adsorbing depletant. In Chapter 5 we analyze the crystallization transition of model colloidal hard cubes and squares. In Chapter 6 we focus on the effect of the broken symmetry on the diffusion and time relaxation of rod-like colloids. Finally, in Chapter 7 we propose a simplified theory for the description and prediction of the effective interactions between colloids induced by a solvent preferential adsorption.

Chapter 2
Theoretical framework

Abstract

One of the characteristic features of colloids is that their equilibrium many-particle properties can be studied by means of statistical mechanics. After a brief introduction to classical statistical mechanics, we describe in this chapter two methods aimed at its application: Density Functional Theory and Monte Carlo simulation.

2.1 Introduction

The description of a colloidal dispersion and the theoretical prediction of its properties represent a formidable challenge for physics. The origin of this high level of complexity stems essentially from two features: the multi-scale character of the microscopic dynamics and the macroscopic size of the system. The multi-scale character of the microscopic dynamics is a consequence of the heterogeneity of the particles composing the system. By definition, a colloidal suspension is comprised of two distinct classes of particles, "colloids" and "solvent", whose microscopic dynamics is characterized by extremely different length and time scales. On the other hand, the second source of complexity of a colloidal suspension, that is, its macroscopic size, implies that the properties of the system are determined in a non-trivial way by those of the *zillions* of particles that compose it.

Due to its multi-scale character, a faithful description of the dynamics of both solvent and colloidal particles composing a colloidal suspension is impossible in practice. By analogy, this would be almost like studying the trajectory of a cannon ball while taking into account the dynamics of each single molecule in the air. Therefore, a typical procedure aimed at simplifying the description consists of substituting the individual solvent molecules with a homogeneous medium, which affects the dynamics of the colloids only through a limited number of experimentally measurable macroscopic parameters (e.g., dielectric permittivity, shear viscosity,...) [1]. In other words, by means of a coarse graining process we approximate the two-component

system made by solvent and colloidal particles with a pure one-component system of colloidal particles with effective dynamics and interactions. These effective interactions depend on a few parameters characterizing the bulk properties of the pure solvent. This procedure is justified in many practical situations, when the dynamics of the colloids develops on length and time scales much larger than those of the solvent inhomogeneities and other effects, like hydrodynamic interactions, can be neglected.

Besides the multi-scale dynamics, the other element of complexity mentioned was the macroscopic size of a typical colloidal suspension. In general, understanding the behavior of a system composed of many particles in a deterministic way is an impossible task. However, there is a class of systems for which a coarse-grained description can be obtained. These systems are said to be *in equilibrium*, meaning that their state is independent of its previous history and fully determined by the value of a (limited) set of variables [13]. The theoretical tool developed to study equilibrium systems is *statistical mechanics*, which allows to determine the macroscopic thermal properties from the microscopic dynamics. This thesis focuses on the equilibrium properties of various model systems of colloidal dispersions, and classical statistical mechanics is the theoretical framework we will work in.

2.2 Fundamentals of statistical mechanics

2.2.1 Particles

In the context of this thesis the term "particle" will refer to both colloids and solvent molecules, but typically not at the same time. In fact, in the case our interest focuses on the thermodynamics of a colloidal suspension (Chapters 3-6), we use the term to refer to the colloids; the properties of the solvent are thought to be incorporated into the colloid-colloid interactions. On the other hand, in Chapter 7 we will be interested in explicitly evaluating the effective interaction between two colloids, in which case the microscopic degrees of freedom of the solvent will be considered explicitly. In the latter context, when talking about "particles", we refer to the solvent molecules.

In general, we will not assume the physical properties of the particles to be spherically symmetric. That means that the kinetics of a single particle must be described in terms of its center of mass position, given by the vector $\mathbf{r}$, and its orientation in space, expressed in terms of a set of angular variables $\boldsymbol{\Omega}$. For the sake of generality, it is convenient to introduce the concept of generalized coordinate $\mathbf{x} = (\mathbf{r}, \boldsymbol{\Omega})$, which is comprised of center-of-mass position and (when applicable) orientation coordinate.

2.2.2 Hamiltonian formulation of the microscopic dynamics

In the Hamiltonian formulation of classical mechanics, the dynamics of a system of N identical particles with generalized coordinates $\mathbf{X} = (\mathbf{x}_1, \ldots, \mathbf{x}_N)$ and corresponding

generalized momenta $\mathbf{P} = (\mathbf{p}_1, \ldots, \mathbf{p}_N)$ can be deduced by the Hamiltonian function

$$\mathcal{H}(\mathbf{X}, \mathbf{P}) \equiv \mathcal{K}(\mathbf{X}, \mathbf{P}) + \mathcal{U}(\mathbf{X}), \tag{2.1}$$

which corresponds to the total energy of the system decomposed into kinetic and potential energy contributions. For non-relativistic particles the kinetic term $\mathcal{K}$ takes the quadratic form [19]

$$\mathcal{K}(\mathbf{X}, \mathbf{P}) = \sum_{i=1}^{N} \frac{1}{2} \mathbf{p}_i^{\mathsf{T}} \, \mathbb{K}(\mathbf{x}_i) \, \mathbf{p}_i, \tag{2.2}$$

where the matrix $\mathbb{K}$, besides depending on some of the generalized coordinates $\mathbf{x}$, is determined by the mass m and the principal moments of inertia I_1, I_2 and I_3 [19]. The remaining term $\mathcal{U}$ in Eq. (2.1) represents the potential energy of the N-particle system.

It is useful to distinguish between the potential energy arising from the interaction between the particles of the system, which will be noted with U, and the potential energy $v(\mathbf{x})$ due to external fields. With this distinction, we can write the potential energy as

$$\mathcal{U}(\mathbf{X}) = U(\mathbf{X}) + \sum_{i=1}^{N} v(\mathbf{x}_i). \tag{2.3}$$

In this thesis we consider pairwise interactions only. Therefore, by denoting the interaction potential energy of particles i and j with $u(\mathbf{x}_i, \mathbf{x}_j)$, we can write

$$U(\mathbf{X}) = \sum_{i<j=1}^{N} u(\mathbf{x}_i, \mathbf{x}_j). \tag{2.4}$$

2.2.3 Ensemble probability density distribution

The statistical approach to the properties of a many-particle system consists of identifying the probability of a given microscopic state $(\mathbf{X}, \mathbf{P})$ under a set of constraints on the macroscopic variables $M_1, M_2, \ldots$. Once the probability density distribution $\mathcal{P}_{M_1 M_2 \ldots}(\mathbf{X}, \mathbf{P})$ is known up to a multiplicative constant, the expectation value of any microscopic variable $A(\mathbf{X}, \mathbf{P})$ for the system of interest at fixed value of $M_1, M_2, \ldots$ can be calculated as

$$\langle A \rangle_{M_1 M_2 \ldots} = \frac{\int d\mathbf{X} \, d\mathbf{P} \, A(\mathbf{X}, \mathbf{P}) \, \mathcal{P}_{M_1 M_2 \ldots}(\mathbf{X}, \mathbf{P})}{\int d\mathbf{X} \, d\mathbf{P} \, \mathcal{P}_{M_1 M_2 \ldots}(\mathbf{X}, \mathbf{P})}. \tag{2.5}$$

Probably the most important result of statistical mechanics states that an equilibrium system of N particles in a volume V in contact with a thermostat at absolute

temperature T ("canonical ensemble") has a probability density given by the Boltzmann distribution

$$\mathcal{P}_{TVN}(\mathbf{X},\mathbf{P}) \propto \exp\big[-\beta\mathcal{H}(\mathbf{X},\mathbf{P})\big], \tag{2.6}$$

where $\beta = (k_B T)^{-1}$ and $k_B = 1.3806488(13)\times 10^{-23} J K^{-1}$ is the Boltzmann constant.

2.2.4 Connection with thermodynamics

In the canonical ensemble the connection with the thermodynamics of the system can be made explicit by defining the partition function $Z(T,V,N)$ as

$$Z(T,V,N) \equiv \int \frac{d\mathbf{X}\,d\mathbf{P}}{h^{N d_p} N!}\ \exp\big[-\beta\mathcal{H}(\mathbf{X},\mathbf{P})\big], \tag{2.7}$$

where d_p is the number of degrees of freedom per particle, $h = 6.62606957(29)\times 10^{-34} J s$ is the Planck constant[1], and the factor $1/N!$ expresses the classical indistinguishability of the particles. In terms of the partition function the Helmholtz free energy is given by

$$F(T,V,N) = -\frac{1}{\beta}\log\big[Z(T,V,N)\big], \tag{2.8}$$

from the derivatives of which all the thermodynamic information can be deduced [13].

Due to the general form of the kinetic energy reported in Eq. (2.2), the integrand of Eq. (2.7) has a Gaussian dependence on the generalized momenta, which allows for an analytic solution. By performing such an integration [20], we can write the partition function as

$$Z(T,V,N) = \frac{Q(T,V,N)}{\mathcal{V}^N N!}, \tag{2.9}$$

where the *configuration integral* $Q(T,V,N)$ is defined as

$$Q(T,V,N) \equiv \int d\mathbf{X}\ \exp[-\beta\mathcal{U}(\mathbf{X})], \tag{2.10}$$

and the thermal volume $\mathcal{V}$ of a particle of mass m and principal moments of inertia I_1, I_2 and I_3 is given by

$$\mathcal{V} = h^6\sqrt{\frac{\beta^6}{(2\pi)^6 m^3 I_1 I_2 I_3}}. \tag{2.11}$$

[1] In a purely classical framework h is an unspecified parameter with units of [energy]×[time], introduced in order to make the partition function dimensionless. Since its effect on the energy is that of an additive constant, it does not influence any physical prediction. The precise value of h follows from a formulation of statistical mechanics based on a quantum microscopic dynamics.

In analogy with our considerations in the canonical ensemble, we can identify the connection between the Hamiltonian function and the relevant thermodynamic potential of other statistical ensembles. For the goals of this thesis, we report here the expression of the grand potential Ω of a system in a volume V at fixed temperature T and chemical potential μ ("grand canonical ensemble"), for which

$$\Omega(T,V,\mu) = -\frac{1}{\beta}\log\big[\Xi(T,V,\mu)\big], \tag{2.12}$$

where the grand canonical partition function is given by

$$\Xi(T,V,\mu) \equiv \sum_{N=0}^{\infty} \exp(\beta\mu N) Z(T,V,N), \tag{2.13}$$

or, using Eqs. (2.3), (2.9) and (2.10),

$$\Xi(T,V,\mu) = \sum_{N=0}^{\infty} \frac{1}{\mathcal{V}^N N!} \int d\mathbf{X} \, \exp\left\{-\beta U(\mathbf{X}) - \sum_{i=1}^{N} \beta\big[v(\mathbf{x}_i) - \mu\big]\right\}. \tag{2.14}$$

2.3 Density functional theory

2.3.1 Single-particle density

In the previous section we have seen that, once the ensemble probability density is known, we can calculate the expected value of any microscopic property $A(\mathbf{X},\mathbf{P})$ by means of Eq. (2.5). However, in many practical situations we are interested in microscopic properties that do not depend on the momenta and that can be expressed as sum of single particle properties, that is

$$A(\mathbf{X}) = \sum_{i=1}^{N} a(\mathbf{x}_i). \tag{2.15}$$

In this case, we can express the average value of Eq. (2.5) as

$$\left\langle \sum_{i=1}^{N} a(\mathbf{x}_i) \right\rangle = \int d\mathbf{x}\, a(\mathbf{x})\rho(\mathbf{x}), \tag{2.16}$$

where we introduced the single-particle density $\rho(\mathbf{x})$, defined as

$$\rho(\mathbf{x}) \equiv \langle \overline{\rho}(\mathbf{x}) \rangle, \tag{2.17}$$

where

$$\overline{\rho}(\mathbf{x}) = \sum_{i=1}^{N} \delta(\mathbf{x} - \mathbf{x}_i), \tag{2.18}$$

and $\delta(\mathbf{x} - \mathbf{x}_i)$ is the multi-dimensional Dirac-delta distribution. The average value of Eq. (2.17) is conveniently calculated in the grand canonical ensemble, from which we can deduce the following normalization condition

$$\int d\mathbf{x}\, \rho(\mathbf{x}) = \langle N \rangle. \tag{2.19}$$

An explicit way to evaluate the average value of Eq. (2.17) can be obtained as follows. By means of Eq. (2.18), we can rewrite the grand canonical partition function Eq. (2.14) as

$$\Xi(T, V, \mu) = \sum_{N=0}^{\infty} \frac{1}{\mathcal{V}^N N!} \int d\mathbf{X}\, \exp\left\{ -\beta U(\mathbf{X}) + \int d\mathbf{x}\, \beta\psi(\mathbf{x})\overline{\rho}(\mathbf{x}) \right\}, \tag{2.20}$$

with the *intrinsic chemical potential* defined as

$$\psi(\mathbf{x}) \equiv \mu - v(\mathbf{x}). \tag{2.21}$$

Note that the grand canonical partition function in Eq. (2.20) can be seen as a functional of $\psi(\mathbf{x})$, so that, by means of Eqs. (2.12) and (2.17), we can express the single-particle density as the functional derivative

$$\rho(\mathbf{x}) = -\frac{\delta\Omega}{\delta\psi(\mathbf{x})}. \tag{2.22}$$

2.3.2 Intrinsic free-energy functional

The result of Eq. (2.22) renders explicit the fact that the grand potential Ω can be considered as a function of T and V and a *functional* of the intrinsic chemical potential $\psi(\mathbf{x})$. However, the explicit evaluation of integrals of the type of Eq. (2.20) is impossible (or extremely difficult) in most cases, thus rendering the route to the single-particle density through Eq. (2.22) not feasible.

An alternative approach, which forms the basis of *density functional theory*, consists of inverting the relation of Eq. (2.22) and adopting the single-particle density as the functional variable rather than the intrinsic chemical potential [21]. This procedure has the great advantage of giving a higher control on the functional form of the single-particle density itself and on the approximations to adopt. In order to introduce the single-particle density as the functional variable, from Eq. (2.22) we define the Legendre transform $\mathcal{F}[\rho]$ of $\Omega[\psi]$ as

$$\mathcal{F}[\rho] \equiv \inf_{\psi(\mathbf{x})} \left\{ \Omega[\psi] + \int d\mathbf{x} \rho(\mathbf{x}) \psi(\mathbf{x}) \right\}, \tag{2.23}$$

which is the so-called *intrinsic free-energy functional*. Notice that the definition of Eq. (2.23) implies the definition of the single-particle density as given by Eq. (2.22). Since the Legendre transform of a function(al) is its own inverse, we can express the grand potential as

$$\Omega[\psi] = \inf_{\rho(\mathbf{x})} \left\{ \mathcal{F}[\rho] - \int d\mathbf{x} \rho(\mathbf{x}) \psi(\mathbf{x}) \right\}, \tag{2.24}$$

or, equivalently,

$$\Omega[\psi] = \inf_{\rho(\mathbf{x})} \left\{ \Omega_v[\rho] \right\}, \tag{2.25}$$

where $\Omega_v[\rho]$, which is a functional of both $v(\mathbf{x})$ and $\rho(\mathbf{x})$, is defined as

$$\Omega_v[\rho] \equiv \mathcal{F}[\rho] - \int d\mathbf{x} \rho(\mathbf{x}) \big[\mu - v(\mathbf{x}) \big]. \tag{2.26}$$

In other words, Eq. (2.25) states that the grand potential of a system of particles at temperature T and chemical potential μ in a volume V under the influence of the external field $v(\mathbf{x})$ is

$$\Omega = \Omega_v[\rho_{\text{eq}}]. \tag{2.27}$$

The equilibrium single-particle density $\rho_{\text{eq}}(\mathbf{x})$ is the one minimizing the functional $\Omega_v[\rho]$, and is therefore a solution[2] of the Euler-Lagrange equation

$$\left. \frac{\delta \Omega_v}{\delta \rho(\mathbf{x})} \right|_{\rho = \rho_{\text{eq}}} = 0. \tag{2.28}$$

It appears clear that the intrinsic free-energy functional $\mathcal{F}[\rho]$ defined in Eq. (2.23) is the relevant element in which all the information about the system is stored. It is therefore not surprising that in general we cannot calculate the functional dependence $\mathcal{F}[\rho]$ exactly. A great deal of work in density functional theory consists of developing approximations for $\mathcal{F}[\rho]$ and testing their quality for various model systems. It is convenient to write the intrinsic free energy as the sum of an ideal part and an excess part, where the latter is different from zero only for interacting systems, that is

$$\mathcal{F}[\rho] = \mathcal{F}^{\text{id}}[\rho] + \mathcal{F}^{\text{exc}}[\rho]. \tag{2.29}$$

The ideal component of the intrinsic free energy reads [21]

[2] In general not the only one, see the discussion in Sec. 2.3.3.

$$\mathcal{F}^{\mathrm{id}}[\rho] = \frac{1}{\beta}\int d\mathbf{x}\,\rho(\mathbf{x})\big\{\log[\mathcal{V}\rho(\mathbf{x})]-1\big\}. \tag{2.30}$$

By making use of the explicit expression for the ideal term of Eq. (2.30), the Euler-Lagrange equation Eq. (2.28) satisfied by the equilibrium single-particle density of a system at temperature T and chemical potential μ can be expressed as

$$\rho(\mathbf{x}) = \mathcal{V}^{-1}\exp\Big[\beta\mu-\beta v(\mathbf{x})+c_1(\mathbf{x},[\rho])\Big], \tag{2.31}$$

where we dropped the index "eq" for notational convenience and introduced the one-particle direct correlation function, which is a functional of the single-particle density and is defined as

$$c_1(\mathbf{x},[\rho]) \equiv -\beta\frac{\delta\mathcal{F}^{\mathrm{exc}}}{\delta\rho(\mathbf{x})}. \tag{2.32}$$

In summary, if an expression for the excess free-energy functional $\mathcal{F}^{\mathrm{exc}}[\rho]$ is known, by solving Eq. (2.31) we obtain a candidate for the equilibrium single-particle density at temperature T and chemical potential μ in the presence of the external field $v(\mathbf{x})$. The solution is only a "candidate" because satisfying Eq. (2.31) is a necessary but not sufficient condition for minimizing the functional $\Omega_v[\rho]$, as we will point out in the next section. The corresponding value for the grand potential is in turn calculated by inserting the solution of Eq. (2.31) into Eq. (2.26).

Alternatively, if we are interested in evaluating the single-particle density in the canonical ensemble, i.e., at fixed temperature T and number density $n = N/V$, Eq. (2.31) must be substituted with

$$\rho(\mathbf{x}) = \frac{n\exp\Big[\beta\mu-\beta v(\mathbf{x})+c_1(\mathbf{x},[\rho])\Big]}{\int\frac{d\mathbf{x}'}{V}\exp\Big[\beta\mu-\beta v(\mathbf{x}')+c_1(\mathbf{x}',[\rho])\Big]}, \tag{2.33}$$

which explicitly satisfies the normalization condition

$$\int d\mathbf{x}\,\rho(\mathbf{x}) = N. \tag{2.34}$$

Due to their highly non-linear character, both Eqs. (2.31) and (2.33) have to be solved numerically.

2.3.3 Bifurcation theory

In the previous section we have seen that the most important step of density functional theory consists of finding the function $\rho(\mathbf{x})$ that minimizes the functional $\Omega_v[\rho]$. In practice, this is achieved by solving the Euler-Lagrange equation Eq. (2.31) or Eq. (2.33). However, besides the absolute minimum (stable solution) of $\Omega_v[\rho]$, the Euler-Lagrange equation has in general more than one solution, representing local minima

(metastable solutions), saddle points and maxima (unstable solutions). In particular, the number of solutions of the Euler-Lagrange equation depends on the thermodynamic state. Typically, at low density or high temperature only one constant solution, corresponding to an isotropic and homogeneous (i.e., highly symmetric) macroscopic phase, exists. However, by varying the thermodynamic variables, we can encounter further solutions. These new solutions are often characterized by non-trivial modulations of the single-particle density in the orientation and/or position variables, and thus represent anisotropic and/or inhomogeneous phases (spontaneous symmetry breaking).

In practice, the identification of the equilibrium single-particle density for each thermodynamic state point is not always feasible. In fact, the numerical challenges related to the solution of the non-linear Euler-Lagrange equation increase with the number of dimensions along which the single-particle density is not homogeneous. This poses in principle a serious problem, since we would not be able to confirm the stability of a given phase, without comparing it with all other possible phases with lower symmetry, i.e., modulations along more dimensions. This problem can be bypassed by means of bifurcation theory, which focuses on the way in which new solutions of a given equation appear when its defining parameters are tuned. This theoretical tool has been introduced in the context of liquid-crystal phase transitions by Kayser and Raveché [22], and further developed by Mulder [23]. In this section we use bifurcation theory to estimate the maximum density at which a given phase can possibly be stable. In the language of Mulder, this coincides with identifying the first-order bifurcation equation [23].

In order for the equilibrium single-particle density $\rho(\mathbf{x})$ to be a minimum, as required by Eq. (2.25), besides solving the Euler-Lagrange equation, the concavity condition inequality

$$\int d\mathbf{x} d\mathbf{x}' \left.\frac{\delta^2 \mathcal{F}}{\delta\rho(\mathbf{x})\delta\rho(\mathbf{x}')}\right|_{\rho(\mathbf{x})} \delta\rho(\mathbf{x})\delta\rho(\mathbf{x}') > 0 \tag{2.35}$$

must be satisfied for an arbitrary choice of the function $\delta\rho(\mathbf{x})$. However, by modifying the thermodynamic state (i.e., by changing the temperature, density, etc...), the inequality Eq. (2.35) can continuously become an equality. If this is the case, what before was a minimum (stable solution) now becomes a saddle point (unstable solution), thus implying the existence of another absolute minimum separated from the original one. By introducing the two-particle direct correlation function

$$c_2(\mathbf{x}, \mathbf{x}', [\rho]) \equiv -\beta \left.\frac{\delta^2 \mathcal{F}^{\text{exc}}}{\delta\rho(\mathbf{x})\delta\rho(\mathbf{x}')}\right|_{\rho(\mathbf{x})}, \tag{2.36}$$

and using the explicit expression for the ideal free-energy functional given by Eq. (2.30), the limit of stability of a given solution $\rho(\mathbf{x})$ is found as the thermodynamic state at which a function $\delta\rho(\mathbf{x})$ exists, such that

$$\delta\rho(\mathbf{x}) = \rho(\mathbf{x}) \int d\mathbf{x}'\, c_2(\mathbf{x}, \mathbf{x}', [\rho]) \delta\rho(\mathbf{x}'). \tag{2.37}$$

Eq. (2.37) can be rewritten as the eigenvalue problem

$$\left(\frac{\delta\rho(\mathbf{x})}{\sqrt{\rho(\mathbf{x})}} \right) = \int d\mathbf{x}' \left[\sqrt{\rho(\mathbf{x})\rho(\mathbf{x}')} c_2(\mathbf{x}, \mathbf{x}', [\rho]) \right] \left(\frac{\delta\rho(\mathbf{x}')}{\sqrt{\rho(\mathbf{x}')}} \right), \tag{2.38}$$

where the integral operator between the square brackets is Hermitean, and hence has a spectrum of real eigenvalues. In summary, the limit of stability of a phase described by the single-particle density $\rho(\mathbf{x})$ is found as the thermodynamic state at which the matrix between square brackets in Eq. (2.38) acquires a unit eigenvalue. The corresponding eigenfunction is then a possible solution for $\delta\rho(\mathbf{x})/\sqrt{\rho(\mathbf{x})}$. If a unit eigenvalue does not exist, the only solution of Eq. (2.38) is $\delta\rho(\mathbf{x}) \equiv 0$, and hence $\rho(\mathbf{x})$ is a stable solution. The great merit of bifurcation theory is that of giving information on a non-linear problem by means of the solution of a linear one.

2.3.4 Approximations

In this section we list the approximation schemes for the excess free-energy functional $\mathcal{F}^{\text{exc}}$ adopted in this thesis. In general, there is no specific rule for preferring one scheme with respect to another. The complexity of the problem, the possibility of systematic improvement or the quality in the description of a specific model are usually the main elements to take into account in this choice. Moreover, these approximations are not mutually exclusive: in some situations we develop approximate free-energy functionals by means of a combination of them.

Local-density approximation (LDA)

In the case of a fluid in the presence of an external potential $v(\mathbf{r})$, which we assume to depend on the positions of the particles $\mathbf{r}$ only, the simplest approach is the local-density approximation (LDA). When the bulk excess-free energy per unit volume $f^{\text{exc}}(\rho)$ of the homogeneous fluid at density ρ is known, the LDA reads

$$\mathcal{F}^{\text{exc}}[\rho] = \int d\mathbf{r}\, f^{\text{exc}}(\rho(\mathbf{r})). \tag{2.39}$$

As it appears from Eq. (2.39), the LDA implies that the fluid behaves locally as if it were homogeneous, thus completely neglecting non-local effects. We can expect this approximation to hold only in the case of slowly varying fields, or, more specifically, when the length scale of the fluid inhomogeneity induced by the external field is much bigger than the correlation length. Eq. (2.39) can be interpreted as a zeroth order truncation of a gradient expansion of the free energy [21]. Therefore, by truncating the gradient expansion at higher orders, in case the corresponding expansion terms exist, we could improve the description by the introduction of non-local terms.

Second-virial approximation

The low-density thermodynamic behavior of a many-particle system with short-range interactions can be approximated by truncating the virial expansion of the free energy. Within this approach, the interaction potential is treated as a perturbation to the ideal-gas behavior. At the lowest non-trivial order the grand potential can be approximated as [16]

$$\Omega[\psi] \simeq \Omega_0[\psi] - \frac{1}{2\beta}\left\langle \sum_{i,j=1}^{N} f_m(\mathbf{x}_i, \mathbf{x}_j) \right\rangle_0, \tag{2.40}$$

where $\Omega_0[\psi]$ is the ideal-gas grand potential and the grand canonical average $\langle \ldots \rangle_0$ is performed over the reference non-interacting system. The Mayer function is defined in terms of the pairwise potential $u(\mathbf{x}_i, \mathbf{x}_j)$ as

$$f_m(\mathbf{x}_i, \mathbf{x}_j) = \exp\Big[-\beta u(\mathbf{x}_i, \mathbf{x}_j)\Big] - 1. \tag{2.41}$$

By means of Eq. (2.18), we can rewrite Eq. (2.40) as

$$\Omega[\psi] \simeq \Omega_0[\psi] - \frac{1}{2\beta}\int d\mathbf{x} d\mathbf{x}' \, f_m(\mathbf{x}, \mathbf{x}') \langle \overline{\rho}(\mathbf{x}) \overline{\rho}(\mathbf{x}') \rangle_0, \tag{2.42}$$

where the non-interacting reference system yields

$$\langle \overline{\rho}(\mathbf{x}) \overline{\rho}(\mathbf{x}') \rangle_0 = \langle \overline{\rho}(\mathbf{x}) \rangle_0 \langle \overline{\rho}(\mathbf{x}') \rangle_0 = \rho(\mathbf{x}) \rho(\mathbf{x}'), \tag{2.43}$$

such that upon comparing with Eq. (2.23), the excess free-energy functional reads

$$\mathcal{F}^{\text{exc}}[\rho] = -\frac{1}{2\beta}\int d\mathbf{x} d\mathbf{x}' \, f_m(\mathbf{x}, \mathbf{x}') \rho(\mathbf{x}) \rho(\mathbf{x}'). \tag{2.44}$$

When considering a homogeneous fluid of non-spherically symmetric particles interacting via a purely hard repulsive potential, we define the excluded-volume function

$$\mathcal{E}(\mathbf{\Omega}, \mathbf{\Omega}') = -\int d(\mathbf{r} - \mathbf{r}') f_m(\mathbf{x}, \mathbf{x}'), \tag{2.45}$$

which can be interpreted as the volume not accessible by the center of mass of a particle with orientation $\mathbf{\Omega}$, when another particle has orientation $\mathbf{\Omega}'$. The corresponding excess free-energy functional reads

$$\mathcal{F}^{\text{exc}}[\rho] = \frac{V}{2\beta}\int d\mathbf{\Omega} d\mathbf{\Omega}' \, \mathcal{E}(\mathbf{\Omega}, \mathbf{\Omega}') \rho(\mathbf{\Omega}) \rho(\mathbf{\Omega}'), \tag{2.46}$$

and gives rise to a density functional theory equivalent to the pioneering approach developed by L. Onsager to interpret the isotropic-nematic transition in colloidal hard-rod fluids [24].

Mean-field approximation

The mean-field approximation is in essence very similar to the second-virial approximation. In statistical physics the term "mean field" is often used with a quite general meaning, identifying all the theories that offer an approximate description of an interacting system by neglecting (some of) the correlations between its degrees of freedom [25]. However, with the term "mean-field" we refer here to a specific approximation, according to which the force experienced by one particle is modeled as an effective self-consistent force field (mean field) generated by all the remaining particles.

Let us suppose that (a good approximation for) the excess free-energy functional $\mathcal{F}_0^{\text{exc}}$ of a system of particles interacting via a pairwise potential $u_0(\mathbf{x},\mathbf{x}')$ is known. The grand potential of a system of particles interacting via a pairwise potential $u(\mathbf{x},\mathbf{x}') = u_0(\mathbf{x},\mathbf{x}') + \Delta u(\mathbf{x},\mathbf{x}')$ can be approximately expressed as a first-order truncated expansion in the perturbation $\Delta u(\mathbf{x},\mathbf{x}')$ as

$$\Omega[\psi] \simeq \Omega_0[\psi] + \frac{1}{2}\left\langle \sum_{i,j=1}^{N} \Delta u(\mathbf{x}_i,\mathbf{x}_j) \right\rangle_0, \tag{2.47}$$

where $\langle \ldots \rangle_0$ stands for the ensemble average over the reference system. Eq. (2.47) can be rewritten as

$$\Omega[\psi] \simeq \Omega_0[\psi] + \frac{1}{2}\int d\mathbf{x} d\mathbf{x}' \, \Delta u(\mathbf{x},\mathbf{x}') \langle \overline{\rho}(\mathbf{x})\overline{\rho}(\mathbf{x}')\rangle_0, \tag{2.48}$$

and, by neglecting two-body correlations, that is

$$\langle \overline{\rho}(\mathbf{x})\overline{\rho}(\mathbf{x}')\rangle_0 \simeq \langle \overline{\rho}(\mathbf{x})\rangle_0 \langle \overline{\rho}(\mathbf{x}')\rangle_0 = \rho(\mathbf{x})\rho(\mathbf{x}'), \tag{2.49}$$

we finally deduce the excess free-energy functional

$$\mathcal{F}^{\text{exc}}[\rho] = \mathcal{F}_0^{\text{exc}}[\rho] + \frac{1}{2}\int d\mathbf{x} d\mathbf{x}' \, \Delta u(\mathbf{x},\mathbf{x}')\rho(\mathbf{x})\rho(\mathbf{x}'). \tag{2.50}$$

Fundamental measure theory (FMT)

Contrarily to the approximations schemes described so far, which can in principle be applied to any system, the fundamental measure theory (FMT) was designed to reproduce the thermodynamics of only one specific model system: hard spheres. However, it does so very well. Developed in its original form by Y. Rosenfeld in 1989 [26], FMT is at present the best theory for the description of hard-sphere systems at equilibrium. Its merits are various and remarkable: it is designed to deal with mixtures, its non-local character gives an extremely good account for confinement conditions and it succeeds in accounting quantitatively for the freezing transition. In its original formulation, FMT gets inspiration from the exactly solvable

one-dimensional hard-rod model to build a high-density extrapolation of the scaled-particle theory equation of state of the homogeneous fluid from the inhomogeneous low-density second-virial behavior [26, 27].

A complete introduction to FMT falls beyond the scope of this thesis[3], and in this section we only describe its mathematical structure. The main assumption of FMT is that the excess free-energy functional of a mixture of M hard-sphere species can be written as a local functional

$$\beta\mathcal{F}^{\text{exc}}[\{\rho_i\}] = \int d\mathbf{r}\,\Phi(\{n_\alpha(\mathbf{r})\}), \tag{2.51}$$

of a limited number of weighted densities $n_\alpha(\mathbf{r})$, calculated as convolutions of the single particle densities $\rho_i(\mathbf{r})$ ($i = 1, \ldots, M$) with a limited number of geometry-inspired weight functions $w_\alpha^i(\mathbf{r})$,

$$n_\alpha(\mathbf{r}) \equiv \int d\mathbf{r}' \sum_{i=1}^{M} \rho_i(\mathbf{r}') w_\alpha^i(\mathbf{r}-\mathbf{r}'). \tag{2.52}$$

The total number of weight functions, as well as the explicit functional dependence of $\Phi(\{n_\alpha(\mathbf{r})\})$, vary from version to version of the theory itself.

Due to its remarkable success, there have been attempts to generalize FMT to dimensions other than $D = 3$, but also to non-spherical hard particles. Among the limited number of models for which a fundamental measure theory has been developed, one finds parallel hard cubes ($D = 3$) and squares ($D = 2$), which will be considered in Chapter 5.

2.4 Monte Carlo simulation

In Sec. 2.2 we have seen that an important aim of statistical mechanics is to compute ensemble averages as in Eq. (2.5). This type of calculation, which involves an integration over a high-dimensional space, is in general impossible to perform analytically. However, an evaluation of integrals like Eq. (2.5), which is in principle "exact", can be performed by means of computational methods based on Monte Carlo integration algorithms, also known as *Monte Carlo simulations*.

Let us focus on the case of a microscopic property, independent of the momenta of the particles, whose average is to be evaluated in the canonical ensemble. In this situation, the average value reads

$$\langle A\rangle_{TVN} = \frac{\int d\mathbf{X}\, A(\mathbf{X}) \exp[-\beta U(\mathbf{X})]}{\int d\mathbf{X} \exp[-\beta U(\mathbf{X})]}. \tag{2.53}$$

A numerical evaluation of the integral in Eq. (2.53) based on a homogeneous random sampling of the configuration space would be extremely inefficient. In fact,

[3] For an introduction to the fundamental measure theory see Refs. [28, 29].

only a tiny fraction of the high-dimensional space spanned by $\mathbf{X}$ is characterized by a corresponding Boltzmann factor which is appreciably different from zero. A much more efficient method would be based on generating random configurations $\mathbf{X}$ that are themselves distributed according to the Boltzmann distribution ("importance sampling"). However, how can we achieve this? The problem was addressed in the early days of computer science by N. Metropolis *et al.* [30].

The basic idea of the Metropolis algorithm consists of generating a stochastic collection of microscopic configurations $\{\mathbf{X}_n\}$ (Markov chain). The transition matrix of the Markov chain is chosen in such a way that the asymptotic state $\mathbf{X}_{n\to\infty}$ is generated with a probability given by the Boltzmann distribution [31]. In practice, by starting from an initial configuration $\mathbf{X}_0$, we generate a successive number of random configurations $\mathbf{X}_1, \mathbf{X}_2, \ldots$, where typically $\mathbf{X}_n = \mathbf{X}_{n-1} + \Delta\mathbf{X}$ and $\Delta\mathbf{X}$ is randomly generated. A configuration $\mathbf{X}_n$ is accepted as an element of the Markov chain with a probability

$$\mathrm{acc}(n-1 \to n) = \min\left\{1, \exp\left[-\beta\big(U(\mathbf{X}_n) - U(\mathbf{X}_{n-1})\big)\right]\right\}. \tag{2.54}$$

In such a way, after a number of Monte Carlo steps which depends on the choice of the initial configuration, the Markov chain reaches a steady-state condition. When the steady state is reached, any ensemble average of the property $A(\mathbf{X})$ can be calculated as an arithmetic average over the configurations generated by the algorithm. So far we focused on averages evaluated in the canonical ensemble, but extensions of Monte Carlo algorithms to other ensembles, like the important case of the isothermal isobaric NPT ensemble, exist [31].

In summary, the Monte Carlo simulation approach consists of generating a series of configurations that asymptotically mimic the Boltzmann distribution. This approach is radically different from Molecular Dynamics simulations, where the microscopic time evolution of the system is reproduced instead. Actually, no time scale is defined in Monte Carlo simulations at all. Nevertheless, in Chapter 6 we will see that Monte Carlo algorithms can be extremely useful to simulate the microscopic dynamics of colloidal particles. Once again, this is a consequence of the Brownian character of the dynamics of colloids. In fact, on time scales sufficiently long the dynamics of a colloid subject to the continual collisions with solvent molecules resembles that of a random walker [1]. This means that the time evolution of the colloid's degrees of freedom can be treated as a Markov chain. Therefore, the Monte Carlo algorithm allows to simulate in an approximate way the dynamics of a colloidal suspension. In order to achieve this result, the algorithm has to be designed in such a way that the transition matrix of the Markov chain reproduces the diffusion constant of the colloid in the solvent.

Chapter 3

Polydispersity stabilizes biaxial nematic phases

Abstract

Inspired by the observations of a remarkably stable biaxial nematic phase, we investigate the effect of size polydispersity on the phase behavior of a suspension of boardlike particles. By means of Onsager theory within the restricted-orientation (Zwanzig) model we show that polydispersity induces a novel topology in the phase diagram, with two *Landau tetracritical points in between which* oblate *uniaxial nematic order is favored over the expected* prolate *order. Additionally, this phenomenon causes the opening of a huge stable biaxiality regime in between uniaxial nematic and smectic states.*

3.1 Introduction

Since its first prediction back in the early 1970s [32–34], the *biaxial nematic* phase (N_B) has strongly attracted the interest of the liquid-crystal community [35, 36]. In contrast to the more common *uniaxial nematic* (N_U) phase, where cylindrical symmetry with respect to the nematic director determines optical uniaxiality, the N_B phase is characterized by an orientational order along three directors and, consequently, by the existence of two distinct optical axes. The prospect of inducing orientational ordering along three directions, while maintaining a nematic fluid-like mechanical behavior [37], renders biaxial nematics preeminent candidates for next generation liquid-crystal based displays [38]. Although experimental evidences of stable N_B phases were reported already 30 years ago in lyotropic liquid crystals [39], in thermotropics this result was achieved in systems of bent-core molecules only a few years ago [40, 41]. Actually, when trying to experimentally reproduce an N_B phase, one often encounters practical problems related to its unambiguous identification [35, 36] and to the presence of competing thermodynamic structures [42–44]. Stabilizing N_B states is therefore an open, challenging scientific problem with huge potential applications. Motivated by the exciting results of a recent experiment

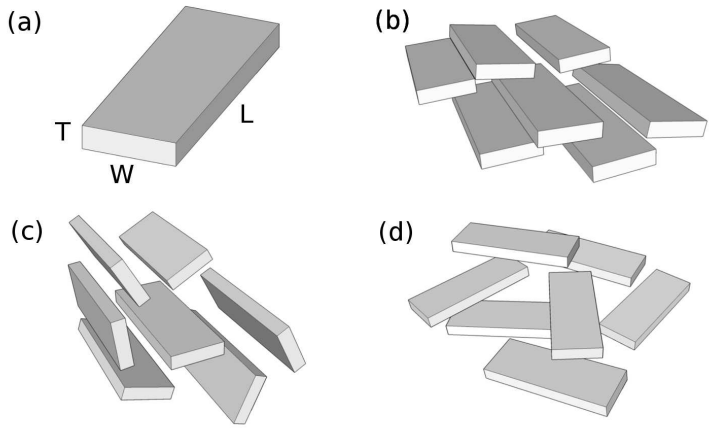

Figure 3.1: (a) Cuboidal particle with dimensions $L \times W \times T$. (b) Schematic representation of a system of freely rotating cuboids in the biaxial nematic phase N_B, (c) the uniaxial nematic prolate N_+ and (d) the uniaxial nematic oblate N_-.

on a colloidal suspension [45], we use here a mean-field theory to investigate the role played by size polydispersity on the stability of biaxial nematics in systems of boardlike particles. We show that a difference in the particle volume of a binary mixture can favor *oblate* uniaxial orientational ordering over *prolate*, in sharp contrast with the behavior of the pure systems. This phenomenon gives rise to a new phase diagram topology due to the appearance of *two* Landau tetracritical points, leading to a wider region of N_B stability. This feature is shown to hold also for a larger number of components, thus offering an explanation to the experimental results of Ref. [45]. Finally, we argue that our findings could furnish a new way to look for biaxiality in thermotropic liquid crystals.

At low density in lyotropics, and at high temperature in thermotropics, the N_B phase appears as a crossover regime in between "rod-like" and "plate-like" behavior [33]. In fact, one can distinguish between the N_U phase developed by rods, in which particles align the longest axis along a common direction (uniaxial nematic *prolate*, N_+), and that developed by plates, in which particles align the shortest axis (uniaxial nematic *oblate*, N_-). A natural candidate system for developing an N_B phase is a binary mixture of rods and plates [46]; however, in most cases a demixing transition into two uniaxial nematic phases, i.e., N_+ and N_-, prevents its stabilization [43, 44]. Alternatively, a stable N_B state is expected in a system of particles with cuboid (i.e., rectangular parallelepiped) shape defined by the lengths of the principal axes $L \geq W \geq T$, as depicted in Fig. 3.1(a) [34]. In this case, it is convenient to introduce a *shape parameter* ν, defined by

$$\nu = \frac{L}{W} - \frac{W}{T}. \tag{3.1}$$

By increasing the packing fraction and disregarding the possible stability of inhomogeneous phases, according to mean-field theory a system of cuboids undergoes an $I \to N_+ \to N_B$ sequence of phases if $\nu > 0$, whereas an $I \to N_- \to N_B$ sequence is found if $\nu < 0$ (I stands for the isotropic phase) [47]. A schematic representation of these nematic phases is given in Fig. 3.1(b)-(d). The case $\nu = 0$ describes the optimal "brick" shape exactly in between "rod-like" and "plate-like". In this case the N_U phase is suppressed and substituted by a second-order IN_B transition [47].

The first experimental realization of the hard-cuboid model was found only recently in a colloidal suspension of boardlike mineral goethite particles [45]. By producing particles with shape parameter $\nu \simeq 0.1$ close to zero ($\langle L\rangle \times \langle W\rangle \times \langle T\rangle = 254 \times 83 \times 28\,\mathrm{nm}^3$ and size polydispersity of $20-25\%$), the authors were able to produce an N_B phase stable over a pressure range surprisingly much wider than to be expected from theory [42, 48] and simulations [49] for particles whose shape parameter deviates even slightly from zero. Even more interestingly, the authors affirm that *no* N_U phase was observed, contrasting Ref. [47]. They suggest that a possible reason for this disagreement should be found in ingredients whose effects have never been studied so far because of their complexity, i.e., fractionation, sedimentation and polydispersity. These unexpected results motivate our interest in analyzing the effect of the above mentioned ingredients, in particular polydispersity, on the stability of the N_B phase in a fluid of hard cuboids.

3.2 Model and theory

We consider an M-component suspension of N_α colloidal cuboidal particles of species $\alpha = 1, \ldots, M$ with dimensions $L_\alpha \times W_\alpha \times T_\alpha$ ($L_\alpha > W_\alpha > T_\alpha$) in a volume V at temperature T. The total number density of colloids is

$$n = \sum_{\alpha=1}^{M} \frac{N_\alpha}{V} = \frac{N}{V}, \tag{3.2}$$

the mole fraction of species α is

$$x_\alpha = \frac{N_\alpha}{N}, \tag{3.3}$$

and the packing fraction is

$$\eta = n \sum_{\alpha=1}^{M} x_\alpha L_\alpha W_\alpha T_\alpha. \tag{3.4}$$

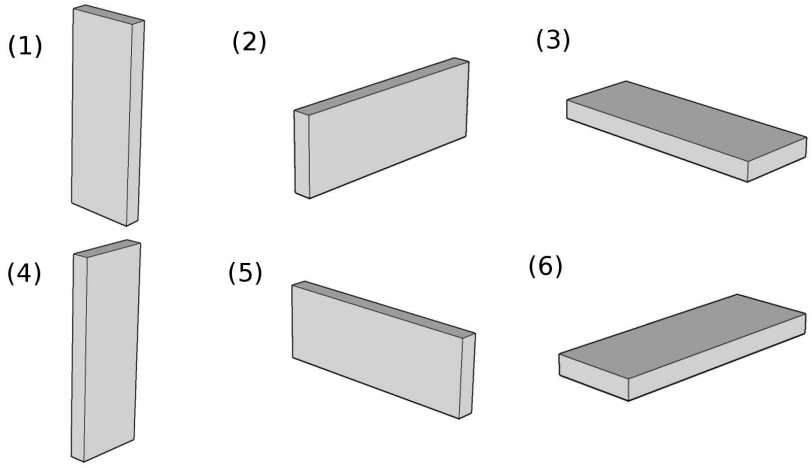

Figure 3.2: The 6 independent orientations of a boardlike particle within the restricted-orientation (Zwanzig) model [50].

The theoretical framework used in this chapter consists of Onsager theory of liquid crystals [24], which is a density functional theory truncated at second-virial order (cf. Sec. 2.3.4). In order to facilitate the calculations, we follow Zwanzig by restricting the orientations of the particles to the six in which their principal axes are aligned along a fixed Cartesian frame, as in Fig. 3.2 [50]. By means of this process of discretization of the orientational degrees of freedom, a particular orientation is identified with a number $i = 1, \ldots, 6$, as summarized in Tab. 3.1.

Although quantitative agreement with real systems is not expected because of the simplifications introduced in the model, the same model was shown to successfully predict non-trivial phenomena like demixing in rod-plate mixtures [43], orientational wetting due to confinement and capillary nematization [51]. As explained in Sec. 2.3.2, in density functional theory the intrinsic free-energy functional is the sum of an ideal and an excess component. By denoting with $\rho_i^\alpha(\mathbf{r})$ the local density of particles of species $\alpha = 1, \ldots, M$ with orientation $i = 1, \ldots, 6$, the ideal free-energy functional for this multi-component model with discretized orientations reads (cf. Eq. (2.30))

$$\beta\mathcal{F}^{\mathrm{id}}[\rho] = \int d\mathbf{r} \sum_{i=1}^{6} \sum_{\alpha=1}^{M} \rho_i^\alpha(\mathbf{r}) \left\{ \log[\rho_i^\alpha(\mathbf{r}) \mathcal{V}_\alpha] - 1 \right\}, \tag{3.5}$$

where $\beta = (k_B T)^{-1}$, T is the absolute temperature, k_B is the Boltzmann constant and $\mathcal{V}_\alpha$ the thermal volume of species α. An exact expression for the excess component of the intrinsic free-energy functional is not known. Here we apply the second virial order approximation (cf. Sec. 2.3.4), in such a way that the excess free-energy functional is approximated by

i	L	W	T
1	x	y	z
2	z	x	y
3	y	z	x
4	x	z	y
5	y	x	z
6	z	y	x

Table 3.1: Enumeration of the possible orientations of a hard cuboid within the Zwanzig model. Each configuration i is identified with the directions (x, y, z) along which the particle axes (L, W, T) are aligned.

$$\beta\mathcal{F}^{\text{exc}}[\rho] = -\frac{1}{2}\int d\mathbf{r}d\mathbf{r}' \sum_{i,i'=1}^{6}\sum_{\alpha,\alpha'=1}^{M} f_m^{\alpha\alpha' ii'}(\mathbf{r}-\mathbf{r}')\rho_i^{\alpha}(\mathbf{r})\rho_{i'}^{\alpha'}(\mathbf{r}'). \tag{3.6}$$

The Mayer function

$$f_m^{\alpha\alpha' ii'}(\mathbf{r}) = \exp\left[-\beta u_{ii'}^{\alpha\alpha'}(\mathbf{r})\right] - 1, \tag{3.7}$$

is defined in terms of the pairwise potential $u_{ii'}^{\alpha\alpha'}(\mathbf{r})$ of a pair of particles belonging to species α and α' with orientation i and i', respectively, and relative position $\mathbf{r}$. For hard cuboids with dimensions $L_\alpha \times W_\alpha \times T_\alpha$ the interaction potential is

$$\beta u_{ii'}^{\alpha\alpha'}(\mathbf{r}) = \begin{cases} \infty & \text{if } |x| < (X_i^{\alpha} + X_{i'}^{\alpha'})/2 \\ & \text{and } |y| < (Y_i^{\alpha} + Y_{i'}^{\alpha'})/2 \\ & \text{and } |z| < (Z_i^{\alpha} + Z_{i'}^{\alpha'})/2; \\ 0 & \text{otherwise,} \end{cases} \tag{3.8}$$

and expresses reciprocal impenetrability. According to the index notation defined in Tab. 3.1, the 6-dimensional vectors $\mathbf{X}^\alpha$, $\mathbf{Y}^\alpha$ and $\mathbf{Z}^\alpha$ of species α introduced in Eq. (3.8) are given in terms of the dimensions of the particles by

$$\begin{aligned} \mathbf{X}^\alpha &= (L_\alpha, W_\alpha, T_\alpha, L_\alpha, W_\alpha, T_\alpha), \\ \mathbf{Y}^\alpha &= (W_\alpha, T_\alpha, L_\alpha, T_\alpha, L_\alpha, W_\alpha), \\ \mathbf{Z}^\alpha &= (T_\alpha, L_\alpha, W_\alpha, W_\alpha, T_\alpha, L_\alpha). \end{aligned} \tag{3.9}$$

The main goal of this chapter is to study the stability of spatially homogeneous phases (i.e., isotropic and nematic). In this case we can simplify the problem by neglecting spatial modulations in the single-particle density, i.e., by imposing $\rho_i^\alpha(\mathbf{r}) =$

ρ_i^α. Consequently, the intrinsic free-energy functional, sum of ideal (Eq. (3.5)) and excess (Eq. (3.6)) components, becomes

$$\frac{\beta\mathcal{F}[\rho]}{V} = \sum_{\alpha=1}^{M}\sum_{i=1}^{6}\rho_i^\alpha\left\{\log[\rho_i^\alpha\mathcal{V}_\alpha]-1\right\} + \frac{1}{2}\sum_{\alpha,\alpha'=1}^{M}\sum_{i,i'=1}^{6}\mathcal{E}_{ii'}^{\alpha\alpha'}\rho_i^\alpha\rho_{i'}^{\alpha'}, \tag{3.10}$$

which is the restricted-orientation version of the Onsager free energy (cf. Eq. (2.46)) [24]. The matrix $\mathcal{E}_{ii'}^{\alpha\alpha'}$ in Eq. (3.10) is the excluded volume between two particles belonging to species α and α' with orientations i and i', and reads

$$\mathcal{E}_{ii'}^{\alpha\alpha'} = (X_i^\alpha + X_{i'}^{\alpha'})(Y_i^\alpha + Y_{i'}^{\alpha'})(Z_i^\alpha + Z_{i'}^{\alpha'}). \tag{3.11}$$

Since at sufficiently high density one expects spatially inhomogeneous phases to be thermodynamically favored, we apply bifurcation theory [47] to determine the limit of stability of the homogeneous equilibrium phases with respect to smectic fluctuations (cf. Appendix 3.A.1).

3.3 Prelude: monodisperse case

The main goal of the present chapter is to investigate how polydispersity affects the phase behavior of a system of hard cuboids. It is therefore instructive to study what the theoretical framework described in Sec. 3.2 predicts for the pure component, i.e., when the total number of species is $M = 1$. We focus here on the role of the particles aspect ratios L/T and W/T on the phase behavior (cf. Fig. 3.1(a)). Since our final goal involves among other things the interpretation of the experiments of Ref. [45], we consider aspect ratios close to the experimental ones, that is, $L/T = 9.07$ and $W/T = 2.96$.

In Fig. 3.3 we report the phase diagram of a monodisperse system of hard cuboids as a function of the aspect ratio W/T at fixed $L/T = 9.07$. By varying W/T (and therefore the shape parameter $\nu = L/W - W/T$) at fixed L/T, one observes a transition from plate- to rod-like behavior when crossing the value $\nu = 0$. In other terms, by passing from negative to positive values of the shape parameter ν, one finds in second-virial theory a transition from a stable oblate N_- to a stable prolate N_+ phase [47]. Moreover, by means of bifurcation theory we estimate the upper limit of stability of homogeneous phases with respect to the smectic (see dashed line in the phase diagram of Fig. 3.3). Fig. 3.3 highlights the fact that, in order to observe a stable N_B phase, the shape of the particles should be designed with extremely high precision in a small ν-regime about $\nu = 0$. In fact, for $L = 9.07\,T$ the N_B phase disappears unless $2.96\,T < W < 3.08\,T$. This is due both to the tight cusp-like shape of the $N_U N_B$ transition line and to the preempting character of inhomogeneous phases. Analogous results would be obtained by varying the shape parameter through L/T, while keeping W/T fixed. Finally, in the inset of Fig. 3.3 (note the different scale) we show the first order character of the IN_U transition.

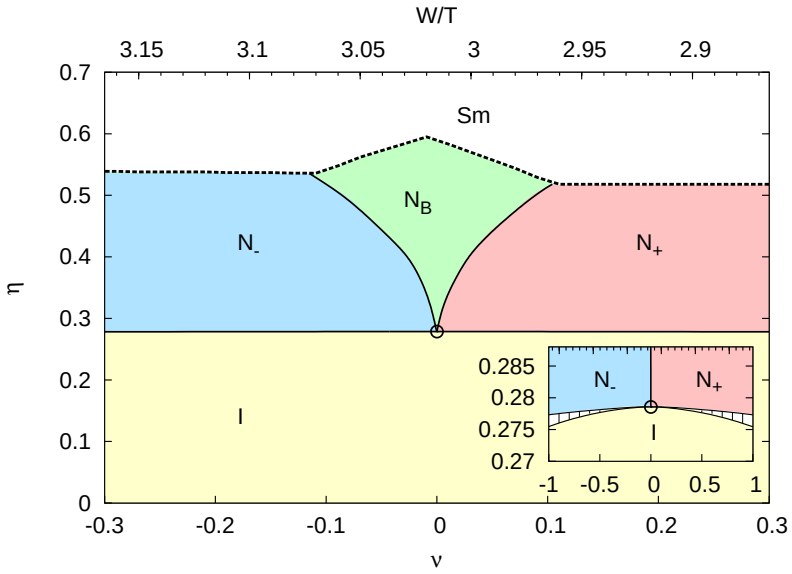

Figure 3.3: Phase diagram of a monodisperse system of hard cuboids as a function of the packing fraction η and the shape parameter $\nu = L/W - W/T$ (here $L/T = 9.07$ is fixed and W/T is varied). The solid lines indicate phase boundaries as calculated by minimizing the Onsager-Zwanzig functional, the dashed line indicates the limit of stability of the nematic with respect to the smectic phase and the open circle the Landau critical point. The inset highlights the first order character of the IN_U transition and how this tends to become continuous by approaching $\nu = 0$.

Notice how such an IN_U transition tends to become continuous while approaching the Landau critical point at $\nu = 0$.

For the sake of completeness, in Fig. 3.4 we report the orientation distribution function p_i, which is the probability of a given orientation $i = 1, \ldots, 6$ as a function of the packing fraction η for different values of the shape parameter ν at fixed $L/T = 9.07$. In a one-component systems $p_i = \rho_i/n$, where $n = N/V$ is the number density. The values of the orientation distribution function characterize the symmetry of the corresponding phase. In fact, at a given packing fraction η one can have one of the following possibilities:

- the probabilities p_i are all the same, i.e., $p_i = 1/6 \simeq 0.166$ (isotropic I phase);
- the probabilities p_i are coupled two-by-two, highlighting the presence of a symmetry axis (uniaxial nematic N_U phase);
- the probabilities p_i are all different between each other (biaxial nematic N_B phase).

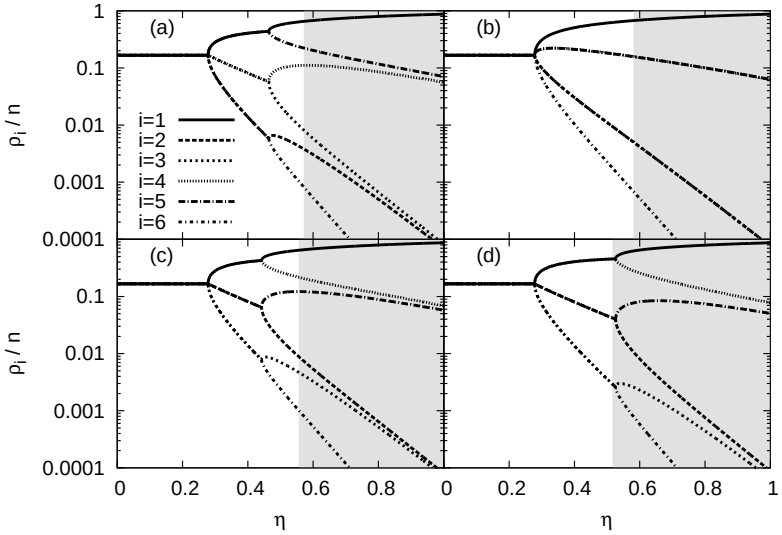

Figure 3.4: Orientation distribution function of a homogeneous monodisperse system of hard cuboids as a function of the packing fraction η obtained by minimization of the Onsager-Zwanzig functional Eq. (3.10) for $M = 1$. The cuboids have dimensions $L/T = 9.07$ and (a) $W/T = 3.04$, (b) $W/T = 3.01$, (c) $W/T = 2.99$, (d) $W/T = 2.96$. The different lines indicate the probability of a particular orientation $i = 1, \ldots, 6$ (cf. Tab. 3.1). The gray area highlights the high-density region where the nematic phase is expected to be metastable with respect to inhomogeneous phases.

Moreover, in the uniaxial nematic case one can further distinguish two situations:

- the two more probable orientations have the shortest axis aligned along the same direction (uniaxial nematic oblate N_- phase);
- the two more probable orientations have the longest axis aligned along the same direction (uniaxial nematic prolate N_+ phase).

With this in mind, one can appreciate the difference in the orientation distribution function when $\nu = -0.06 < 0$ ($W/T = 3.04$, Fig. 3.4(a)), $\nu = 0$ ($W/T = 3.01$, Fig. 3.4(b)) and $\nu = 0.04 > 0$ ($W/T = 2.99$, Fig. 3.4(c)). The gray area indicates the high-density region where our bifurcation analysis suggests that the nematic phase is metastable with respect to inhomogeneous phases. Finally, Fig. 3.4(d) shows the orientation distribution function when the experimental value $W/T = 2.96$ is considered [45]. These results highlight how according to our model the N_B phase is expected to be preempted by inhomogeneous phases.

3.4 Binary mixture

Our analysis proceeds by considering the simplest case of polydispersity, i.e., a mixture of $M = 2$ components with mole fractions x_1 and $x_2 = 1 - x_1$, respectively. Among the different ways one can parameterize polydispersity, our preliminary analysis suggests to consider *volume polydispersity* (i.e., same particle shape but different volume). Therefore, we study the phase behavior of a binary mixture of hard cuboids whose dimensions are

$$\begin{array}{lll} L_1 = L(1+s), & W_1 = W(1+s), & T_1 = T(1+s), \\ L_2 = L(1-s), & W_2 = W(1-s), & T_2 = T(1-s), \end{array} \tag{3.12}$$

where the parameter $s \in [0,1)$ describes the degree of bidispersity. Notice that Eq. (3.12) implies the same aspect ratios for both species $L_1/T_1 = L_2/T_2 = L/T$ and $W_1/T_1 = W_2/T_2 = W/T$ (hence $\nu_1 = \nu_2 = \nu$). Here we set $L/T = 9.07$ and $W/T = 2.96$ ($\nu = 0.1$) in order to reproduce the experimental parameters of Ref. [45], thereby neglecting the small effect of the ionic double layer used by the authors to interpret the experimental data.

Fig. 3.5 shows density-composition phase diagrams of binary mixtures ($M = 2$) of boardlike particles with the experimental shape parameter $\nu = 0.1$ for various bidispersity parameters (a) $s = 0.15$, (b) 0.18, (c) 0.20 and (d) 0.30, featuring isotropic (I), uniaxial nematic (N_+ *and* N_-), biaxial nematic (N_B) and smectic (Sm) phases. Due to the near-perfect "biaxial" shape of the particles, i.e., $\nu \simeq 0$, fractionation is extremely weak and invisible on the scale of Fig. 3.5. Further details on the role of fractionation between homogeneous phases are given in Appendix 3.A.2. At the extreme mole fractions $x_1 = 0$ and $x_1 = 1$ (pure systems) all phase diagrams feature the phase sequence $I \to N_+ \to Sm$ that is well known and expected for board-shaped particles with $\nu > 0$, with the N_B phase metastable with respect to the Sm phase [42, 47] (cf. Sec. 3.3). However, for all $s > 0$ there is an intermediate composition regime in which the N_B phase is found to be stable, the more so for increasing s. Whereas the opening-up of a stable N_B regime is only quantitative for $s = 0.15$, there is a qualitative change of the phase diagram topology beyond $s = 0.18$, where *two* Landau tetracritical points appear (open circles in Figs. 3.5(b)-(d)). In between these critical points a region of stable N_- phase, which is *not* expected for the rod-shaped particles ($\nu > 0$) of interest, opens up. Clearly, Figs. 3.5(c) and (d) show that this unexpected N_- regime enlarges with bidispersity, accompanying a further increased N_B stability. In other words, excluded-volume interactions in mixtures of prolate boards with the same shape and different volume tend to favor N_B states as a consequence of a prolate-oblate (N_+N_-) competition. At higher packing fractions the increased N_B stability with respect to the Sm phase is not a surprise, given that regular packing into layers is hindered by size differences between particles [48].

It is interesting to understand how the remarkable features of the binary mixture described in Fig. 3.5 change with the shape of the particles. Here we are mainly interested in two properties of the phase diagram: (i) the minimum threshold bidispersity s_{thr} at which the Landau tetracritical points appear and (ii) the

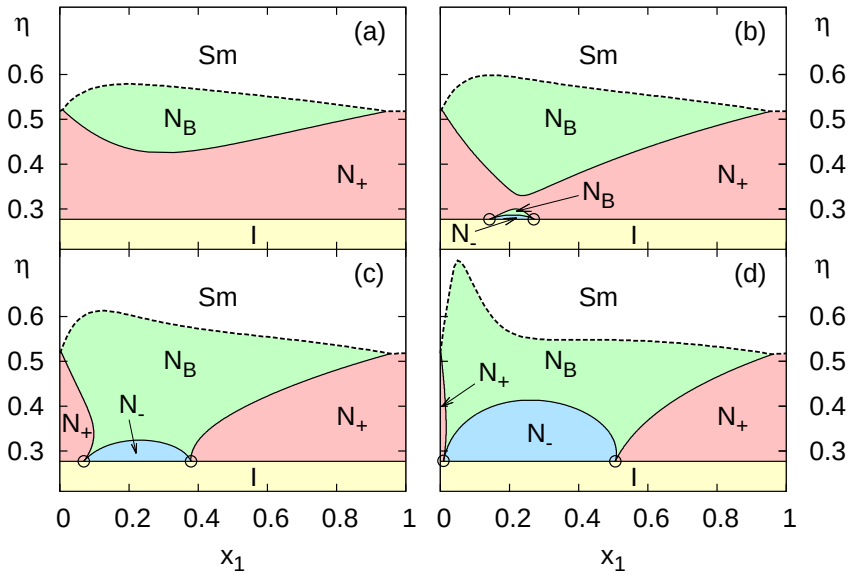

Figure 3.5: Phase diagram of a binary mixture of hard cuboids in terms of packing fraction η vs. mole fraction of the larger component x_1 showing isotropic (I), uniaxial (N_+ and N_-) and biaxial (N_B) nematic and smectic (Sm) phases. The size of the particles is defined by Eq. (3.12) with $L/T = 9.07$, $W/T = 2.96$ ($\nu = 0.1$) and bidispersities (a) $s = 0.15$, (b) $s = 0.18$, (c) $s = 0.20$, (d) $s = 0.30$. The solid lines separate different homogeneous phases, the dashed lines indicate the limit of stability of the homogeneous phases with respect to smectic fluctuations, whereas the open circles represent the Landau tetracritical points.

tetracritical mole fractions x_1^* in terms of the bidispersity s. We change the particle shape ($\nu = L/W - W/T$) by fixing in Eq. (3.12) one aspect ratio (W/T) and varying the remaining one (L/T). Fig. 3.6(a) shows for $W/T = 2.0$, 2.96, 4.0 and 5.0 a similar trend: the minimum threshold bidispersity s_{thr} increases the more the shape deviates from the optimal "brick" one (i.e., $\nu = 0$). The fact that at fixed ν the threshold bidispersity decreases with W/T indicates that the appearance of the Landau tetracritical points is favored by an increasing aspect ratio of the particles, in qualitative agreement with Ref. [52]. By fixing the aspect ratio $W/T = 2.96$, we observe in Fig. 3.6(b) the tetracritical mole fraction as a function of the bidispersity for different values of $\nu = 0.01$, 0.1 and 0.25. The closer the shape to the optimal "brick", for which $\nu = 0$, the wider the difference in value of the two tetracritical mole fractions x_1^* and, consequently, the wider stability regime of the N_- phase. Finally, we note that no critical composition is observed if the particles are closer to the "plate-like" shape. In other words, if $\nu_1 = \nu_2 = \nu < 0$ one finds the N_- in between the I and N_B phases for every value of s and x_1 (not shown); the N_+ phase does *not* occur in this case.

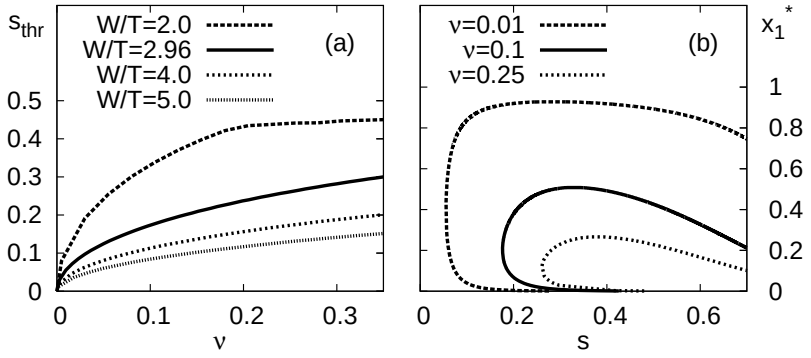

Figure 3.6: (a) Threshold bidispersity s_{thr} for the appearance of a tetracritical point as a function of the shape parameter ν for different fixed values of W/T. (b) Critical mole fraction x_1^* as a function of the bidispersity parameter s for a binary mixture of hard cuboids for different particle aspect ratios (cf. Eq. (3.12)).

3.5 Realistic model of polydispersity

In order to analyze proper polydispersity, and thus more realistically model the experimental system of Ref. [45], we extend our calculations to a system of $M = 21$ components of cuboids. Inspired by our analysis of the binary mixture and by the experiments [45], we fix the aspect ratios of all species to $L_\alpha/T_\alpha = L/T = 9.07$ and $W_\alpha/T_\alpha = W/T = 2.96$, such that (i) all species have the same shape $\nu_\alpha = \nu = 0.1$ and (ii) the size of each species is completely determined by T_α. We consider T_α to be distributed according to a discretized Gaussian function with average $\langle T \rangle = 28\,\mathrm{nm}$ and standard deviation $\sigma\langle T \rangle$, where σ is the (relative) size polydispersity. In general the calculation of a (high-dimensional) phase diagram of a multi-component system is a daunting task [53–55]. As explained in Appendix 3.A.2, it is in this case justified to ignore fractionation between homogeneous phases, which reduces the problem to minimizing the functional with respect to ρ_i^α at fixed nx_α. The resulting phase diagram in the density-polydispersity representation is shown in Fig. 3.7(a), featuring again I, N_+, N_-, N_B and Sm equilibrium states and a tetracritical point at $\sigma \simeq 24\%$, which is surprisingly close to the size polydispersity in the experiments [45]. The strikingly large stability regime of the N_B is caused by the reduced stability of Sm and N_+ (cf. Fig. 3.7(b)), not unlike in the binary case. However, a direct IN_B transition similar to that observed in Ref. [45] is not expected in this model due to the reentrant character of the N_+N_B phase transition (cf. Fig. 3.7(c)).

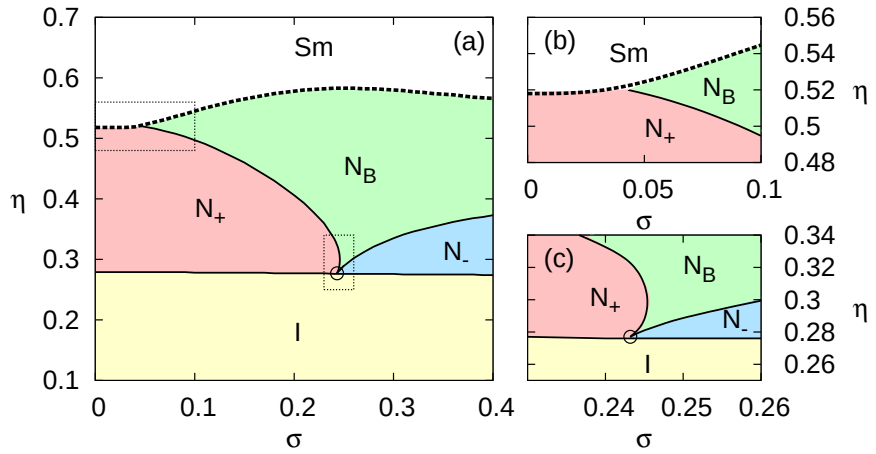

Figure 3.7: (a) Phase diagram of $M = 21$ components of hard cuboids (packing fraction η) with aspect ratios $L_\alpha/T_\alpha = 9.07$ and $W_\alpha/T_\alpha = 2.96$ ($\alpha = 1, \ldots, M$) and Gaussian-distributed dimensions with polydispersity σ (see text). The dashed line indicates the limit of stability of the homogeneous phases with respect to smectic fluctuations. The dotted rectangles highlight (b) the absence of the N_B phase at polydispersity $\sigma < 4\%$ due to the direct N_+Sm phase transition and (c) the reentrant character of the N_+N_B transition close to the tetracritical point (open circle).

3.6 Conclusions

In conclusion, by means of a mean-field theoretical approach with discrete orientations we have shown that size polydispersity strongly affects the phase behavior of boardlike particles, driving the emergence of a novel topology of the phase diagram. This topology change is due to the appearance of Landau tetracritical points, which in turn is related to a competition between the prolate "rod-like" ordering typical of the pure components and the oblate "plate-like" ordering purely induced by the mixing. In combination with the destabilization of the Sm phase, we can conclude that polydispersity dramatically increases the stability regime of the N_B phase. The usual stability limitations of N_B phases, such as N_+N_- demixing of rod-plate mixtures and ordering into smectics, are therefore overcome in the present system. Although this work focuses on a particular value of the particle dimensions, its predictions hold for a more general choice of the relevant parameters. Moreover, we do not expect the homogeneous phase behavior to be crucially dependent on the form of the interaction (cuboidal). On the contrary, it should be qualitatively similar to other excluded-volume interactions with the *same* symmetry (e.g. spheroid, spheroplatelet).

Finally, it is tempting to consider this work in the perspective of stabilizing N_B thermotropic liquid crystals. In this case, the soft-core character of the inter-

molecular interactions does not allow for a univocal definition of "shape", and van der Waals forces can significantly influence the phase diagram. Nonetheless, it is widely accepted that hard-core models contain the essential physical ingredients for a first-approximation description of the structure of a molecular or colloidal fluid [20, 56]. Following this interpretation scheme, it is intriguing to wonder whether it is possible to enhance the N_B stability by considering two- or multi-component mixtures of molecules with biaxial symmetry and different size.

Acknowledgements

We would like to thank E. van den Pol, G.J. Vroege and their collaborators for sharing with us their insights on the experiments of Ref. [45].

3.A Appendix

3.A.1 Nematic-Smectic bifurcation

While studying the homogeneous equilibrium phases of the model introduced in Sec. 3.2, we are also interested in estimating their upper bound in the phase diagram, where spatially inhomogeneous phases tend to be thermodynamically favored. Bifurcation theory provides a way to investigate the limit of stability of a particular phase (cf. Sec. 2.3.3).

Here we are interested in calculating the limit of stability of the (uniaxial or biaxial) nematic phase with respect to smectic fluctuations. With this in mind, in Eq. (2.38) we neglect spatial modulations in the reference phase, i.e., $\rho_i^\alpha(\mathbf{r}) = \rho_i^\alpha$, and assume a positional dependence of the fluctuations along the z direction only, i.e., $\delta\rho_i^\alpha(\mathbf{r}) = \delta\rho_i^\alpha(z)$. Within these assumptions Eq. (2.38) becomes

$$\sigma_i^\alpha(z) = \sum_{\alpha',i'} \int dz'\, Q_{ii'}^{\alpha\alpha'}(z-z')\,\sigma_{i'}^{\alpha'}(z'), \tag{3.13}$$

where $\sigma_i^\alpha(z) = \delta\rho_i^\alpha(z)/\sqrt{\rho_i^\alpha}$ and

$$Q_{ii'}^{\alpha\alpha'}(z) = \sqrt{\rho_i^\alpha \rho_{i'}^{\alpha'}} \int dx\, dy\, f_m^{\alpha\alpha' ii'}(\mathbf{r}), \tag{3.14}$$

a symmetric (Hermitean) kernel. By inserting the explicit form of the Mayer function given by Eqs. (3.7) and (3.8) into Eq. (3.14), one gets

$$Q_{ii'}^{\alpha\alpha'}(z) = \begin{cases} -\sqrt{\rho_i^\alpha \rho_{i'}^{\alpha'}}(X_i^\alpha + X_{i'}^{\alpha'})(Y_i^\alpha + Y_{i'}^{\alpha'}) \\ \qquad\qquad \text{if } |z| < (Z_i^\alpha + Z_{i'}^{\alpha'})/2; \\ 0 \qquad\qquad \text{otherwise.} \end{cases} \tag{3.15}$$

Eq. (3.13) is more conveniently solved in Fourier space, where it reads

$$\hat{\sigma}_i^\alpha(q) = \sum_{\alpha',i'} \hat{Q}_{ii'}^{\alpha\alpha'}(q)\hat{\sigma}_{i'}^{\alpha'}(q), \tag{3.16}$$

with

$$\hat{Q}_{ii'}^{\alpha\alpha'}(q) = -\sqrt{\rho_i^\alpha \rho_{i'}^{\alpha'}}\,\mathcal{E}_{ii'}^{\alpha\alpha'}\, j_0\big(q(Z_i^\alpha + Z_{i'}^{\alpha'})\big), \tag{3.17}$$

and $j_0(x) = \sin(x)/x$.

In conclusion, the limit of stability of the nematic phase with respect to smectic fluctuations can be numerically found as the minimum packing fraction $\bar{\eta}$ at which a wave vector $\bar{q}$ exists such that the $6M \times 6M$ matrix (M being the total number of components) with entries $\hat{Q}_{ii'}^{\alpha\alpha'}(\bar{q})$ has a unit eigenvalue. The periodicity of the corresponding bifurcating smectic phase is given by $\lambda = 2\pi/\bar{q}$.

3.A.2 Near-continuous character of the $I/N_{\pm}$ transition

When dealing with mixtures of M distinct species, the phase diagram is conveniently expressed in terms of the osmotic pressure P vs. the mole fraction x_α of $M-1$ components. In this way it is possible to visualize the coexistence of phases characterized by a different composition with respect to the parent distribution. This phenomenon, called demixing or fractionation, reveals the presence of a first-order phase transition.

Here we analyze demixing in a binary mixture of cuboids, whose dimensions

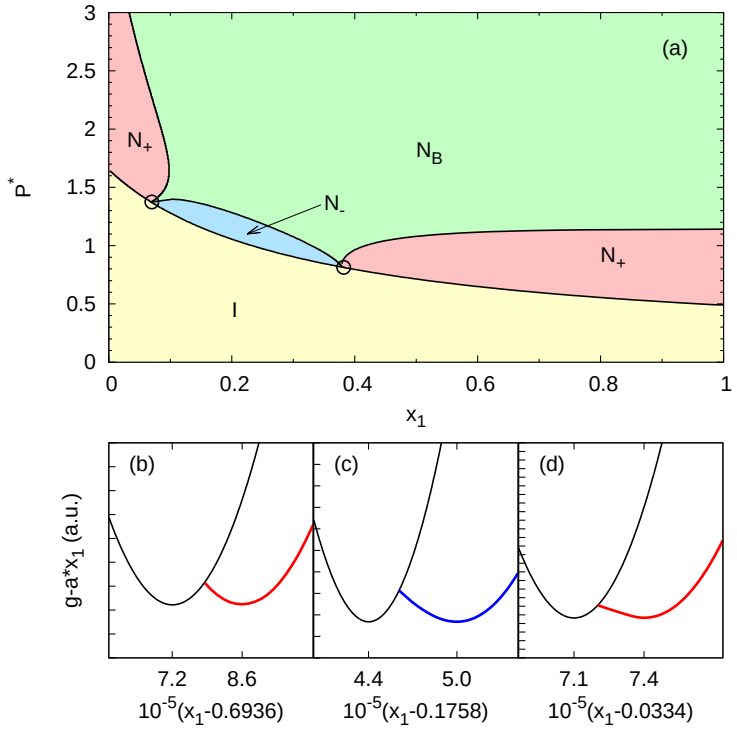

Figure 3.8: (a) Phase diagram of a binary mixture of hard cuboids in terms of the reduced osmotic pressure $P^* = \beta PLWT$ vs. mole fraction of the first species x_1. Unlike Figs. 3.3, 3.5 and 3.7 no bifurcation analysis concerning the limit of stability of the homogeneous with respect to inhomogeneous phases was performed in this case. (b)-(d) I (black line), N_+ (red line) and N_- (blue line) branches of the Gibbs free energy per particle $g = G/N$ at (b) $P^* = 0.6$, (c) $P^* = 1.1$ and (d) $P^* = 1.5$. A straight line with slope $a = \partial g/\partial x_1|_{x_1=x_I} = \partial g/\partial x_1|_{x_1=x_N}$ (with x_I and x_N the mole fractions of the coexisting isotropic and nematic phases) was subtracted in each case to enhance the visualization of the common tangent construction.

are parameterized as in Eq. (3.12) with $L/T = 9.07$, $W/T = 2.96$ and $s = 0.2$. In Fig. 3.8(a) we report the phase diagram for such a system as a function of the mole fraction x_1 of the larger species. Since our attention focuses on the demixing between homogeneous phases, we do not perform any bifurcation analysis with respect to inhomogeneous fluctuations. This means that the wide region of biaxial stability of Fig. 3.8(a) is expected to be appreciably reduced by including inhomogeneous states. On the scale of Fig. 3.8(a) the first-order character of the IN_U transitions is not detectable, but it is testified by the free-energy curves of Figs. 3.8(b)-(d). On the other hand, the $N_U N_B$ transition appears to be continuous even at a closer inspection (not shown). At three different values of the reduced osmotic pressure $P^* = \beta PLWT$ we calculate the isotropic and uniaxial nematic branches of the Gibbs free energy per particle $g(P, x_1) = \beta G(P, N_1, N_2)/(N_1 + N_2)$. The coexistence between the two phases is obtained by means of a common tangent construction, which allows to evaluate their difference in composition Δx_1. The results are reported in Figs. 3.8(b)-(d) for $P^* = 0.6$, 1.1 and 1.5, respectively. In the three cases, two of which describe an IN_+ and one an IN_- transition, $\Delta x_1 \approx 10^{-5}$ and can in practice be neglected. The situation does not change when considering different values of the bidispersity parameter s.

Although Landau-de Gennes theory predicts the IN_U transition to be first order [17], we have just shown that its discontinuous character can be safely neglected for the binary mixture of boardlike particles we consider in this work. In our opinion, this fact is tightly related to the shape of the particles, close to the $\nu = 0$ value. In fact, for a monodisperse system the closer ν to zero, the weaker the first-order character of the IN_U transition (cf. Sec. 3.3). This fact allows us to approximate the IN_U transition as continuous. As a consequence, we can neglect demixing between homogeneous phases in the analysis of the polydisperse system reported in Fig. 3.7, thus reducing enormously the complexity of our task.

Chapter 4

Depletion-induced biaxial nematic states of boardlike particles

Abstract

With the aim of investigating the stability conditions of biaxial nematic liquid crystals, we study the effect of adding a non-adsorbing ideal depletant on the phase behavior of colloidal hard boardlike particles. We take into account the presence of the depletant by introducing an effective depletion attraction between a pair of boardlike particles. At fixed depletant fugacity, the stable liquid-crystal phase is determined through a mean-field theory with restricted orientations. Interestingly, we predict that for slightly elongated boardlike particles a critical depletant density exists, where the system undergoes a direct transition from an isotropic liquid to a biaxial nematic phase. As a consequence, by tuning the depletant density, an easy experimental control parameter, one can stabilize states of high biaxial nematic order even when these states are unstable for the pure system.

4.1 Introduction

Onsager's intuition that purely repulsive rods undergo an entropy-driven transition from an isotropic (I) to an orientationally ordered nematic (N) phase constitutes one of the major milestones in our understanding of liquid crystals [24]. The key ingredient of this phenomenon relies on considering markedly non-spherical particles, which can be modeled as cylindrically symmetric "rods" and "plates". In the early 1970s Freiser pointed out that a richer phase behavior is expected, if the assumption of cylindrical symmetry is released [32]. Besides the usual prolate (N_+) and oblate (N_-) uniaxial nematic phases, normally developed by uniaxial rods and plates, respectively, a novel nematic phase with an increased orientational order can appear in the phase diagram. Such a liquid-crystal phase is characterized by alignment along three directors and, consequently, by the presence of two distinct optical axes, hence the name *biaxial nematic* (N_B) [35]. Further studies suggested that the N_B

stability could be interpreted as a balanced competition between rodlike (favoring N_+) and platelike (favoring N_-) behavior [33, 34, 47].

In more than 40 years since its first theoretical prediction, extensive theoretical [42, 43, 47, 48, 52, 57–62] and simulation [36, 49, 63–67] work has been devoted to identify the conditions under which a stable N_B phase could be observed. The practical limitations in this sense are testified by the fact that, apart from the micellar system studied by Yu and Saupe [39], no such state has been observed for more than 30 years. A renewed interest towards the topic has grown due to the first experimental realization of thermotropic N_B liquid crystals in systems of bent-core molecules a few years ago [40, 41]. In lyotropics, a remarkably stable N_B phase was recently discovered in a colloidal suspension of mineral boardlike particles [45].

Boardlike particles, that is, particles with the symmetry of a brick, represent the simplest model in which an N_B phase has been predicted [35]. However, the emergence of smectic layering is expected to prevent the realization of this phase, unless the constituent particles are designed with a precision far beyond present-day ability [42, 45]. A higher N_B stability can be achieved by considering size-polydisperse systems of boardlike particles, as demonstrated by a recent experiment [45]. In fact, polydispersity seems to enhance N_B stability through two distinct phenomena: (i) a reduced smectic stability [48] and (ii) an N_+N_- competition, which manifests itself exclusively in systems of slightly elongated (rodlike) boards (cf. Chapter 3). The first phenomenon does not come as a surprise [48], since it is well known that polydispersity renders the establishment of long-distance positional ordering unfavorable [68–70]. On the contrary, the reason behind the second phenomenon appears to be more obscure.

In this chapter we investigate the effect of a non-adsorbing depletant on the biaxial-nematic stability of (monodisperse) colloidal boardlike particles. Our understanding of depletion dates back to the pioneering work by Asakura and Oosawa [71] and Vrij [72], who showed that the addition of small co-solutes (e.g. polymers, surfactants, micelles) to a colloidal suspension gives rise to an effective attraction between colloidal particles. Since then, the concepts related to depletion have been widely applied to various scientific fields [73]: in biology by interpreting phenomena like macromolecular crowding [74] and protein crystallization [75]; in nanotechnology through e.g. the development of self-assembly processes as key-lock structures [76, 77]; in condensed matter physics, furnishing answers to fundamental problems like the condition for gas-liquid phase separation [78], the kinetics of crystallization [79, 80] and the nature of glassy states [81]. More recently, the liquid-crystal phase behavior of non-spherical colloids, typically rods [82–87] and plates [88–91], in the presence of a depletant has also been addressed. As a general feature, the addition of a depletant reduces the stability of liquid-crystal phases, leading to a direct isotropic-crystal transition at high enough depletant mole fraction. Moreover, when the size of the depletant particles is big enough, one or more critical points appear in the phase diagram, indicating a liquid-gas separation between phases with same spatial symmetries.

In contrast to the aforementioned work on rods and plates, we focus here on the

low depletant density limit, where the stability of the nematic liquid-crystal phases developed by the pure system of boardlike particles is preserved. In the same spirit as the Asakura-Oosawa-Vrij model for spheres [71, 72], we consider the limit of low depletant density and neglect depletant-depletant interactions. For the sake of convenience, we model the depletants as cubic particles excluded from the surface of the cuboids via a hard-core interaction. A mean-field theory at second virial order [21, 24] with restricted orientations (Zwanzig model) [50] constitutes our theoretical framework. The degrees of freedom of the depletant in the partition function can be systematically integrated out, giving rise to an effective potential between boardlike particles [92, 93], where only two-body interactions are considered. The assumption of an ideal depletant allows to determine an explicit expression for such a pairwise depletion potential. We show that, by varying the depletant density, the system develops a prolate-oblate (N_+N_-) competition remarkably similar to that predicted for a polydisperse system of boardlike particles in the absence of depletant, as described in Chapter 3. If in Chapter 3 the origin of this competition is not evident, here it appears to be due to a balance between the hard-core repulsion between slightly rodlike boardlike particles, favoring N_+ ordering, and the depletion attraction, favoring N_- ordering. As a consequence of this effect, the biaxial nematic phase appears to be stable over a wide range of depletant density. We therefore suggest that the concentration of a non-adsorbing depletant furnishes in practical situations the simplest, though effective, way to control the liquid-crystal phase behavior of boardlike particles and to select states of high biaxial-nematic stability.

4.2 Model and theory

The aim of the present section is the analysis of the phase behavior of colloidal boardlike particles in the presence of a non-adsorbing depletant. In what follows, the mesoscopic behavior of boardlike particles will be described by means of density functional theory. The effect of the depletant will be introduced in Sec. 4.3 by means of an effective pairwise potential between boardlike particles. The density functional theory approach we follow closely resembles that of Chapter 3. Here we summarize the main ingredients of the theory, while addressing the reader to Sec. 3.2 for further details.

We consider a system of N boardlike particles with dimensions $L \times W \times T$ ($L > W > T$ and particle volume $v = LWT$) in a box of volume V at temperature T. Accounting for the orientational degrees of freedom at the single-particle level requires a numerically demanding description based on 3 Euler angles. In order to circumvent this problem while keeping the essential physics of the system, we turn to the so-called Zwanzig model: the only allowed orientations are those with the main particle axes aligned along the Cartesian axes of a fixed reference frame [50]. Within this model a boardlike particle can take the 6 orientations depicted in Fig. 3.2, and the single-particle density is a 6-dimensional function with components $\rho_i(\mathbf{r})$ ($i = 1, \ldots, 6$). Within this restricted orientation model, the ideal component of

the intrinsic free-energy functional reads

$$\beta\mathcal{F}^{\mathrm{id}}[\rho] = \int d\mathbf{r} \sum_{i=1}^{6} \rho_i(\mathbf{r})\big\{\log[\rho_i(\mathbf{r})\mathcal{V}]-1\big\}, \tag{4.1}$$

where $\beta = (k_B T)^{-1}$, k_B is the Boltzmann constant, T the absolute temperature and $\mathcal{V}$ the thermal volume. Approximated at the second-virial order, the excess free-energy functional reads

$$\beta\mathcal{F}^{\mathrm{exc}}[\rho] = -\frac{1}{2}\int d\mathbf{r}d\mathbf{r}' \sum_{i,i'=1}^{6} f_m^{ii'}(\mathbf{r}-\mathbf{r}')\rho_i(\mathbf{r})\rho_{i'}(\mathbf{r}'), \tag{4.2}$$

where the Mayer function is defined in terms of the pairwise potential $u_{ii'}(\mathbf{r})$ between two boardlike particles with center-to-center distance $\mathbf{r}$ and orientations i and i', respectively, as

$$f_m^{ii'}(\mathbf{r}) = \exp\big[-\beta u_{ii'}(\mathbf{r})\big]-1. \tag{4.3}$$

In this chapter we are mostly concerned with the relative stability of isotropic and nematic (i.e., homogeneous) phases. Therefore, we can simplify the numerics involved in our problem by assuming homogeneity, i.e., by focusing on the case $\rho_i(\mathbf{r}) = \rho_i$. With this assumption, the intrinsic free-energy functional, sum of the ideal (Eq. (4.1)) and the excess (Eq. (4.2)) part, reads

$$\frac{\beta\mathcal{F}[\rho]}{V} = \sum_{i=1}^{6}\rho_i\big\{\log[\rho_i\mathcal{V}]-1\big\} + \frac{1}{2}\sum_{i,i'=1}^{6}\mathcal{E}_{ii'}\rho_i\rho_{i'}. \tag{4.4}$$

The 6×6 matrix $\mathcal{E}_{ii'}$, defined in terms of the Mayer function as

$$\mathcal{E}_{ii'} = -\int d\mathbf{r}\, f_m^{ii'}(\mathbf{r}), \tag{4.5}$$

coincides with the excluded volume between two boardlike particles with orientations i and i', respectively. As in Sec. 3.2 let us indicate with X_i the main axis (L, W or T) of a particle with orientation i along the x axis of a fixed reference frame (and similarly for Y_i and Z_i). Within the Zwanzig model each of the 6 independent orientations of a particle can be identified by (X_i, Y_i, Z_i), which is one of the 6 permutations of the three elements L, W and T. With these definitions one can write the interaction potential between two identical boardlike particles, modeled as hard cuboids, as

$$\beta u_{ii'}(\mathbf{r}) = \begin{cases} \infty & \text{if } |x| < (X_i + X_{i'})/2 \\ & \text{and } |y| < (Y_i + Y_{i'})/2 \\ & \text{and } |z| < (Z_i + Z_{i'})/2; \\ 0 & \text{otherwise,} \end{cases} \tag{4.6}$$

and the corresponding excluded-volume matrix reads

$$\mathcal{E}_{ii'} = (X_i + X_{i'})(Y_i + Y_{i'})(Z_i + Z_{i'}). \tag{4.7}$$

The equilibrium single-particle density at packing fraction $\eta = (LWT)N/V$ is obtained by minimizing the free energy Eq. (4.4) with respect to ρ_i, subject to the normalization condition

$$\sum_{i=1}^{6} \rho_i = \frac{\eta}{LWT}. \tag{4.8}$$

The symmetry of the solution of this minimization problem allows to identify the stable homogeneous phase. When $\psi_i \equiv \rho_i LWT/\eta = 1/6$ for every $i = 1, \ldots, 6$, the phase is isotropic (I). In the opposite case, when all the components ψ_i of the orientation distribution function assume different values, the phase is biaxial nematic (N_B). When the system is characterized by the presence of a single axis of symmetry (uniaxial nematic phase), the coefficients ψ_i are coupled two-by-two. Let us suppose this axis of symmetry to be the vertical axis of Fig. 3.2. In this case, we distinguish between *prolate* uniaxial nematic phase (N_+), when the most likely configurations of Fig. 3.2 are (1) and (4), and *oblate* uniaxial nematic phase (N_-), when the most likely configurations are (3) and (6).

Since we assume homogeneity, we need to estimate the limit of validity of this assumption. To this aim we adopt bifurcation theory to calculate the minimum packing fraction $\bar{\eta}$, beyond which homogeneous phases are unstable with respect to smectic states [23]. The details of this procedure are explicitly described in Sec. 3.A.1. Let us indicate with $Q^{(x)}_{ii'}(q_x)$ the function

$$Q^{(x)}_{ii'}(q_x) = \sqrt{\rho_i \rho_{i'}} \int d\mathbf{r}\, f_m^{ii'}(\mathbf{r}) \exp(-iq_x x), \tag{4.9}$$

where ρ_i is the single-particle density of the (homogeneous) equilibrium phase at packing fraction η. The functions $Q^{(y)}_{ii'}(q_y)$ and $Q^{(z)}_{ii'}(q_z)$ are defined analogously. The bifurcation packing fraction $\bar{\eta}_x$ for smectic fluctuations along the x axis is found as the minimum packing fraction at which the 6×6 matrix with entries $Q^{(x)}_{ii'}(q_x)$ has an eigenvalue 1 for some $\bar{q}_x$. Therefore, the smectic bifurcation packing fraction is $\bar{\eta} = \min(\bar{\eta}_x, \bar{\eta}_y, \bar{\eta}_z)$. As a final remark, it is important to notice that the present bifurcation analysis allows only to predict when homogeneous phases are unstable with respect to one-dimensional modulations in the single-particle density. There is no guarantee, however, that the corresponding stable inhomogeneous phase is actually characterized by one-dimensional (smectic) ordering, since two- (columnar) or three-dimensional (crystal) positional ordering are also possible in principle.

4.3 Effective depletion interaction

Our aim is to study the influence of a depletant on the phase behavior of a system of boardlike particles. Hence, the system described in Sec. 4.2 is modified by the addition of a second species of particles (the depletant), modeled as cubes with dimensions $d \times d \times d$. The binary mixture of boardlike particles and depletant is assumed to be in equilibrium with a reservoir of depletant particles at fixed fugacity $z_D = \exp(\beta\mu_D)/\mathcal{V}_D$, where μ_D is the chemical potential of the depletant and $\mathcal{V}_D$ its thermal volume. Following the pioneering approaches to the topic [71, 72], we neglect interactions between depletants, in which case the fugacity z_D coincides with the density n_D in the reservoir. The ideal-depletant assumption is justified *a posteriori* by the low packing fractions $n_D d^3$ considered. Modeling the depletant with cubic particles appears to be rather unrealistic, especially if compared to typical polymeric depletants, usually treated as spheres. However, we claim that our choice contains the essential features of the physical phenomenon, while considerably simplifying the mathematics that follows. In the next section we show that the peculiar phase behavior of our system is due to the asphericity of the depletion volume, which, in turns, is a consequence of the asphericity of boardlike particles. Therefore, we do not expect the specific shape of the depletion region (cuboidal for cubic depletant, spherocuboidal for spherical depletant) to play a major role in our results. Moreover, the relative difference between cuboidal and spherocuboidal depletion volume for the values of the particles dimensions considered here amounts to a few percentage points. The interactions in the mixture are given by the cuboid-cuboid potential Eq. (4.6) between boardlike particles, and by the cuboid-cube potential between boardlike particles and depletant, given by

$$\beta v_i(\mathbf{r}) = \begin{cases} \infty & \text{if } |x| < (X_i + d)/2 \\ & \text{and } |y| < (Y_i + d)/2 \\ & \text{and } |z| < (Z_i + d)/2; \\ 0 & \text{otherwise,} \end{cases} \tag{4.10}$$

which explicitly depends on the orientation i of the boardlike particle.

At fixed fugacity z_D the configurational entropy of the depletant is maximized when the total depletion volume, i.e., the region of space forbidden to the depletant due to the presence of boardlike particles, is minimized. As a consequence, an effective attraction between boardlike particles appears. Such a depletion interaction can be explicitly calculated by integrating out the depletant degrees of freedom and must be expressed in general as a sum of two-, three- and perhaps many-body interaction terms [92, 93]. For the sake of simplicity, we describe the effect of the depletant by considering only the effective two-body interaction potential, while neglecting higher order terms. The effective pairwise depletion potential $w_{ii'}(\mathbf{r})$ between cuboids with orientations i and i', respectively, and center-to-center separation $\mathbf{r}$ is given by [94]

$$\beta w_{ii'}(\mathbf{r}) = -n_D \mathcal{V}_{ii'}(\mathbf{r}), \tag{4.11}$$

with $\mathcal{V}_{ii'}(\mathbf{r})$ the overlap volume of the depletion regions,

$$\mathcal{V}_{ii'}(\mathbf{r}) = \begin{cases} 0 & \text{if } |x| > (2d + X_i + X_{i'})/2 \\ & \text{or } |y| > (2d + Y_i + Y_{i'})/2 \\ & \text{or } |z| > (2d + Z_i + Z_{i'})/2; \\ \lambda_{ii'}^{(x)} \lambda_{ii'}^{(y)} \lambda_{ii'}^{(z)} & \text{otherwise.} \end{cases} \tag{4.12}$$

The parameter $\lambda_{ii'}^{(x)}$ reads (cf. Appendix 4.A)

$$\lambda_{ii'}^{(x)}(x) = \begin{cases} d + \frac{X_i + X_{i'}}{2} - |x| & \text{if } |x| > \frac{|X_i - X_{i'}|}{2} \\ & \text{and } |x| < (d + \frac{X_i + X_{i'}}{2}); \\ d + \min(X_i, X_{i'}) & \text{if } |x| < \frac{|X_i - X_{i'}|}{2}, \end{cases} \tag{4.13}$$

and analogous definitions hold for $\lambda_{ii'}^{(y)}(y)$ and $\lambda_{ii'}^{(z)}(z)$.

Let us indicate with a tilde the properties obtained by adding the effective two-body depletion potential $w_{ii'}(\mathbf{r})$ to the cuboid-cuboid potential $u_{ii'}(\mathbf{r})$. The Mayer function Eq. (4.3) becomes

$$\widetilde{f}_m^{ii'}(\mathbf{r}) = \exp\big[-\beta u_{ii'}(\mathbf{r}) + n_D \mathcal{V}_{ii'}(\mathbf{r})\big] - 1. \tag{4.14}$$

The phase behavior of this effective one-component system can then be calculated by following the prescriptions of Sec. 4.2, with the function $f_m^{ii'}(\mathbf{r})$ substituted by $\widetilde{f}_m^{ii'}(\mathbf{r})$. Unfortunately, the expression of $\mathcal{V}_{ii'}(\mathbf{r})$ given in Eq. (4.12) does not allow for an analytical calculation of the integrals $\widetilde{\mathcal{E}}_{ii'}$ and $\widetilde{Q}_{ii'}^{(x)}(q_x)$ in Eqs. (4.5) and (4.9). However, an analytical expression can be obtained by inserting the small-n_D Taylor series of the Mayer function Eq. (4.14),

$$\widetilde{f}_m^{ii'}(\mathbf{r}) = f_m^{ii'}(\mathbf{r}) + \sum_{m=1}^{\infty} \frac{n_D^m}{m!} \big(\mathcal{V}_{ii'}(\mathbf{r})\big)^m \exp\big[-\beta u_{ii'}(\mathbf{r})\big], \tag{4.15}$$

into Eq. (4.5). In such a way one obtains the effective excluded-volume coefficients in terms of a series in n_D,

$$\widetilde{\mathcal{E}}_{ii'} = \mathcal{E}_{ii'} - \sum_{m=1}^{\infty} \frac{n_D^m}{m!} \int_V d\mathbf{r} \big(\mathcal{V}_{ii'}(\mathbf{r})\big)^m \exp\big[-\beta u_{ii'}(\mathbf{r})\big], \tag{4.16}$$

where the integrals of the r.h.s. can now be solved analytically for every integer m. Similar considerations hold for the functions $\widetilde{Q}_{ii'}^{(x)}(q_x)$ of Eq. (4.9). We verified by comparison with exact numerical calculations of the effective excluded-volume coefficients that quantitative agreement can be obtained by truncating the series of

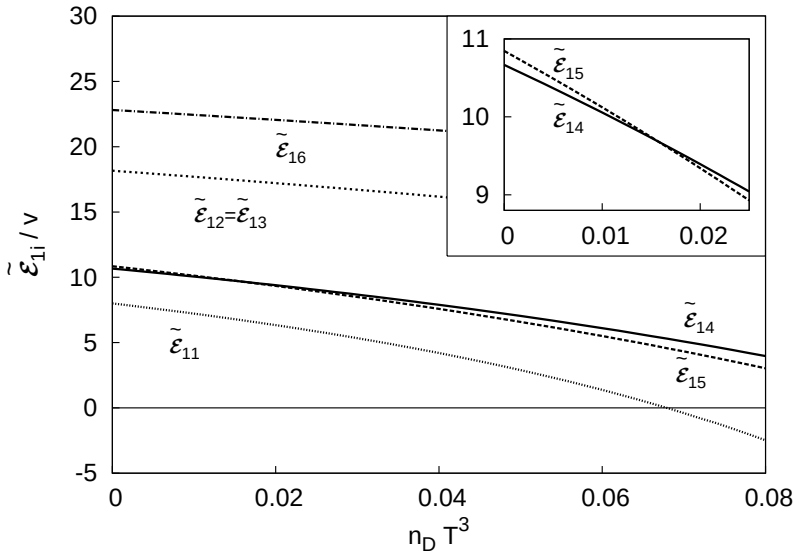

Figure 4.1: Effective excluded-volume coefficients $\widetilde{\mathcal{E}}_{1i}$ (in units of boardlike particle volume $v = LWT$) for the 6 independent orientational configurations of a pair of boardlike particles in the Zwanzig model as a function of the depletant number density n_D. Here the boardlike particles have dimensions $L/T = 9.3$, $W/T = 3.0$ and are in contact with a reservoir of ideal cubic depletants with edge-length $d/T = 1.0$ and number density n_D.

Eq. (4.16) at fifth order in n_D for all n_D considered in this chapter. For consistency, the Taylor expansion in n_D of the functions $\widetilde{Q}^{(x)}_{ii'}(q_x)$ is truncated at the same order.

4.4 Excluded-volume matrix and phase behavior

The framework developed in Sec. 4.3 allows to determine the effective excluded-volume coefficients $\widetilde{\mathcal{E}}_{ii'}$ of a system of cuboidal $L \times W \times T$ particles due to the presence of an ideal cubic $d \times d \times d$ depletant at fugacity z_D (and reservoir density $n_D = z_D$). The phase behavior of this effective one-component system of boardlike particles is then analyzed by applying the theory described in Sec. 4.2.

It is readily understood from Eq. (4.16) that adding the depletion attraction Eq. (4.11) to the cuboid-cuboid pairwise potential $u_{ii'}(\mathbf{r})$ gives rise to a monotonic decrease of the coefficients $\widetilde{\mathcal{E}}_{ii'}$ with n_D. This effect is depicted in Fig. 4.1, where we report the 6 independent values of the matrix elements $\widetilde{\mathcal{E}}_{1i}$, corresponding to the 6 two-particle configurations (1,1), (1,2), (1,3), (1,4), (1,5) and (1,6) (cf. Fig. 3.2 for a visual inspection of the six one-particle orientations), as a function of the reservoir depletant concentration n_D. In order to allow for a comparison with previous

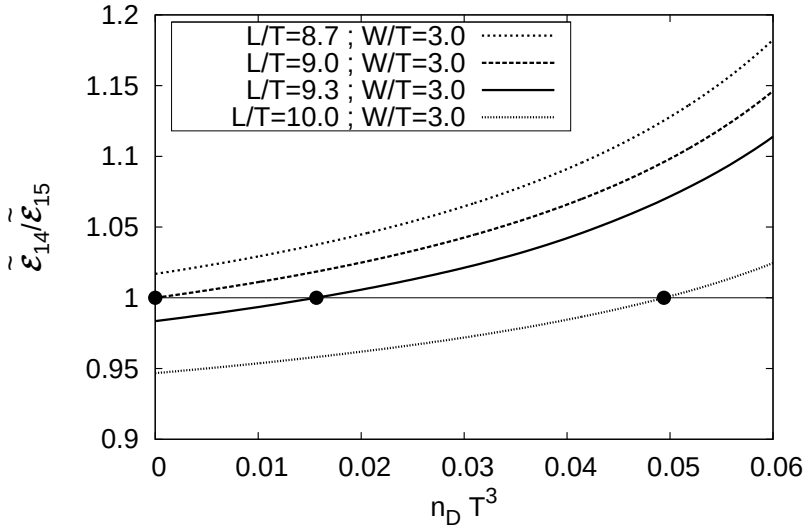

Figure 4.2: Ratio between the second-virial coefficients corresponding to the two-particle configurations (1,4) and (1,5) of Fig. 3.2 as a function of the depletant density n_D for boardlike particles with $W/T = 3.0$ and $L/T = 8.7$ ($\nu = L/W - W/T = -0.1$), $L/T = 9.0$ ($\nu = 0.0$), $L/T = 9.3$ ($\nu = 0.1$), and $L/T = 10.0$ ($\nu = 0.33$). The solid circles highlight the value of the depletant density n_D^*, defined by the condition $\widetilde{\mathcal{E}}_{14} = \widetilde{\mathcal{E}}_{15}$.

experimental [45] and theoretical (cf. Sec. 3) work on the subject, the aspect ratios are chosen as $L/T = 9.3$ and $W/T = 3.0$, while for the cubic depletant we set $d/T = 1.0$. At $n_D = 0$ the 6 excluded-volume matrix elements are positive definite, but with increasing n_D their value decreases until becoming negative (see $\widetilde{\mathcal{E}}_{11}$ in Fig. 4.1). Such a behavior is well known from the study of systems of spherically symmetric particles with short-range attractive potentials, where one can define a temperature at which the second virial coefficient changes its sign ("Boyle temperature"). The change in sign of the second-virial coefficient is related to a tendency of the system to develop a gas-liquid phase separation. Also in the present case, where the role of the (inverse) temperature is played by the depletant density n_D, this change in sign can indicate a tendency towards a phase separation between two homogeneous phases. On the other hand, when the dimension of the depletant is sufficiently small, one expects the gas-liquid phase separation to be metastable with respect to a broad gas-solid coexistence [84, 86, 92, 93]. As we ignore the stability of inhomogeneous phases like smectic, columnar or crystal states, in the present work we limit our investigations to values of n_D small enough as to guarantee a positive value of all the effective excluded-volume matrix elements, and to avoid strong tendency towards a broad phase separation.

Although the monotonic decrease with n_D is a feature of all the 6 effective excluded-volume coefficients $\widetilde{\mathcal{E}}_{1i}$, their rate of change is not the same. Let us focus on the coefficients corresponding to the two-particle configurations (1,4) and (1,5). In absence of depletant ($n_D = 0$), $\widetilde{\mathcal{E}}_{15} = \mathcal{E}_{15}$ is slightly bigger than $\widetilde{\mathcal{E}}_{14} = \mathcal{E}_{14}$. On the other hand, by increasing n_D the coefficient $\widetilde{\mathcal{E}}_{15}$ decreases faster than $\widetilde{\mathcal{E}}_{14}$. As a consequence, one can identify a value of the depletant density n_D^*, such that $\widetilde{\mathcal{E}}_{14} = \widetilde{\mathcal{E}}_{15}$. Moreover, $\widetilde{\mathcal{E}}_{14} < \widetilde{\mathcal{E}}_{15}$ for $n_D < n_D^*$, the opposite being the case for $n_D > n_D^*$ (see inset of Fig. 4.1). An alternative representation of this phenomenon is reported in Fig. 4.2, where we plot the ratio $\widetilde{\mathcal{E}}_{14}/\widetilde{\mathcal{E}}_{15}$ as a function of the depletant density n_D for fixed aspect ratios $W/T = 3.0$ and $d/T = 1.0$ and different values of L/T ($L/T = 8.7$, 9.0, 9.3 and 10.0). In the four cases reported in Fig. 4.2 we observe a monotonically increasing dependence of $\widetilde{\mathcal{E}}_{14}/\widetilde{\mathcal{E}}_{15}$ on n_D. This implies that the density n_D^*, defined by the condition $\widetilde{\mathcal{E}}_{14}/\widetilde{\mathcal{E}}_{15} = 1$, exists only if $\mathcal{E}_{14}/\mathcal{E}_{15} \leq 1$. In other words, a positive (i.e., physical) n_D^* exists only if $\mathcal{E}_{14} \leq \mathcal{E}_{15}$, with $n_D^* = 0$ if and only if $\mathcal{E}_{14} = \mathcal{E}_{15}$. On the contrary, if $\mathcal{E}_{14} > \mathcal{E}_{15}$ one has $\widetilde{\mathcal{E}}_{14} > \widetilde{\mathcal{E}}_{15}$ independently of the depletant density n_D, and no density n_D^* is defined in this case. Finally, it is important to notice that the ratio $\mathcal{E}_{14}/\mathcal{E}_{15}$ depends of the aspect ratios of the boardlike particles L/T and W/T only.

Before addressing the physical consequences of the existence of the density n_D^*, it is worth seeing how in mean-field theory the ratio of the excluded volume coefficients $\mathcal{E}_{14}/\mathcal{E}_{15}$ determines the phase behavior of boardlike particles in the absence of a depletant (i.e., $n_D = 0$). It is well known that monodisperse hard boardlike particles are expected to undergo an I-N transition by increasing the packing fraction of the system [34]. The nematic phase emerging from the I can be (i) *uniaxial prolate* N_+ with common alignment of the long axis L of the boards; (ii) *uniaxial oblate* N_- with common alignment of the short axis T; (iii) *biaxial* N_B with alignment of the three axes of the particle (cf. the pictorial representations in Fig. 3.1). Following Onsager [24], the origin of this phase transition can be understood by considering that orientational ordering determines an increase in excluded-volume entropy, which more than compensates the decrease in orientational entropy. Therefore, in case $\mathcal{E}_{14} < \mathcal{E}_{15}$ the N_+ phase will be thermodynamically favored over the N_-, the opposite being the case when $\mathcal{E}_{14} > \mathcal{E}_{15}$ (cf. the pair configurations (1)-(4) and (1)-(5) in Fig. 3.2). In the intermediate situation, when $\mathcal{E}_{14} = \mathcal{E}_{15}$, the system undergoes a direct second-order I-N_B transition instead. By explicitly calculating $\mathcal{E}_{14}$ and $\mathcal{E}_{15}$ in terms of particle's size L, W and T, and defining as in Sec. 3.3 a shape parameter

$$\nu = \frac{L}{W} - \frac{W}{T}, \tag{4.17}$$

one can show that

$$\frac{\mathcal{E}_{14}}{\mathcal{E}_{15}} \begin{cases} < 1 & \Leftrightarrow \nu > 0, \\ = 1 & \Leftrightarrow \nu = 0, \\ > 1 & \Leftrightarrow \nu < 0. \end{cases} \tag{4.18}$$

This is consistent with Straley's result that at the mean-field level a system of boardlike particles undergoes (i) a first-order IN_+ transition if $\nu > 0$; (ii) a first-order IN_- transition if $\nu < 0$; (iii) a second-order IN_B transition if $\nu = 0$ [47].

4.5 Phase diagram of attractive boardlike particles

We can now go back to the case of boardlike particles dispersed with a non-adsorbing depletant at density n_D. We have shown in Fig. 4.2 that we can control the ratio $\widetilde{\mathcal{E}}_{14}/\widetilde{\mathcal{E}}_{15}$ by varying the depletant density n_D. By analogy with the monodisperse case (cf. Eq. (4.18)), we expect n_D to allow us to tune the stability of prolate uniaxial, oblate uniaxial and biaxial nematic states. In other words, we expect the system to favor prolate uniaxial ordering N_+ in the case $n_D < n_D^*$, since $\widetilde{\mathcal{E}}_{14}/\widetilde{\mathcal{E}}_{15} < 1$, and oblate uniaxial N_- in the case $n_D > n_D^*$. On the other hand, we expect a direct continuous IN_B transition if $n_D = n_D^*$, since then the tendencies to form oblate and prolate ordering are perfectly balanced and $\widetilde{\mathcal{E}}_{14} = \widetilde{\mathcal{E}}_{15}$. Such a direct second-order IN_B transition corresponds to a Landau critical point, hence we refer to n_D^* as the *critical depletant density*.

This picture is confirmed by the (η, n_D) phase diagrams of Fig. 4.3, describing the phase behavior of boardlike particles with dimensions $W/T = 3.0$ and (a) $L/T = 8.7$ ($\nu = -0.1$), (b) $L/T = 9.0$ ($\nu = 0.0$), (c) $L/T = 9.3$ ($\nu = 0.1$), and (d) $L/T = 10.0$ ($\nu = 0.33$) immersed in a cubic depletant with edge-length $d/T = 1.0$ and number density n_D. As a general feature, at low packing fraction the system undergoes a phase transition from the I phase (yellow region) to the N_+ (red regions), N_- (blue regions) or N_B (green regions) states. The first-order character of the IN_+ and IN_- transitions is not detectable on the scale of Fig. 4.3 (cf. also Appendix 3.A.2). The dotted lines indicate the limit of stability of the homogeneous phases with respect to one-dimensional (smectic, Sm) fluctuations along the long axis L (red dotted lines) or along the short axis T (blue dotted lines). This smectic bifurcation analysis confirms that inhomogeneous phases (white regions) destabilize nematic states at sufficiently high packing fractions. More specifically, the higher the depletant density n_D, the lower the stability of homogeneous phases with respect to inhomogeneous ones. This result is in agreement with previous studies on the phase behavior of hard rods interacting via an attractive depletion potential [84, 86]. In the latter case the coexistence regions increase with the depletant density, leading eventually to a wide isotropic-crystal coexistence at sufficiently high n_D and a consequent disappearance of the liquid-crystal phases. We expect a similar phenomenon at depletant concentrations higher than those considered here. However, a description beyond the second virial order would be needed in that case.

As deduced from the analysis of Fig. 4.2, in the case of "platelike" boards, that is, boardlike particles characterized by a shape parameter $\nu < 0$, no critical depletant density is defined. This implies that the I phase undergoes a transition to the N_- for every value of n_D, as depicted in the phase diagram of Fig. 4.3(a). Let us now consider the phase behavior of boardlike particles with $\nu = 0$ reported in Fig. 4.3(b).

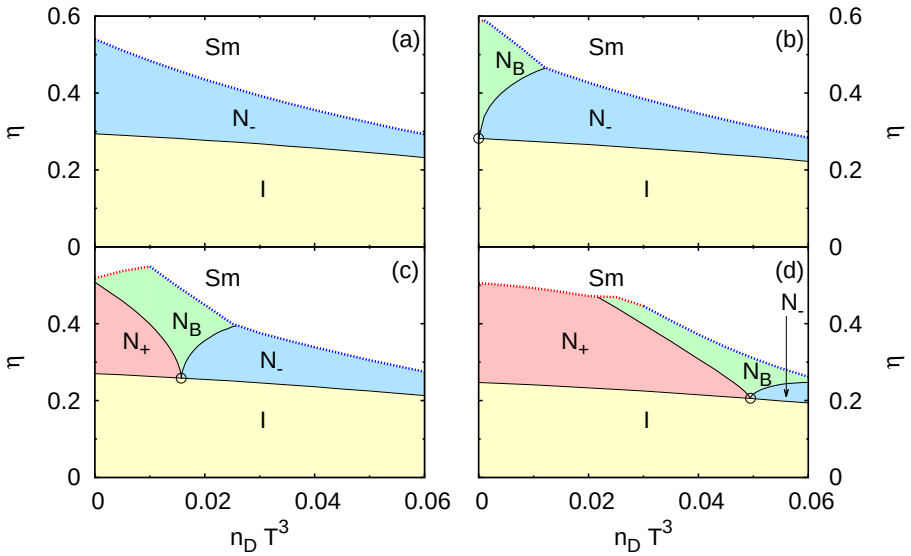

Figure 4.3: Phase diagrams of boardlike particles with aspect ratios $W/T = 3.0$ and (a) $L/T = 8.7$ ($\nu = -0.1$), (b) $L/T = 9.0$ ($\nu = 0.0$), (c) $L/T = 9.3$ ($\nu = 0.1$), (d) $L/T = 10.0$ ($\nu = 0.33$) in contact with a reservoir of cubic depletant with edge-length length $d/T = 1.0$ at number density n_D. The diagrams feature isotropic (I, yellow regions), prolate (N_+, red regions) and oblate (N_-, blue regions) uniaxial and biaxial (N_B, green regions) nematic phases. The black circles highlight the Landau critical points, whereas the dotted lines indicate the limit of stability of nematic phases with respect to smectic (Sm) fluctuations along the long (red dotted line) and short (blue dotted line) particle axis, respectively.

In absence of depletant a direct second-order IN_B transition is expected in this case [34, 47]. In the picture we presented in the previous section, this corresponds to a critical depletant density at $n_D^* = 0$. For values of the depletant density $n_D > n_D^* = 0$, at intermediate packing N_- states appear in between the I and the N_B phase. The phase diagram of this boards-depletant mixture becomes even more rich when considering "rodlike" boards, for which $\nu > 0$, as reported in Figs. 4.3(c) and (d). As described in the previous section, in this case one can identify a non-zero critical depletant density $n_D^* > 0$. The pure system, for which $n_D = 0$, is characterized by an IN_+ transition. However, adding the depletant to the suspension has the effect of reducing the N_+ stability in favor of the N_B. Furthermore, when reaching the critical depletant concentration n_D^*, one observes a direct IN_B transition. Surprisingly, at even higher depletant densities, that is when $n_D > n_D^*$, the stable uniaxial nematic phase has oblate ordering N_-, in sharp contrast with the behavior of the pure boards. It is worth remarking that the phase diagrams of Figs. 4.3(c) and (d) suggest that, when dealing with boardlike particles with $\nu > 0$, setting the depletant density at

values close to n_D^* allows to select regions of the phase diagram with relatively high N_B stability. This appears to be possible even when the regime of N_B stability for the pure boardlike particles system is small (Fig. 4.3(c)) or even absent (Fig. 4.3(d)).

A relevant result of the present analysis concerns the conditions for the existence of the critical depletant density n_D^*, which is guaranteed only for slightly elongated rodlike boards ($\nu > 0$). On the contrary, no Landau critical point is observed when $\nu < 0$, in which case for every value of n_D the system develops a first-order $I N_-$ transition, typical of platelike particles. We interpret this fact in the following terms. When the depletant density is low, the boardlike particles are weakly sensitive to the depletant and the features of the nematic phase are driven by the gain in boardlike particles' excluded-volume entropy. In other words, at low depletant concentration one has N_+ (N_-) ordering if $\nu > 0$ ($\nu < 0$), with no qualitative change with respect to the phase diagram of the pure system. On the other hand, at high enough depletant density the thermodynamically favored states are those maximizing the depletant (positional) entropy, i.e., states where the overall depletion volume is minimized. From geometric considerations it is easily realized that N_- rather than N_+ ordering tends to maximize the overlap between the depletion regions of the boards *independently* of the sign of ν. As a consequence, when $\nu > 0$ the Landau critical point at n_D^* appears as a result of a competition between the excluded-volume entropy of boardlike particles and depletant. Conversely, this competition does not develop when $\nu < 0$, since both boards and depletant entropies are maximized by N_- states, and thus no critical depletant density exists.

4.6 Estimating the critical depletant density

The phase diagrams of Fig. 4.3 highlight the monotonic increasing dependence of n_D^* on $\nu = L/W - W/T$, when the dimensions of the depletant d/T and one of the two boards' aspect ratios (here W/T) are fixed. It is interesting to deduce the phase behavior, and more specifically the critical depletant density, in more general terms. By numerically solving in n_D the equation $\widetilde{\mathcal{E}}_{14} = \widetilde{\mathcal{E}}_{15}$, whose solution defines in this model the critical depletant density n_D^*, we investigate in this section the role of the depletant size and the shape of the boardlike particles.

In Fig. 4.4 we report the critical depletant density n_D^* as a function of the depletant edge-length d/T for three boardlike particle dimensions. By increasing the size of the depletant, the critical depletant number density n_D^* decreases. This trend can be understood by considering the definition of the depletant potential Eq. (4.11), according to which the intensity of the interaction is determined both by the depletant density and the volume of the depletion regions. This means that if the size of the depletant (and therefore the depletion volume) is reduced, in order to have the same interaction strength one needs to increase the depletant density. Furthermore, at fixed ν the critical depletion density decreases most for the more extreme aspect ratios of the particles. In other words, the bigger the aspect ratios L/T and W/T at fixed ν, the smaller the amount of depletant needed to reach n_D^*. By changing

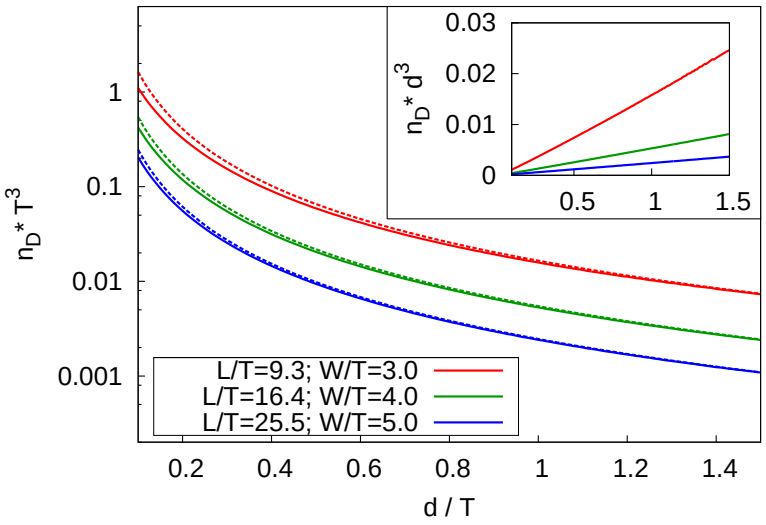

Figure 4.4: Critical depletant density n_D^* as a function of the edge-length d of the cubic depletant for different boardlike particles with the same shape parameter $\nu = 0.1$: $L/T = 9.3$ and $W/T = 3.0$ (solid red line); $L/T = 16.4$ and $W/T = 4.0$ (solid green line); $L/T = 25.5$ and $W/T = 5.0$ (solid blue line). The dashed lines represent the approximate analytical dependence given by Eq. (4.19). The inset illustrates the same data in terms of the critical depletant packing fraction $n_D^* d^3$.

our unit of length, we consider in the inset of Fig. 4.4 the critical depletant packing fraction $n_D^* d^3$, which appears to be an increasing function of d. This observation allows us to conclude that the ideal depletant approximation introduced in Sec. 4.3 is increasingly reliable the smaller the depletants.

In practical situations, one could be interested in estimating the critical depletant density n_D^*, which in our model is defined as the solution of the non-linear equation $\widetilde{\mathcal{E}}_{14} = \widetilde{\mathcal{E}}_{15}$. If n_D^* is sufficiently small, one can obtain an approximate expression for this quantity by linearizing both sides of equation $\widetilde{\mathcal{E}}_{14} = \widetilde{\mathcal{E}}_{15}$ in n_D. The approximate critical depletant density is then given by the following expression

$$n_D^* = \frac{2\big[T(L+W)^2 - L(W+T)^2\big](L-T)^{-1}}{2(LT-W^2)d^3 + W(LW+TW-2LT)d^2}, \tag{4.19}$$

and it can be compared (dotted lines of Fig. 4.4) with the "exact" numerical solution (solid lines), showing good overall agreement, which improves the larger the depletant edge-length d/T.

4.7 Conclusions

In the present chapter we investigate the effect of a short-range depletion-induced attraction on the liquid-crystal phase behavior of boardlike particles. To this aim, we make use of classical density functional theory truncated at second-virial order, and adopt the Zwanzig model for the description of the orientational degrees of freedom. In close analogy with the Asakura-Oosawa-Vrij model for mixtures of spheres, by neglecting interactions between the cubic depletant particles, we can explicitly calculate the effective two-body attractive depletion potential between boardlike particles.

We predict that in systems of slightly elongated boardlike particles ($\nu > 0$) a critical depletant density exists. At this critical depletant density the first-order transition from the isotropic to a uniaxial nematic phase is substituted by a continuous transition to a biaxial nematic phase. At higher depletant concentrations, a large region of oblate uniaxial nematic ordering develops. This means that the system of attractive "rodlike" boards behaves like a system of purely repulsive "platelike" boards. The origin of this phenomenon is due to two competing mechanisms: the maximization of the boardlike particles entropy, favoring N_+ ordering, and the maximization of the depletant entropy, favoring N_- ordering.

The phase behavior described in this work shares many similarities with the findings of Chapter 3. In Chapter 3 we showed that size-polydispersity in a system of hard boardlike particles induces the appearance of a Landau tetracritical point at a specific composition. This phenomenon is related to a competition between prolate and oblate ordering, which in turn is realized only when the boardlike particles are slightly elongated. In the light of our present findings, we suggest that this prolate-oblate (N_+N_-) competition and the corresponding emergence of a Landau tetracritical point can be understood in terms of a depletion effect. More specifically, when size-polydispersity becomes relevant, N_- rather than N_+ ordering allows for the highest total entropy due to the minimization of the overall depletion regions of the big particles with respect to the smaller ones. In further analogy with the boards-depletant mixture, no such competition is predicted for platelike boards. Consequently, no tetracritical point appears in this case.

Besides furnishing an explanation for the results of Chapter 3, we suggest that manipulating the attraction induced by a depletant, e.g. a non-adsorbing polymer, furnishes an original and effective way to control the phase behavior of boardlike particles, allowing to stabilize prolate and oblate uniaxial and biaxial nematic states. Moreover, the depletant density is expected to be an easy experimental control parameter.

Acknowledgements

It is our pleasure to thank R. Kamien for suggesting, during the 8th Liquid Matter Conference in Vienna, to interpret the results of Chapter 3 as a depletion effect. We

would also like to thank R. Ni for stimulating discussions.

4.A Appendix: Overlap volume of the depletion regions

In this appendix we calculate explicitly the overlap volume of the depletion regions for the model described in Sec. 4.2 and 4.3. The depletion region of a $L \times W \times T$ cuboidal colloid is the region of space excluded to the center of mass of the cubic $d \times d \times d$ depletants, and it is also a cuboid with dimensions $(L+d) \times (W+d) \times (T+d)$. Moreover, also the overlap volume between two depletion regions is a cuboid, whose volume $\mathcal{V}_{ii'}(\mathbf{r})$ depends on the reciprocal position $\mathbf{r} = \mathbf{r}_1 - \mathbf{r}_2$ and the orientations i and i' of the two colloids. We calculate the volume of the overlap region by multiplying its edge lengths $\lambda_{ii'}^{(x)}$, $\lambda_{ii'}^{(y)}$ and $\lambda_{ii'}^{(z)}$ along the x, y and z axes (cf. Eq. (4.12)). Let us focus here on the x axis, and let us indicate with $L_1 = X_i + d$ and $L_2 = X_{i'} + d$ the edge length along the x axis of the depletion regions of particle 1 and 2, respectively (cf. the definition of X_i in Sec. 4.2). Moreover, let x_1 and x_2 be the x coordinates of the position of the center of mass of the two particles. Now, we have to consider separately the two cases reported in Fig. 4.5(a) and (b). If $|x_1 - x_2| > |L_1 - L_2|/2$ (Fig. 4.5(a)) the length of the overlap region explicitly depends on the reciprocal distance $|x_1 - x_2|$ as

$$\lambda^{(x)} = \frac{L_1 + L_2}{2} - |x_1 - x_2|. \tag{4.20}$$

On the other hand, if $|x_1 - x_2| < |L_1 - L_2|/2$ (Fig. 4.5(b)) the size of the overlap region takes the constant value

$$\lambda^{(x)} = \min(L_1, L_2), \tag{4.21}$$

and one deduces Eq. (4.13).

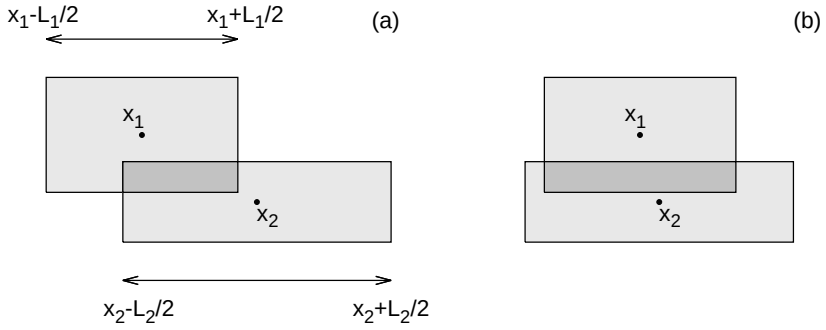

Figure 4.5: Pictorial representation of two overlapping rectangles with center of mass positions on the horizontal axis x_1 and x_2, respectively. Their edge length on the horizontal axis is L_1 and L_2, respectively. In the two pictures we report the case (a) $|x_1 - x_2| > |L_1 - L_2|/2$ and (b) $|x_1 - x_2| < |L_1 - L_2|/2$.

Chapter 5

Freezing of parallel hard squares and cubes

Abstract

Due to remarkable advances in colloid synthesis techniques, systems of squares and cubes, once an academic abstraction for theorists and simulators, are nowadays an experimental reality. By means of a free minimization of the free-energy functional, we apply the fundamental measure theory to analyze the phase behavior of parallel hard squares and hard cubes. We compare our results with those obtained by the traditional approach based on the Gaussian parameterization, finding small deviations and good overall agreement between the two methods. For hard squares our predictions feature at intermediate packing fraction a smectic phase, which is however expected to be unstable due to thermal fluctuations that are not properly included at the present mean-field level. Due to this inconsistency we cannot determine unambiguously the prediction of the theory for the expected fluid-to-crystal transition of parallel hard squares, but we deduce two alternative scenarios: (i) a second-order transition with a vacancy-rich crystal or (ii) a higher-density first-order transition with a coexisting crystal characterized by a lower vacancy concentration. In accordance with previous studies, a second-order transition with a high vacancy concentration in the crystal is predicted for hard cubes.

5.1 Introduction

Hard spheres represent the simplest and most versatile model for the description of molecular and colloidal many-particle systems. This statement has particularly been true since 1957, when Wood and Jacobson [95] and Alder and Wainwright [96] demonstrated that hard spheres undergo a fluid-to-crystal transition, and therefore that hard interactions alone can account for freezing.

Systems of hard cubes, on the other hand, were considered as mere toy models until only a few years ago. The reason for this is evident: no molecule or macromolecular aggregate found in nature is known to be reasonably approximated by this

shape. However, the interaction between parallel hard cubes is the second-simplest hard interaction one can imagine after that between hard spheres. Its simplicity made this model a perfect object of study for theory and simulation.

Early studies on the equation of state of parallel hard squares ($D = 2$ dimensions) and cubes ($D = 3$) date back to the dawn of computer simulation in the 1950s [97–99]. Soon after, the question regarding the high-packing phase behavior of the models arose. For parallel hard squares, a transition from the fluid to a square-lattice crystal (with quasi-long-range order) was found [100, 101], but its character, whether continuous or discontinuous, has been a matter of debate ever since [102–105]. Conversely, the stability of a "brick-wall" smectic phase with one-dimensional ordering in rows (or columns) was suggested to exist for parallel hard squares, but the stability of this peculiar state was soon ruled out [106]. Similarly, parallel hard cubes manifest a fluid-to-crystal transition with a well-established second-order character [107], and no stable phase with lower translational symmetry than the crystal is expected [108].

In the mid-1990s, while the interest of the liquid-state community was focusing on mixtures of hard spheres, hard cubes were rediscovered. By means of computer simulation Dijkstra et al. showed evidence of a demixing transition in a binary system of parallel hard cubes on a lattice, thus demonstrating that additive hard interactions can induce an entropy-driven fluid-fluid phase separation [109, 110]. These results motivated Cuesta and Martínez-Ratón to face the problem by means of density functional theory [111, 112]. Following the pioneering approach developed by Rosenfeld for hard spheres [26], they developed a fundamental measure theory (FMT) [28, 29] formalism aimed at describing both the homogeneous and inhomogeneous phase behavior of mixtures of squares and cubes [111, 112].

Since the early work on hard squares and cubes, the progress in colloidal particle synthesis has been enormous. In particular, colloidal suspensions of micron-sized cubes [113] and quasi-two-dimensional square platelets [114] have been recently produced and analyzed. These experimental advances led to a renewed interest in the model, and at present more complex aspects like the role of orientational degrees of freedom, the addition of dipolar interactions, the roundedness of the shape and the effect of vacancies in the freezing mechanism constitute objects of intense research [115–120]. Far from being a toy model or a mere academic exercise, squares and cubes have therefore gained a key role as model systems of non-spherical colloidal particles.

Besides the development of new theories [121, 122], the increasing attention towards the self-assembly of non-spherical particles requires a detailed analysis of the capabilities of the existing ones. The aim of this work is to reinvestigate the prediction of the fundamental measure theory as formulated in Ref. [111] for the phase behavior of parallel hard squares and cubes. The focus of our attention points to the freezing transition and the structure of the high-density inhomogeneous phases. In particular, by exploiting present-day computer power we improve previous analyses on the subject by performing a *free minimization* of the density functional, and compare our results with those obtained by means of the widely applied Gaussian

parameterization of the single-particle density. We observe good overall agreement between the two methods, the main drawbacks of the Gaussian parameterization being (i) a systematic albeit small underestimation of the equilibrium vacancy concentration in the crystal and (ii) the lack of anisotropy of the crystal density peaks at high enough density. Furthermore, to the best of our knowledge this work constitutes the first density-functional theory study of the hard-square system. We show that the fundamental measure theory surprisingly predicts a smectic phase absent in computer simulation and we suggest that, in analogy with the hard-cube system, vacancies can play a crucial role in the freezing transition.

5.2 Model and theory

The density-functional theory route to the equilibrium properties of a many-body system consists of expressing the intrinsic Helmholtz free energy $\mathcal{F}$ as a functional of the single-particle density $\rho(\mathbf{r})$ (see Sec. 2.3). When considering a system composed of a single species of particles having only translational (and no rotational) degrees of freedom in D dimensions, the free-energy functional reads

$$\beta\mathcal{F}[\rho] = \int d^D\mathbf{r}\, \rho(\mathbf{r})\Big\{\log[\rho(\mathbf{r})\mathcal{V}]-1\Big\} + \beta\mathcal{F}^{\text{exc}}[\rho], \tag{5.1}$$

where $\mathbf{r}$ is a D-dimensional vector, $\beta = (k_B T)^{-1}$ is the inverse temperature in units of the Boltzmann constant, $\mathcal{V}$ the thermal volume and the integrals are performed over the (D-dimensional) volume V occupied by the system. The first term in the right-hand side of Eq. (5.1) denotes the ideal-gas contribution, while the second describes the excess contribution due to particle-particle interactions.

5.2.1 Fundamental Measure Theory (FMT)

The excess free-energy functional $\mathcal{F}^{\text{exc}}[\rho]$ in Eq. (5.1) is the non-trivial element of the theory: it contains the free-energy dependence on the inter-particle interactions and it can not be calculated exactly in general.

Various methods to systematically estimate this functional dependence have been developed. For hard spheres the undoubtedly most successful approach is that of the fundamental measure theory (FMT). According to FMT, the excess free energy is written as

$$\beta\mathcal{F}^{\text{exc}}[\rho] = \int d^D\mathbf{r}\, \Phi^{(D)}\big(\{n_\alpha(\mathbf{r})\}\big), \tag{5.2}$$

where $\{n_\alpha(\mathbf{r})\}$ is a set of weighted densities, labeled by α, obtained as convolutions between the single-particle density and a set of corresponding weight functions $w_\alpha(\mathbf{r})$,

$$n_\alpha(\mathbf{r}) = \int d^D\mathbf{r}'\,\rho(\mathbf{r}')w_\alpha(\mathbf{r}-\mathbf{r}'). \tag{5.3}$$

The functional dependence of $\Phi^{(D)}\big(\{n_\alpha\}\big)$ is determined by extrapolating from known limiting cases, such as the homogeneous bulk equation of state, the low-density second-virial behavior, and the dimensional crossover to highly confined conditions [28, 29].

For hard parallel squares ($D = 2$) and cubes ($D = 3$) with side σ, the FMT functional was determined by Cuesta and Martínez-Ratón in Ref. [111]. In what follows, we report their explicit expression of $\Phi^{(D)}\big(\{n_\alpha\}\big)$ for the single-component case. Following Ref. [111] we introduce the auxiliary functions

$$\tau(x) = \Theta\left(\frac{\sigma}{2} - |x|\right), \qquad \zeta(x) = \frac{1}{2}\delta\left(\frac{\sigma}{2} - |x|\right), \tag{5.4}$$

defined for $x \in \mathbb{R}$.

For parallel squares the weight functions are

$$w_0(\mathbf{r}) = \zeta(x)\zeta(y); \tag{5.5a}$$
$$\mathbf{w}_1(\mathbf{r}) = \big(\zeta(x)\tau(y), \tau(x)\zeta(y)\big); \tag{5.5b}$$
$$w_2(\mathbf{r}) = \tau(x)\tau(y), \tag{5.5c}$$

where we note that $\mathbf{w}_1$ has a vector character. The functional dependence of the excess free energy of parallel squares is given by

$$\Phi^{(2)} = -n_0\log\big(1-n_2\big) + \frac{n_1^{(x)}n_1^{(y)}}{1-n_2}. \tag{5.6}$$

For parallel cubes the weight functions are

$$w_0(\mathbf{r}) = \zeta(x)\zeta(y)\zeta(z); \tag{5.7a}$$
$$\mathbf{w}_1(\mathbf{r}) = \big(\tau(x)\zeta(y)\zeta(z), \zeta(x)\tau(y)\zeta(z), \zeta(x)\zeta(y)\tau(z)\big); \tag{5.7b}$$
$$\mathbf{w}_2(\mathbf{r}) = \big(\zeta(x)\tau(y)\tau(z), \tau(x)\zeta(y)\tau(z), \tau(x)\tau(y)\zeta(z)\big); \tag{5.7c}$$
$$w_3(\mathbf{r}) = \tau(x)\tau(y)\tau(z); \tag{5.7d}$$

and

$$\Phi^{(3)} = -n_0\log\big(1-n_3\big) + \frac{\mathbf{n_1}\cdot\mathbf{n_2}}{1-n_3} + \frac{n_2^{(x)}n_2^{(y)}n_2^{(z)}}{(1-n_3)^2}. \tag{5.8}$$

5.2.2 Functional minimization

Once an explicit expression for the functional dependence of $\mathcal{F}^{\text{exc}}$ on the single-particle density $\rho(\mathbf{r})$ is established, the equilibrium Helmholtz free energy $F(T, V, N)$ of N particles at temperature T in a volume V (area A for $D = 2$) is obtained as the minimum of Eq. (5.1) with respect to $\rho(\mathbf{r})$ under the constraint that

$$\int d^D\mathbf{r}\,\rho(\mathbf{r}) = N. \tag{5.9}$$

In the case of hard-core interactions between the particles, the system is athermal and its thermodynamic state is completely identified by the packing fraction $\eta = Nv_p/V$, where $v_p = \sigma^3$ is the particle's volume (for $D = 2$ dimensions $\eta = Na_p/A$ and $a_p = \sigma^2$ is the particle's area).

The numerically easiest way to solve the functional minimization problem consists of expressing the single-particle density in terms of a limited number of variational parameters. After inserting this ansatz into the free energy, the latter is minimized with respect to the variational parameters to obtain an estimate of the free energy at equilibrium. This approach has been widely applied in studying the freezing transition of hard spheres, where the single-particle density was parameterized as a sum of Gaussian functions centered on the lattice sites of the expected stable crystal phase (*Gaussian parameterization* or *ansatz*) [27, 123, 124]. In this chapter we investigate the freezing transition of squares and cubes into square and simple-cubic crystal phases, for which the Gaussian ansatz can be expressed as

$$\rho_{\gamma,\lambda}(\mathbf{r}) = \eta\left(\frac{\lambda}{\sigma}\right)^D\left(\frac{\gamma}{\pi}\right)^{\frac{D}{2}}\sum_{\mathbf{n}\in\mathbb{Z}^D}\exp\Big[-\gamma(\mathbf{r}-\lambda\mathbf{n})^2\Big]. \tag{5.10}$$

In Eq. (5.10) the variational parameters are half the inverse variance γ and the lattice constant λ. Note that the lattice constant λ is related to the vacancy concentration of the crystal $x_{\text{vac}} = (N_{\text{sites}} - N)/N_{\text{sites}}$ through $x_{\text{vac}} = 1 - \eta(\lambda/\sigma)^D$, where N_{sites} is the total number of sites.

An alternative to the Gaussian parameterization consists of the numerical solution of the Euler-Lagrange equation associated with the minimization problem (*free minimization*) [125–128]. The mathematical accuracy of the free minimization method, according to which no particular functional form is imposed to the solution of the problem, is particularly relevant for the description of detailed characteristics of the density distribution (e.g. the anisotropy of its peaks). In the canonical ensemble the Euler-Lagrange equation reads (cf. Eq. 2.33)

$$\rho(\mathbf{r}) = N\exp\Big[-\frac{\delta\beta\mathcal{F}^{\text{exc}}}{\delta\rho(\mathbf{r})}\Big]\left\{\int d^D\mathbf{r}'\,\exp\Big[-\frac{\delta\beta\mathcal{F}^{\text{exc}}}{\delta\rho(\mathbf{r}')}\Big]\right\}^{-1}. \tag{5.11}$$

At high packing fraction η one expects the free energy to be minimized by inhomogeneous solutions characterized by spatial modulations of $\rho(\mathbf{r})$ along one or more

directions, representing, e.g., smectic, columnar, or crystal phases. In practice, these spatial modulations must be inserted explicitly into Eq. (5.11) by means of a Fourier series expansion. Therefore, the single-particle density of a phase characterized by a d-dimensional spontaneous breaking of the translational symmetry ($d \leq D$) is obtained by solving the following equation

$$\rho(\mathbf{s}) = \eta \frac{\lambda^d}{\sigma^D} \exp\Big[-\frac{\delta\beta\mathcal{F}^{\rm exc}}{\delta\rho(\mathbf{s})}\Big] \Big\{ \int_\Gamma d^d\mathbf{s}' \exp\Big[-\frac{\delta\beta\mathcal{F}^{\rm exc}}{\delta\rho(\mathbf{s}')}\Big] \Big\}^{-1}, \tag{5.12}$$

where $\mathbf{s} \in \Gamma$ is a d-dimensional vector, $\Gamma = [-\lambda/2, \lambda/2]^d$ and λ is the periodicity of the inhomogeneous solution (assumed to be the same along all the d directions). The minimization procedure consists of (i) solving in $\rho(\mathbf{s})$ Eq. (5.12) at fixed λ; (ii) evaluating the free-energy Eq. (5.1) associated with this solution; (iii) repeating this operation for different values of λ until the minimum of the free energy in λ is found. For hard squares ($D = 2$) we will see that Eq. (5.12) describes smectic (Sm, $d = 1$) and square crystal (X, $d = 2$) phases; for hard cubes ($D = 3$) Eq. (5.12) accounts for smectic (Sm, $d = 1$), columnar (Col, $d = 2$) and simple-cubic crystal (X, $d = 3$) ordering.

The numerical solution of Eq. (5.12) on a grid of points is expected to offer a better description of the single-particle density than the constrained minimization based on the Gaussian ansatz Eq. (5.10). We develop a Picard algorithm to solve Eq. (5.12), where all the convolutions involved in the FMT formalism are handled by means of Fast Fourier Transforms [129]. Moreover, the minimization with respect to the lattice spacing λ is performed using the Brent algorithm [130].

5.3 Parallel Hard Squares (D=2)

5.3.1 Preliminary considerations

When considering the high-density phase behavior, monodisperse squares (as well as cubes in $D = 3$ dimensions) possess a peculiar property. Unlike other regular polygons (e.g., pentagons, hexagons,..., and disks), squares do not have a well-defined "locked-in" configuration at close packing. In other words, besides the two-dimensional ordered square crystal (X), any other configuration with rows (or columns) shifted with respect to one another completely fills the plane. Therefore, also a smectic phase (Sm), characterized by positional ordering along one direction only, should in principle be considered as a candidate stable phase (see Fig. 5.1(a)). The higher degeneracy of Sm configurations with respect to X configurations suggests a higher entropy of the former with respect to the latter. However, in low-dimensional systems thermal fluctuations can play a relevant role in destroying long-range order, leading to so-called Landau-Peierls instabilities [131, 132]. In particular, for short-range interactions proper crystals do not exist in $D = 2$ dimensions, since positional ordering can in this case have at most quasi-long-range character

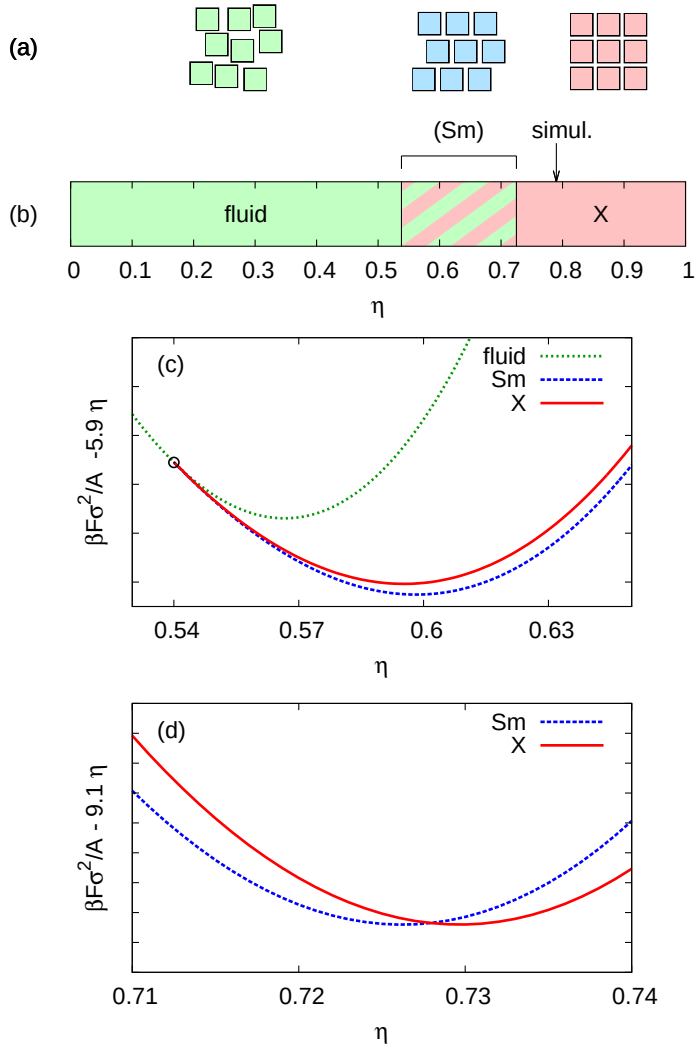

Figure 5.1: (a) Pictorial representation of (from left to right) the fluid, smectic (Sm) and square crystal (X) phases of parallel hard squares as a function of the packing fraction η. (b) Phase diagram of parallel hard squares according to FMT, to be compared with the simulation value of Ref. [105] for the fluid-to-crystal transition packing fraction (vertical arrow). The (Sm) interval highlights the states where the (Peierls-Landau unstable) smectic phase is predicted to be the stable phase. (c) FMT prediction for the free energy per unity area F/A of fluid (dotted green), Sm (dashed blue) and X (solid red lines) phases in the proximity of the second-order fluid-to-smectic (black circle) and (d) the first-order smectic-to-crystal transition.

[133]. The situation is even more dramatic when considering smectic phases, where thermal fluctuations make the correlation between layers decay exponentially with the distance [134]. This means that in $D = 2$ dimensions we do not expect smectic ordering to be stable at all. Computer simulations of both parallel [103] and freely-rotating [135] hard squares, where only a direct fluid-to-crystal phase transition was observed without any smectic state, confirm this picture.

5.3.2 Phase diagram

We report in Fig. 5.1(b) the phase diagram of parallel hard squares, as obtained by freely minimizing the FMT functional with respect to the single-particle density $\rho(\mathbf{r})$ including vacancies. Despite the above-mentioned considerations on the effect of fluctuations, we approximate the single-particle density of the X phase by assuming long-range order (as implied in Eqs. (5.10) and (5.12)). A similar approximation was recently applied for the description of the freezing transition in two-dimensional hard disks, showing remarkably good agreement with computer simulations [128]. We include in our calculations also the possibility of long-range Sm ordering, which is however expected to be Landau-Peierls unstable. The free-energy dependence of the fluid, smectic and crystal phases on the packing fraction η is reported in Fig. 5.1(c) and (d) for two density intervals. Note that this representation allows for common tangent constructions to identify coexisting states. Surprisingly, FMT predicts a second-order fluid-to-smectic transition at $\eta^* = 0.538$ (Fig. 5.1(c)) and a weakly first-order smectic-to-crystal transition with bulk coexisting densities $\eta_{Sm} = 0.726$ and $\eta_X = 0.730$ (Fig. 5.1(d)). The picture does not change appreciably by minimizing the free energy within the Gaussian ansatz, giving the sole effect of slightly displacing the alleged Sm-X transition ($\eta_{Sm} = 0.750$ and $\eta_X = 0.756$, not shown). As already pointed out, theoretical considerations and simulation results rule out the possibility of stable smectic ordering in the thermodynamic limit. Therefore, we must conclude that the smectic phase is an artifact due to the mean-field character of the fundamental measure theory, which is unable to take fully into account the role of long-wavelength fluctuations. On the other hand, the question whether the fluid or the crystal is the stable phase in the range of allegedly smectic stability (striped region in Fig. 5.1(b)) is open. We address this point, as well as possible conditions for smectic stability, in the final discussion of Sec. 5.5.

5.3.3 Crystal properties

In order to further investigate the properties of the crystal, we report the dependence of the vacancy concentration (Fig. 5.2(a)) and the root-mean-squared deviation from the average position in the unit cell, also known as Lindemann parameter (Fig. 5.2(b)), on the packing fraction. At the second-order transition at $\eta = 0.538$ the vacancy concentration is $x_{\text{vac}} \simeq 15\%$, and x_{vac} reduces monotonically with η. This value is appreciably higher than that predicted for hard disks $x_{\text{vac}} \simeq 2\%$ [128].

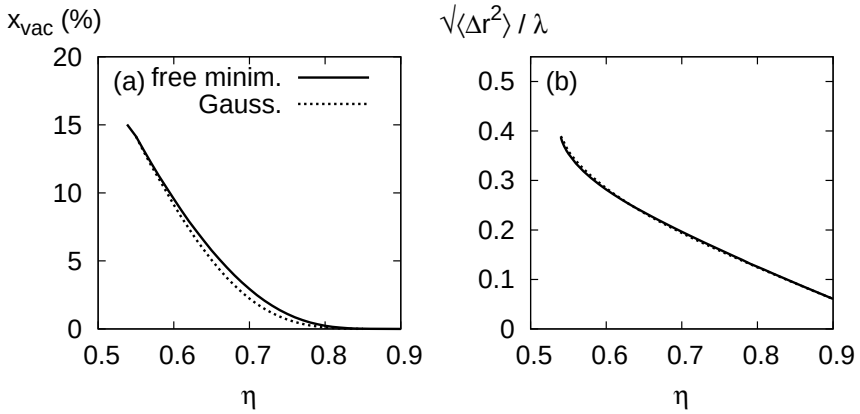

Figure 5.2: FMT results for (a) the vacancy concentration and (b) the root-mean-squared deviation from the average position (in units of the lattice constant λ) of the square crystal phase of parallel hard squares as a function of the packing fraction η. Solid lines correspond to values calculated by free minimization of the FMT functional, whereas dashed lines indicate those obtained through the Gaussian ansatz.

This marked difference between squares and disks shows analogies with the three-dimensional case. In fact, the vacancy concentration at the melting transition of hard cubes is two orders of magnitude higher than in hard-sphere systems [115, 120, 127]. Not unlike the case of hard cubes [115], these results suggest that vacancies can play an important role in stabilizing (quasi-long-range) crystal order in systems of hard squares. Moreover, Fig. 5.2(a) highlights a systematic, albeit small, underestimation of the vacancy concentration at intermediate packing fraction when the Gaussian ansatz is applied. On the other hand, no appreciable difference with the root-mean-squared deviation calculated by free minimization is observed in Fig. 5.2(b). In both cases, at the second-order transition the Lindemann parameter assumes a value close to 0.4. This value is remarkably higher than 0.15 which, according to the empirical Lindemann criterion, is related to the melting transition of a three-dimensional system [16]. Notice, however, that according to our calculation the Lindemann parameter takes the value of 0.15 at a packing fraction of $\eta = 0.75$ approximately. Therefore, the Lindemann criterion suggests in this case a melting transition at $\eta = 0.75$ approximately, which is very close to the simulation result for the fluid-to-crystal transition (see Fig. 5.1(b)).

We complete our analysis of the crystal phase by studying the evolution of the single-particle density from the freezing-transition region, where $\rho(x, y)$ is still appreciably non-zero at the edge of the Wigner-Seitz cell, to the confined regime at higher density. In Fig. 5.3(a), (c) and (e) we report the functional dependence of the equilibrium single-particle density inside the unit cell at packing fraction $\eta = 0.55$, 0.65 and 0.75, respectively. In order to ease the analysis, we plot on the

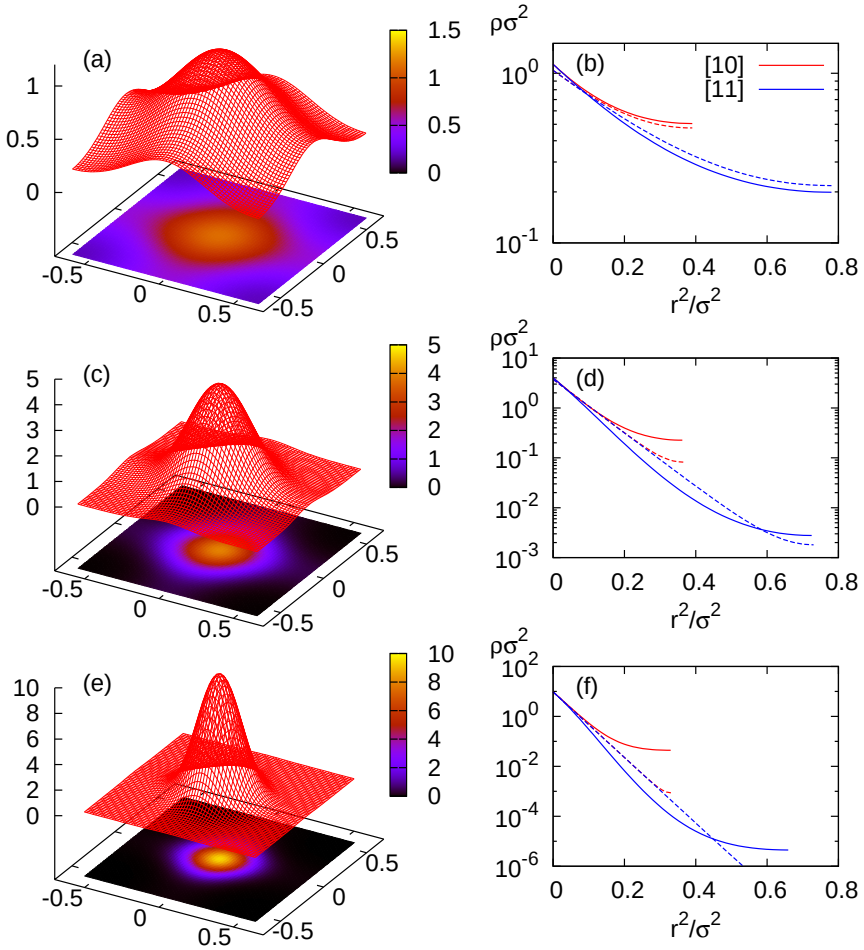

Figure 5.3: Single-particle density $\rho(x, y)$ in the unit cell of the square crystal phase obtained through FMT free minimization at packing fraction (a) $\eta = 0.55$, (c) $\eta = 0.65$ and (e) $\eta = 0.75$. On the right column we report the section of the single-particle density along the *[10]* (red lines) and *[11]* (blue lines) crystallographic directions. The graphs are expressed in log-scale as a function of the squared distance from the center of the unit cell. The dashed lines represent the corresponding functional dependence obtained through the Gaussian ansatz.

right of each figure (Fig. 5.3(b), (d) and (f)) a section of the corresponding $\rho(x, y)$ along the crystallographic directions *[10]* and *[11]*. These graphs are represented in logarithmic scale as a function of r^2 to highlight Gaussian behavior (straight lines). As expected, the section along the *[10]* direction, connecting nearest-neighbor sites, is systematically bigger than that along the *[11]* direction for both the freely minimized (solid lines) and Gaussian- parameterized (dashed lines) profiles. At the lowest packing fraction the peak of the density distribution is smeared out on the unit cell. As a consequence, the single-particle density in the Gaussian parameterization shows relevant deviations from a Gaussian distribution due to the overlap of the peaks centered on neighboring cells. In fact, the tails of the neighboring lattice sites allow to properly reproduce the anisotropy of the density peak. This leads to the marked difference between the *[10]* and *[11]* profiles, which is similar to what observed for the free-minimization solution (Fig. 5.3(b)). This overlap is weaker at higher packing fraction, where the confinement is stronger. Hence, the Gaussian ansatz fails to reproduce the anisotropy of the distribution in this regime (Fig. 5.3(d) and (f)). However, these deviations occur on a density scale a few orders of magnitude smaller than the peak value, and therefore their relevance is quantitatively limited.

5.4 Parallel Hard Cubes (D=3)

5.4.1 Phase diagram

Here we compare the predictions of the freely-minimized FMT for parallel hard cubes with those based on the Gaussian parameterization (a case extensively studied in the past [108, 112, 120]) with our results based on the free minimization of the functional. Since the formulation by Cuesta and Martínez-Ratón [111], FMT is known to correctly predict two significant properties of the freezing transition of the model [112]: (i) its second-order character and (ii) the role of vacancies in stabilizing the crystal.

The second-order fluid-to-crystal transition, which is known to become first-order when the rotational degrees of freedom are taken into account [107], is predicted to occur at packing fraction $\eta = 0.314$. As in the case of parallel squares, this value appreciably underestimates the simulation result of $\eta = 0.469$ [120] (see Fig. 5.4(a)). Also in analogy with parallel hard squares, parallel cubes lack a "locked-in" configuration at close packing. By means of a bifurcation analysis of the FMT functional and computer simulations, Groh and Mulder addressed the question about the stability of columnar order, and showed it to be metastable [108]. In contrast to hard squares, smectic and columnar solutions are in the three-dimensional case always metastable with respect to the crystal. This finding, which results directly from our free minimization scheme, is easily verified by comparing the free-energy curves of smectic, columnar and crystal phases as a function of the packing fraction in Fig. 5.4(b).

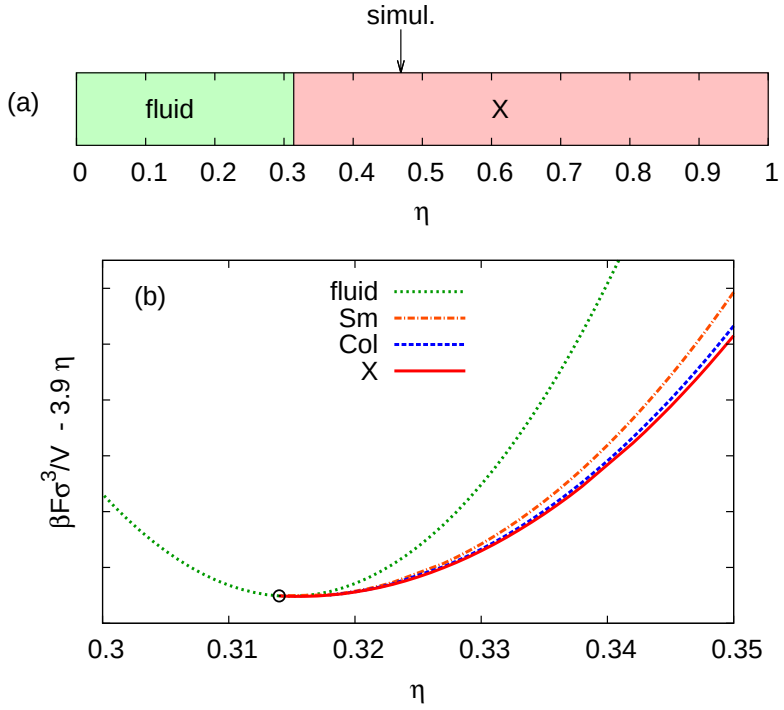

Figure 5.4: (a) Phase diagram of parallel hard cubes according to FMT as a function of the packing fraction η, to be compared with the simulation result of Ref. [120] for the fluid-to-crystal (X) transition packing fraction (vertical arrow). (b) FMT prediction for the free energy per unit volume $\beta F/V$ of fluid (dotted green), crystal (solid red) and the metastable columnar (Col, dashed blue) and smectic (Sm, dot-dashed orange) phases in the proximity of the second-order freezing transition (black circle).

5.4.2 Crystal properties

The remarkably high concentration of vacancies at the freezing transition, $x_{\text{vac}} \simeq 30\%$, is a known feature of the theory (cf. Fig. 5.5(a)) [108, 112]. Although this value is three orders of magnitude higher than that measured for hard spheres [127], it was recently shown to be compatible with computer simulations of both parallel ($x_{\text{vac}} = 13\%$ [120]) and freely-rotating ($x_{\text{vac}} = 6.4\%$ [115]) hard cubes, thus highlighting the essential role of vacancies in stabilizing the simple-cubic crystal. Within the free minimization of the FMT functional, the vacancy concentration at bulk coexistence does not change with respect to the Gaussian ansatz result. Nonetheless, an inspection of Fig. 5.5(a), reporting x_{vac} as a function of the packing fraction η, shows that the Gaussian ansatz tends to underestimate this property at intermedi-

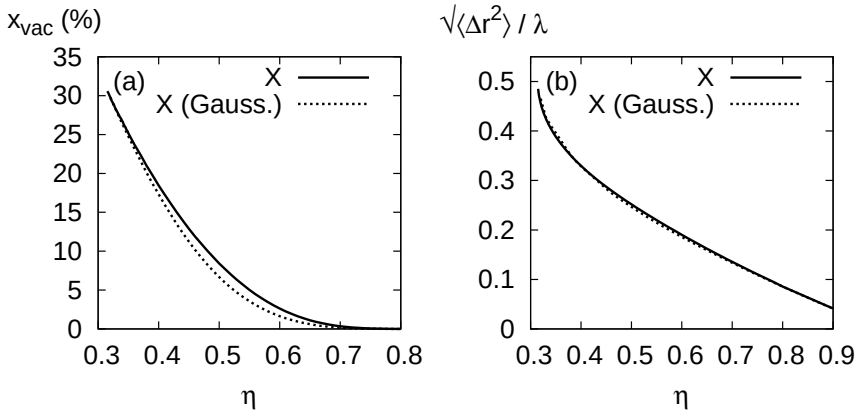

Figure 5.5: FMT results for (a) the vacancy concentration and (b) the root-mean-squared deviation from the average position (in units of the lattice constant λ) of the simple-cubic crystal phase of parallel hard cubes as a function of the packing fraction η. Solid lines correspond to values calculated by free minimization of the FMT functional, whereas dashed lines indicate those obtained through the Gaussian ansatz.

ate packing fractions. Therefore, in this regime the free minimization improves the Gaussian ansatz data by furnishing results closer to those of computer simulation [120]. However, if we focus on the root-mean-squared deviation from the average lattice site (Lindemann parameter), reported as a function of the packing fraction η in Fig. 5.5(b), we do not observe any appreciable deviation from the known dependence calculated by means of the Gaussian ansatz. Notice that the Lindemann parameter takes a value close to 0.5 at the fluid-to-crystal transition. We conclude that, similarly to the case of hard squares, the Lindemann prediction of a root-mean-squared deviation close to 0.15 at the melting transition grossly fails. For hard squares we have seen that the packing fraction at which the Lindemann parameter takes the value of 0.15 is actually pretty close to the expected freezing transition. This is not the case for hard cubes, where the melting transition deduced via the Lindemann criterion takes the value of approximately $\eta = 0.65$, which appreciably overestimates the simulation prediction of $\eta = 0.469$ [120].

Finally, in Fig. 5.6 we represent sections of the equilibrium single-particle density $\rho(x, y, z)$ at packing fraction $\eta = 0.32$ ((a)-(b)), 0.50 ((c)-(d)) and 0.70 ((e)-(f)) and we compare them with the corresponding Gaussian ansatz solution (dashed lines). The graphs on the left ((a), (c) and (e)) show sections along the crystallographic directions *[100]* (red lines), *[110]* (green lines) and *[111]* (blue lines); to ease the comparison, we report on the right of each graph ((b), (d) and (f)) the absolute difference of these sections between the two minimization methods. In the three cases, the cubic symmetry of the freely-minimized solution is evident by the hierarchy in values of the single-particle density along the three crystallographic directions. In

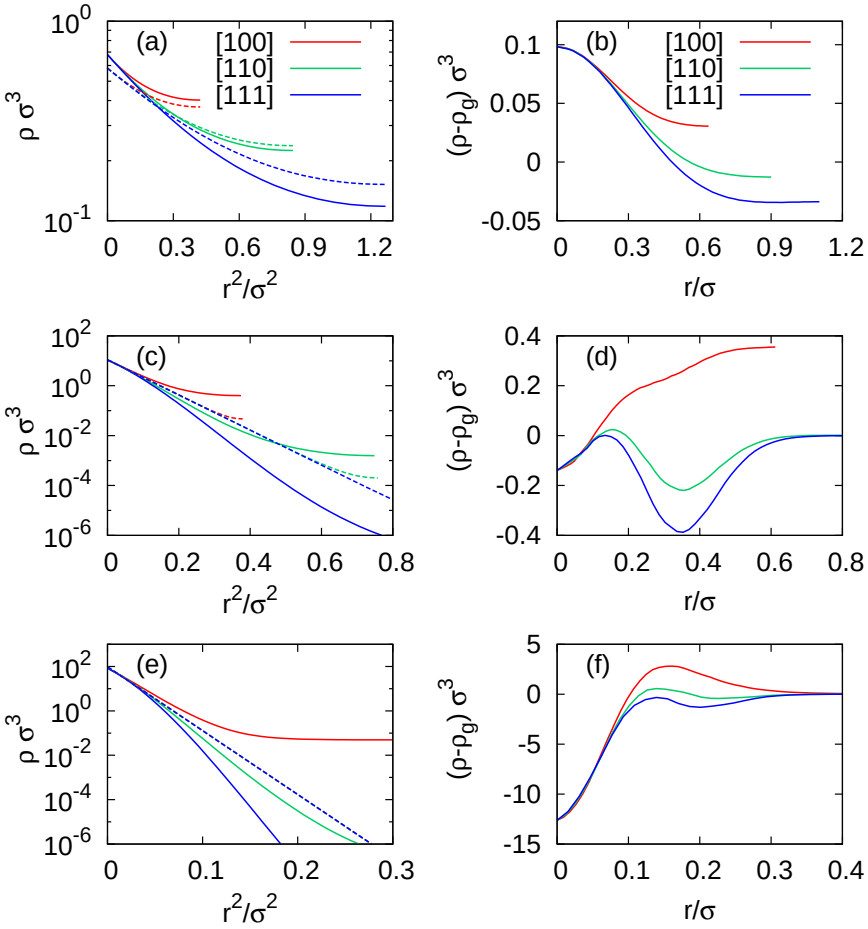

Figure 5.6: FMT prediction for the single-particle density of parallel hard cubes. The graphs on the left show sections of $\rho(x,y,z)$ along the crystallographic directions *[100]* (red lines), *[110]* (green lines) and *[111]* (blue lines) at packing fraction (a) $\eta = 0.32$, (c) 0.50 and (e) 0.70 calculated by means of free minimization of the functional (solid lines) and the Gaussian ansatz (dashed lines). The right graphs represent the corresponding absolute difference between the free minimization solution and the Gaussian ansatz for the three packing fractions ((b)$\eta = 0.32$, (d) 0.50 and (f) 0.70) and the three crystallographic directions considered.

analogy with the parallel square system, at low enough packing fraction there is good quantitative agreement between the two methods, since the overlap between neighboring peaks within the Gaussian ansatz allows to reproduce the anisotropy of the single-particle distribution. At higher packing fraction, deviations from the Gaussian-ansatz solution are evident, but limited to the low-density region of the unit cell.

5.5 Discussion and Conclusions

By means of the fundamental measure theory we investigate the phase behavior of single-component systems of parallel hard squares (in $D = 2$ dimensions) and cubes ($D = 3$). Our attention focuses on the predictions for the freezing transition and the properties of the crystal phase. In density-functional theory the typical approach for describing crystal phases is based on the parameterization of the single-particle density by a sum of Gaussian functions centered on the lattice sites. We compare these predictions with a more accurate free-minimization method, where the single-particle density is evaluated on a grid of points.

Despite its simplicity, we conclude that for both squares and cubes the Gaussian parameterization works remarkably well. Apart from some inadequacy of the Gaussian ansatz in describing the anisotropy of the single-particle density of the crystal, the main deviations between the two minimization methods lie in the expected vacancy concentrations of the square and simple-cubic crystals, which appears to be slightly underestimated by the Gaussian ansatz. On the other hand, as already noticed for cubes, FMT suffers from a serious inability to give quantitatively reliable values for the freezing packing fraction. However, improvement in this direction can be achieved only by a reformulation of the theory itself, as the numerical minimization is performed exactly. The development of FMT for hard spheres from the original version by Rosenfeld suggests that fruitful approaches could involve the addition of new (tensorial) weight functions [136] or the use of an equation of state as an input of the theory in order to improve over the Scaled Particle Theory approximation [124, 137].

For the three-dimensional system of parallel hard cubes our results coincide with previous FMT analysis based on the Gaussian parameterization and indicate a second-order fluid-to-crystal transition with a vacancy-rich crystal phase. For the parallel hard-square system, this work constitutes to the best of our knowledge the first analysis based on density-functional theory. In contrast with previous simulation studies, the fundamental measure theory predicts a stable smectic phase in between the low-density fluid and the high-density square crystal. However, by taking into account the effect of long-wavelength thermal fluctuations, one can show the one-dimensional smectic ordering to be unstable. Therefore, we deduce that the mean-field character of the theory, which is unable to properly take into account the role of fluctuations, is the element to be blamed for this artifact. When big enough simulation boxes are considered, computer simulations with periodic bound-

ary conditions confirm the picture of an unstable smectic phase [135]. However, it is interesting to notice that, when the simulation box is small enough, ordering of the squares in parallel layers was observed [135]. On the basis of these observations, it is tempting to conclude that, when long-wavelength fluctuations can be neglected, the behavior of the system coincides with the predictions of FMT, showing a stable smectic phase. In other words, we expect parallel-square systems to develop intermediate smectic states in finite size systems and under the effect of confining walls.

For what concerns the original problem regarding the phase behavior of parallel hard squares in the thermodynamic limit, the conclusions we can draw are more limited. On the basis of our theoretical results we do not have enough elements to deduce which of the two phases, either the fluid or the crystal, is the stable one in the density range where the theory predicts a stable smectic. In fact, if we simply neglected the smectic solution of FMT, we would find a second-order freezing transition at $\eta^* = 0.538$; on the other hand, if we kept the smectic solution while deducing it to be structurally indistinguishable from the fluid due to the fluctuations-induced short-range correlations between smectic layers, we would obtain a first-order freezing transition with coexisting densities $\eta_{fluid} = 0.726$ and $\eta_X = 0.730$. Since we do not have any prescription to choose between these two alternative scenarios, we cannot conclude whether the theory predicts a low-density second-order freezing transition with a high vacancy concentration in the crystal, or a higher-density weakly first-order freezing with a lower vacancy concentration.

Although FMT is well-known to incorporate short-range correlations accurately, this study brings to the front a shortcoming of FMT as regards the incorporation of long-wavelength fluctuations. We hope that this study stimulates new developments in this direction, perhaps along (some of) the lines of Hierarchical Reference Theory [138] to reconcile short- and long-range correlations consistently.

Acknowledgements

It is a pleasure to thank R. Evans, F. Smallenburg and M. Marechal for stimulating discussions.

Chapter 6

Heterogeneous diffusion in columnar liquid crystals

Abstract

In the wake of previous studies on the rattling-and-jumping diffusion in smectic liquid-crystal phases of colloidal rods, we analyze here the heterogeneous diffusion in columnar phases. More specifically, we perform computer simulations aimed at investigating the relaxation dynamics of a binary mixture of perfectly aligned hard spherocylinders. We find that the columnar arrangement of the system produces free-energy barriers the particles need to overcome in order to jump from one column to another. This determines a hopping-type diffusion in the plane perpendicular to the nematic director. Such a phenomenon accounts for the non-Gaussian inter-column diffusion and manifests itself in a two-step structural relaxation, which is remarkably analogous to that of out-of-equilibrium glass-forming systems and gels. Slight deviations from the behavior of simple liquids due to packing effects are also observed along the nematic director.

6.1 Introduction

Liquid crystals are phases of matter characterized by a partial spontaneous breaking of the spatial symmetries of the system due to anisotropies in the interparticle interactions. Since the spontaneous symmetry breaking involves only some of the spatial symmetries of the Hamiltonian, liquid crystals manifest features in between the crystalline solid and the isotropic liquid phase. The notion that entropic effects alone are sufficient to drive the self-assembly of liquid-crystal phases is well established in colloid science, where in many situations the main interactions between the particles have a purely repulsive, steric origin [24, 139–142]. Due to their simplicity, model systems of hard particles constitute the natural choice to describe the phase and aggregation behavior of this type of colloidal suspensions.

In his seminal work Onsager showed that a system of purely repulsive infinitely thin rigid cylinders undergoes an isotropic-nematic phase transition associated with

the development of spontaneous orientational order [24]. The more realistic case of rods with finite size has been extensively studied in the past thanks to computer simulation. It has been shown that, by varying their length-to-diameter ratio, one- (smectic), two- (columnar) and three- (crystal) dimensional translational ordered phases could be encountered [143, 144]. However, further studies showed that in monodisperse systems of both parallel [145] and freely rotating [84] hard rods the columnar phase happens to be metastable with respect to the smectic for each value of the length-to-diameter ratio. The complexity of the phase behavior of linear particles becomes even more pronounced by proceeding from monodisperse systems to mixtures [70, 146–149]. Size-polydispersity introduces a sensible change in the phase behavior of rod-like particles, as their packing happens to be not as effective as in systems of monodisperse rods. For instance, the formation of smectic layers in a system of hard spherocylinders can be inhibited by introducing a length bidispersity. As a result, a columnar liquid-crystal phase substitutes the smectic in the phase diagram [146, 147]. Entropy-driven columnar phase transitions have also been observed in monodisperse systems of disc-like particles, such as cut spheres and oblate spherocylinders [67, 150–152]. As far as rod-like particles are concerned, theoretical studies indicated that the columnar order could be observed not only in bidisperse mixtures, but also in more realistic polydisperse systems of parallel cylinders [153]. However, polydispersity is not the only element which favors the stabilization of the columnar phase in systems of rods, as it was recently suggested that the columnar stability can be enhanced by means of soft repulsions [154]. On the other hand, the effect of rod flexibility in stabilizing the columnar phase is at present still under debate [155–158].

As a consequence of our increased understanding of the static (i.e., equilibrium time-independent) properties of colloidal liquid crystals, a stronger interest towards the dynamic time-dependent ones has been manifested. Most of the work in this direction focused on the single-particle diffusion, which in the presence of nematic ordering develops anisotropies quantifiable through the measure of the self-diffusion coefficients [159–162]. Experimentally such measurements have been successfully performed by means of fluorescence techniques [163–166]. However, in these experiments the particles were sampled collectively, and only little work focused on the dynamics at the single-particle level [167, 168]. By applying fluorescence microscopy to the study of the single-particle dynamics of *fd* viruses in suspension, Lettinga and Grelet observed for the first time the mechanism of interlayer diffusion (a.k.a., permeation) in smectic liquid crystals [168]. More specifically, they showed that the layered structure characteristic of the smectic phase induces a heterogeneous diffusion in the direction perpendicular to the layers. This heterogeneous dynamics accounts for deviations from Gaussian diffusion, a feature which is well known to characterize non-equilibrium homogeneous states of spherical particles close to a kinetic-arrest transition [169–172]. The diffusion is termed heterogeneous since one can identify different time regimes characterized by different diffusion coefficients. At small time scales each particle does not feel the presence of its neighbors, and the diffusion coefficients are determined by the particle's geometry and by the solvent's

viscous properties only (free diffusion). On the other hand, at higher time scales the diffusion is hampered by the ordered structure of the fluid, which allows for the diffusion through smectic layers via quasi-quantized jumps . This picture allows to interpret the dynamics in the system at time t by the identification of "slow" and "fast" particles: slow particles are those which have not left their smectic layer after an interval of time t, whereas fast ones are those which succeeded in it. The discrete nature of the diffusion through the smectic layers has been interpreted in terms of effective permanent free-energy potentials related to the periodic structure of the phase. However, in a recent dynamic density-functional theory study Bier *et al.* highlighted the role on the dynamics of the in-layer structure, which cannot be accounted for in models based on the permanent free-energy background only [173, 174]. This work showed that the in-layer fluid-like structure determines a "temporary" caging regime that sums up to the "permanent" one induced by the smectic ordering [173, 174]. Such a coupling between in-layer and intra-layer diffusion has been confirmed by simulations of both parallel [175] and freely rotating [176, 177] hard spherocylinders. Moreover, these simulation approaches allowed for a quantitative analysis of the structural relaxation in terms of the deviation of the time correlations from the exponential decay typical of simple fluids [175–177].

Following this line of research and motivated by a recent experiment on a colloidal suspension of *fd* viruses [178], we investigate in this chapter the dynamics of a binary mixture of rod-like particles exhibiting a stable columnar liquid-crystal phase. Using Monte Carlo (MC) simulations we are able to study for the first time the dynamical heterogeneities arising from the columnar structure and their effect on the diffusion and on the long-time structural relaxation of the system. The reliability of such a Monte Carlo based approach to the study of the dynamics of inhomogeneous liquid crystals has been confirmed to be excellent when compared to more realistic but time-consuming Brownian Dynamics simulations [179]. Furthermore, we measure the inter-column free-energy barriers and compare our results with the simulation data available for the smectic phase [175–177].

6.2 Model and Simulations

We study a system containing $N = 1600$ perfectly aligned hard spherocylinders with aspect ratio $L^* = L/D$. L and D are the length and diameter of a cylindrical body capped by two hemispheres with diameter D, respectively. The phase diagram of a monodisperse system containing such rod-like particles shows stable nematic, smectic, and crystal phases, but lacks a stable columnar phase in the range $0 \leq L^* < \infty$ [145]. Stroobants studied the phase behavior of bidisperse systems of hard rods and found that the bidispersity can favor and stabilize columnar order over smectic order [146]. Therefore, in order to prevent the formation of smectic layers, we investigate a binary mixture of hard spherocylinders with the same diameter D (used as our unit of length), but different lengths L_1^* and L_2^*, with $L_1^* > L_2^*$. In this model, the rotational degrees of freedom are frozen out and hence the particles are

forced to be aligned along a common nematic director, oriented along the z axis. The relative concentration of the two species is chosen such that the volume fractions of each component are the same. The phase diagram at fixed $L_2^* = 1.0$ displays a region of stability of the columnar phase which increases with L_1^* and disappears at $L_1^* \leq 1.6$, where a nematic-smectic transition is observed [146]. Here we study a columnar ordered binary mixture of rods with $L_1^* = 2.1$ and $L_2^* = 1.0$, and relative concentrations $x_1 = N_1/N = 0.375$ and $x_2 = N_2/N = 0.625$, respectively. At lower pressure the columnar phase undergoes a transition into a nematic phase, while at higher pressure it freezes into a solid crystal.

We perform standard MC simulations in a rectangular box of volume V with periodic boundary conditions. In order to equilibrate the columnar phase, we carry out preliminary equilibration runs in the isobaric-isothermal (NPT) ensemble. The particle moves are accepted according to the Metropolis algorithm [31], that is, if no particle overlap is detected (see Sec. 2.4). Each MC cycle consists of N attempts to displace a randomly selected particle, plus an attempt to modify the box volume with independent changes of the three box sides. The system is considered to be in equilibrium when the volume reaches a stationary value within the statistical fluctuations. We run simulations at several reduced osmotic pressures $P^* = \beta P D^3$, where $\beta = 1/k_B T$, k_B is the Boltzmann's constant and T the absolute temperature. In particular, we equilibrate a nematic phase at $P^* = 2.5$ (packing fraction $\eta = N(x_1 v_1 + x_2 v_2)/V = 0.470$ with v_i ($i = 1, 2$) the single particle volume) which is very close to the nematic-columnar transition, and three different columnar phases at $P^* = 3.0$ ($\eta = 0.535$), 3.5 ($\eta = 0.563$) and 4.0 ($\eta = 0.580$). In all these cases, our starting configuration consists of a highly packed columnar structure with the rods randomly located along the z direction, and hexagonally ordered in the xy plane. The minimum number of MC cycles needed for an equilibration run is roughly 5×10^5, and is followed by a production run of 2×10^6 MC cycles in the canonical (NVT) ensemble to simulate the relaxation dynamics and evaluate all the physical properties of interest. In this case, the box volume is kept fixed in order to prevent unphysical collective moves which do not mimic the Brownian dynamics of the particles. In the following the role of hydrodynamics and hydrodynamic interaction, which is extremely difficult to explicitly take into account, is completely neglected. In rod suspensions this choice is justified in a first approximation, since the main contribution to the dynamics comes from the excluded-volume interactions [180].

Under these conditions, the MC approach offers a useful and effective tool to study the dynamics of colloids. In fact, in spite of its intrinsically non-dynamical nature, MC algorithms are able to reproduce the Brownian diffusion typical of colloidal suspensions [181]. To pursue this goal, one must set a small enough maximum MC displacement, typically of the order of one tenth of the shortest dimension of the particle. The optimal value of the mean particle displacement is strictly linked to the acceptance rate and hence to the CPU time per simulation run. The maximum displacement is fixed to give an acceptance rate of roughly 50% per move. Furthermore, in order to take into account the non-spherical shape of the particles,

the maximum MC displacement is set in such a way that at short times it reproduces the anisotropic diffusion of a single colloidal rod. More specifically, the ratio between the maximum MC displacement in the xy plane $\Delta x_{max} = \Delta y_{max}$ and in the z direction Δz_{max} is set as

$$\frac{\Delta x_{max}}{\Delta z_{max}} = \frac{\Delta y_{max}}{\Delta z_{max}} = \sqrt{\frac{D_\perp}{D_\parallel}}, \tag{6.1}$$

where we denote with $D_\perp$ and $D_\parallel$ the short-time self-diffusion coefficients of the rod in the direction parallel and perpendicular to its long axis, respectively. In order to estimate the ratio $D_\perp/D_\parallel$, which solely depends on the geometry of the particle, we refer to the semi-empirical expression derived in Ref. [182]. In that work, the authors used a numerical approach to evaluate the translational self-diffusion coefficients of a cylindrical particle for different values of the length-to-diameter ratio p, finding good overall agreement with experimental data in the range $2 < p < 30$ [183]. A least-square quadratic fitting in p^{-1} of the data allowed the authors to give an analytic expression for the transverse and longitudinal self-diffusion coefficients as functions of the parameter p. Since here we consider spherocylinders, we evaluate the ratio $D_\perp/D_\parallel$ by setting $p = (L+D)/D$, while neglecting deviations due to the non-cylindrical shape of the particles. According to the above-mentioned expression, the ratio between the maximum MC displacement perpendicular and parallel to the z axis is set to 0.92 for particles of species 1 and 0.94 for those of species 2. Moreover, since the transverse section of the particles is the same for the two species, we set the longitudinal maximum MC displacement along the z axis to be the same for the two components. Once the short-time longitudinal ($D_\parallel$) and transverse ($D_\perp$) self-diffusion coefficients are known, it is possible to introduce a time scale defined by $\tau = D^2/D_{tr}$. The total translational diffusion coefficient $D_{tr} = (\langle D_\parallel \rangle + 2\langle D_\perp \rangle)/3$ is evaluated in terms of the measured longitudinal and transverse short-time diffusion coefficients averaged over the two species [175].

6.3 Relevant physical properties

In order to analyze the heterogeneous diffusion and the structural relaxation of the system, the following physical properties are calculated.

Transverse mean-field potential

In a columnar liquid-crystal phase the translational invariance is spontaneously broken in the plane (xy) perpendicular to the nematic director (z). This gives rise to a non homogeneous probability $\pi_i(x, y)$ of finding a particle of species $i = 1, 2$ at the position (x, y, z). The effective energetic barrier associated with this probability distribution is given by the mean-field potential $U_i(x, y)$, defined as [168]

$$\pi_i(x,y) \propto \exp\left[-\frac{U_i(x,y)}{k_B T}\right], \tag{6.2}$$

where the zero of the potential is set at its periodic minima.

Self part of the van Hove function (SVHF)

The heterogeneous dynamics and hopping-type inter-column diffusion can be quantitatively described by means of the self-part of the van Hove function (SVHF) [184]

$$G_s(\mathbf{r},t) = \left\langle \frac{1}{N}\sum_{j=1}^{N} \delta(\mathbf{r} - \mathbf{r}_j(t+t_0) + \mathbf{r}_j(t_0)) \right\rangle, \tag{6.3}$$

which measures the probability distribution for a particle displacement $\mathbf{r}$ in a time interval t. Since in this chapter our attention focuses on the columnar phase, it is natural to separately study the diffusion in the xy plane, where the system is inhomogeneous, and along the z axis, where the same is homogeneous. This separate analysis is achieved by partially integrating the SVHF Eq. (6.3) in the x and y coordinates to get the longitudinal component

$$G_s^{\parallel}(z,t) = \left\langle \frac{1}{N}\sum_{j=1}^{N} \delta(z - z_j(t+t_0) + z_j(t_0)) \right\rangle, \tag{6.4}$$

and in the z coordinate to get its transverse component. The transverse component of the SVHF can be further averaged over the azimuthal angle of $\mathbf{r}$

$$G_s^{\perp}(R,t) = \left\langle \frac{1}{N}\sum_{j=1}^{N} \delta(\mathbf{R} - \mathbf{R}_j(t+t_0) + \mathbf{R}_j(t_0)) \right\rangle_{2\pi}. \tag{6.5}$$

In the above equations $(\mathbf{R}_j(t), z_j(t))$ is the position of particle j at time t, δ is the Dirac delta; $\langle \ldots \rangle$ stands for an ensemble average, and the index 2π indicates an additional average over the azimuthal angle θ associated with the bidimensional vector $\mathbf{R} = (x,y) = (R\cos(\theta), R\sin(\theta))$. In the case of free diffusion, i.e., for non-interacting particles, these functions are described by Gaussian distributions [3].

Distinct part of the van Hove function (DVHF)

The SVHF introduced in the previous section contains all the relevant information about the single-particle diffusion. However, in order to fully understand the equilibrium dynamics of a many-particle system, one needs to take into account also the collective dynamics of two or more particles. Such a task is achieved by calculating the distinct-part of the van Hove function (DVHF). The DVHF is the probability distribution that a particle occupies the position $\mathbf{r}$ at the instant $t_0 + t$, when another particle is at the origin at t_0. The DVHF is defined as

$$G_d(\mathbf{r},t) = \left\langle \frac{1}{N}\sum_{j\neq i=1}^{N} \delta(\mathbf{r} - \mathbf{r}_j(t+t_0) + \mathbf{r}_i(t_0)) \right\rangle . \tag{6.6}$$

Similarly to our analysis for the SVHF, we are interested in investigating separately the diffusion dynamics along the nematic director (z) and in the plane of the columnar ordering (xy). Therefore, we consider the longitudinal

$$G_d^{\parallel}(z,t) = \left(\frac{\pi D^2}{4}\right)^{-1} \int_0^{D/2} RdR \int_0^{2\pi} d\theta G_d(\mathbf{r},t), \tag{6.7}$$

and the transverse component of the DVHF

$$G_d^{\perp}(R,t) = (2\pi L)^{-1} \int_{-L/2}^{L/2} dz \int_0^{2\pi} d\theta G_d(\mathbf{r},t), \tag{6.8}$$

where we set $L = \min\{L_1, L_2\}$ and θ is the azimuthal angle of $\mathbf{r}$ in the xy plane.

Non-Gaussian parameter (NGP)

In the case of freely-diffusing colloidal particles, the mean square displacement depends linearly on time and the SVHF is a Gaussian distribution [3]. However, in the case of an interacting many-particle system one expects deviations from this type of Gaussian diffusion. Such deviations can be estimated through the non-Gaussian parameter (NGP), defined as [185]

$$\alpha_2(t) = \frac{\langle \Delta\mathbf{r}^4(t)\rangle}{(1+2/d)\langle \Delta\mathbf{r}^2(t)\rangle^2} - 1, \tag{6.9}$$

where $\Delta\mathbf{r}(t)$ is the displacement of a particle during a time interval t. The parameter d refers to the dimension of the space over which the diffusion is considered. This means that $d = 1$ for the linear diffusion longitudinal to the nematic director ($\alpha_{2,z}(t)$), whereas $d = 2$ for the transverse diffusion in the xy plane ($\alpha_{2,xy}(t)$). As pointed out in Ref. [186], when dealing with mixtures one should pay attention not to take into account trivial non-Gaussianity related to a size-dependent particle mobility. In order to avoid this artifact, one has to calculate the NGP $\alpha_2^{(i)}$ as defined in Eq. (6.9) for each species $i = 1,2$ separately, and only afterwards perform an average weighted over the concentrations x_i, that is

$$\langle \alpha_2(t)\rangle = x_1\alpha_2^{(1)}(t) + x_2\alpha_2^{(2)}(t). \tag{6.10}$$

With these definitions heterogeneous diffusion can be detected when the NGP deviates from zero value.

Self part of the intermediate scattering function (SISF)

The structural relaxation of the system is conveniently described by means of the self-part of the intermediate scattering function (SISF)

$$F_s(\mathbf{k},t) = \left\langle \frac{1}{N}\sum_{j=1}^{N} \exp[i\mathbf{k}\cdot(\mathbf{r}_j(t+t_0)-\mathbf{r}_j(t_0))] \right\rangle , \tag{6.11}$$

which describes the decay of density auto-correlations in reciprocal space. Most of the relevant structural information is contained at the first peak $\mathbf{k}^*$ of the structure factor. Therefore, we can focus on the transverse and longitudinal relaxations by evaluating the SISF at the wave vectors $(k_x^*, k_y^*, 0)$ and $(0, 0, k_z^*)$, respectively. With this in mind, our analysis on the structural relaxation of the system involves the measurement of the functions $F_{s,xy}(t) \equiv F_s((k_x^*, k_y^*, 0), t)$ and $F_{s,z}(t) \equiv F_s((0, 0, k_z^*), t)$.

6.4 Hopping-type diffusion

When the difference in length between the two components of a binary mixture of aligned hard spherocylinders is sufficiently high, the system undergoes a transition from a nematic to a columnar phase. The structure of the columnar phase is characterized by the development of hexagonal order in the plane perpendicular to the nematic director [146]. Two typical configurations in the nematic ($P^* = 2.5$) and in the columnar phase ($P^* = 4.0$) are depicted in Fig. 6.1.

The effect of the columnar structure on the single-particle motion can be observed in Fig. 6.2, where we show typical trajectories of long and short rods projected on the xy plane at $P^* = 3.0$. The difference with the Gaussian diffusion typical of a simple liquid, where the particle trajectories resemble the behavior of a random walker, is evident. In this case, the dynamics is characterized by a hopping-type diffusion: each particle rattles around the center of a column until it finds suitable conditions to jump to another column. The spread in the total displacement between long and short rods, reported in Fig. 6.2(a) and (b), respectively, is linked to the different free-energy barriers felt by the two components, as discussed in what follows. Such a behavior is observed in the whole range of osmotic pressure considered, and its effects on the long-time relaxation dynamics of the system are crucial. More specifically, the long rods are expected to sample the configuration space on a time scale significantly longer than that associated with the short ones. As a consequence, the decay of the correlation functions is strongly affected by the slow diffusion of the long particles, as we will show in Sec. 6.7.

The single-particle diffusion in a system characterized by spontaneous translational-symmetry breaking is conveniently described as the motion of an isolated particle subject to an effective one-body potential. For the columnar ordering object of this study, the effective one-body potential $U(x, y)$ is given in Eq. (6.2). This approach was applied in experiments [168] and simulations [175–177] to characterize

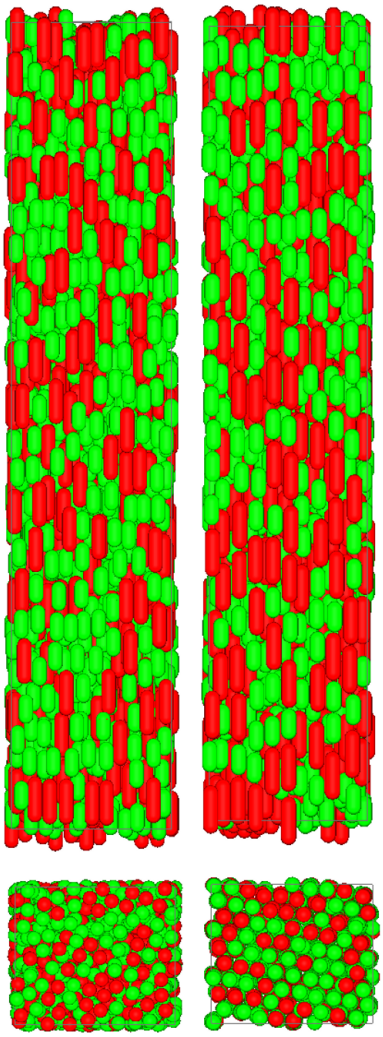

Figure 6.1: Side and top views of two typical configurations in the nematic ($P^* = 2.5$, left figure) and in the columnar phase ($P^* = 4.0$, right figure) of a binary mixture of perfectly aligned hard spherocylinders with length-to-diameter ratios $L_1^* = 2.1$ (in red) and $L_2^* = 1.0$ (in green) and relative concentrations $x_1 = 0.375$ and $x_2 = 0.625$.

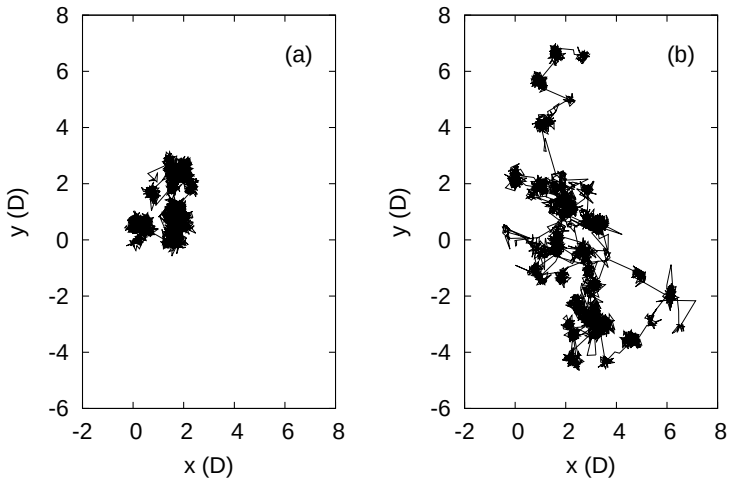

Figure 6.2: Two typical trajectories projected on the xy plane of a long (a) and a short (b) rod in the columnar phase at reduced pressure $P^* = 3.0$ after an interval of time $\Delta t = 380\tau$.

the hopping-type diffusion in smectic liquid crystals along the nematic director. It was found that the free-energy cost for the layer-to-layer diffusion is of the order of few k_BT per particle, depending mostly on the packing of the system, but also on the degree of anisotropy of the rods and the presence of rotational degrees of freedom. For binary mixtures one has to evaluate separately the mean-field potential related to each component. We report in Fig. 6.3 the mean-field potential for long and short rods at several values of the osmotic pressure. The minima of the potential correspond to the hexagonal lattice positions, while the height of the barriers gives a quantitative description of the free-energy penalty associated with a column-to-column jump. In order to better estimate the height of the maxima of the potential, we report in Fig. 6.4 a transverse section of the energy landscapes of Fig. 6.3. Following the procedure of Ref. [175], the experimental points in Fig. 6.4 are fitted with a function

$$U(R) = \sum_{k=1}^{n} U_k \left[\sin\left(\frac{\pi R}{h} \right) \right]^{2k}, \tag{6.12}$$

with U_k and h fit parameters and $n = 5$. As expected, the height of the potential barrier increases with the packing fraction and with the particle anisotropy [176]. At sufficiently high packing fractions, we detect higher barriers for the longer rods. Additionally, at the reduced osmotic pressure $P^* = 3.5$ and 4.0 the column-to-column jumps become so rare that the associated statistics is too poor to furnish a precise estimate of the barrier height. In other words, the long rods are constrained to rattle

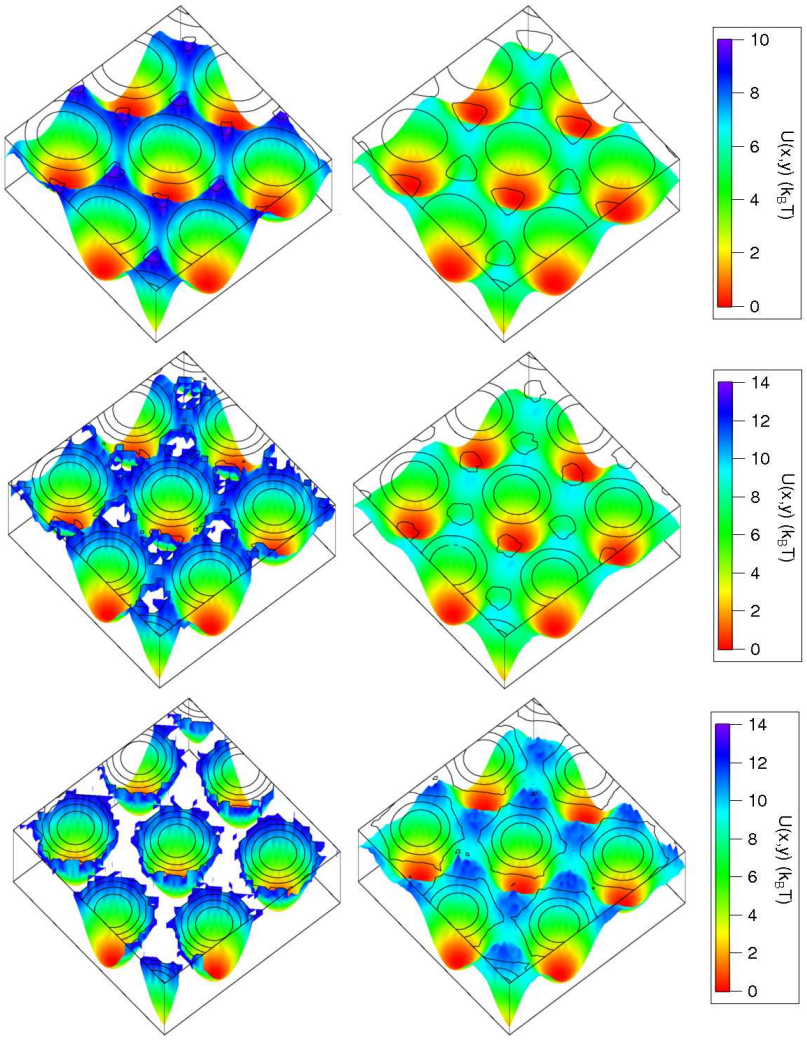

Figure 6.3: Mean-field effective potential $U(x, y)$ in units of k_BT in the bulk columnar phase of a binary mixture of perfectly aligned hard spherocylinders at $P^* = 3.0$, $P^* = 3.5$ and $P^* = 4.0$ (from top to bottom). The images on the left correspond to the long rods (species 1), whereas those on the right to the short ones (species 2). In order to ease the visualization, the black lines at the top of each graph identify the isopotential points in the xy plane with increments of $3k_BT$.

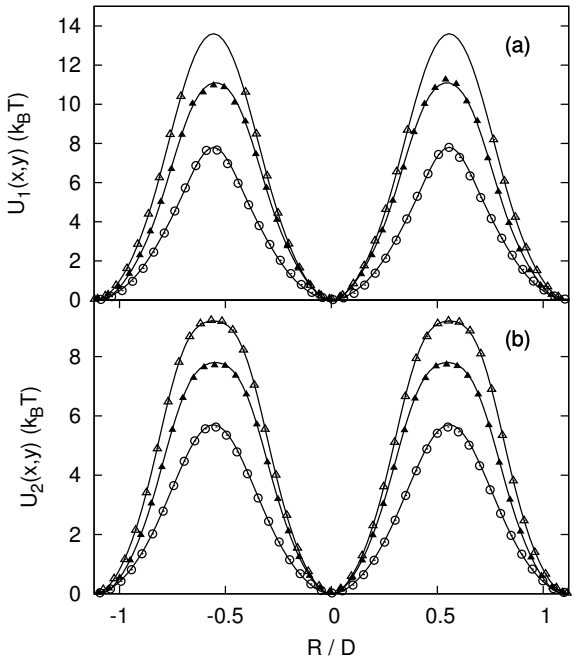

Figure 6.4: Transverse section of the mean-field effective potential in Fig. 6.3 for a binary mixture of long (a) and short (b) hard spherocylinders at the reduced osmotic pressure $P^* = 3.0$ (○), $P^* = 3.5$ (▲) and $P^* = 4.0$ (△). The solid lines are fits (see text).

in their columnar "cage", the jump to a neighboring column being too demanding. This is due to the fact that at high packing fraction no MC configuration shows a long rod in between two columns, with the result that the mean-field potential is characterized by an unphysical divergence. The typical height of the barriers, close to and even higher than $10\,k_BT$, is significantly higher than in the smectic phase [175–177]. This statement can be made more explicit by comparing our data at $P^* = 3.5$ ($\eta = 0.563$) with those of Ref. [175] for the smectic phase of a system of parallel hard spherocylinders with $L^* = 5.0$ at pressure $P^* = 5.0$ ($\eta = 0.563$). In the latter case the height of the free-energy barrier reaches a value close to $8\,k_BT$ [176].

6.5 Permanent and transient caging

In the present section we study the diffusion dynamics in terms of the time-dependent particle-particle correlation functions (van Hove functions). First, we focus on the

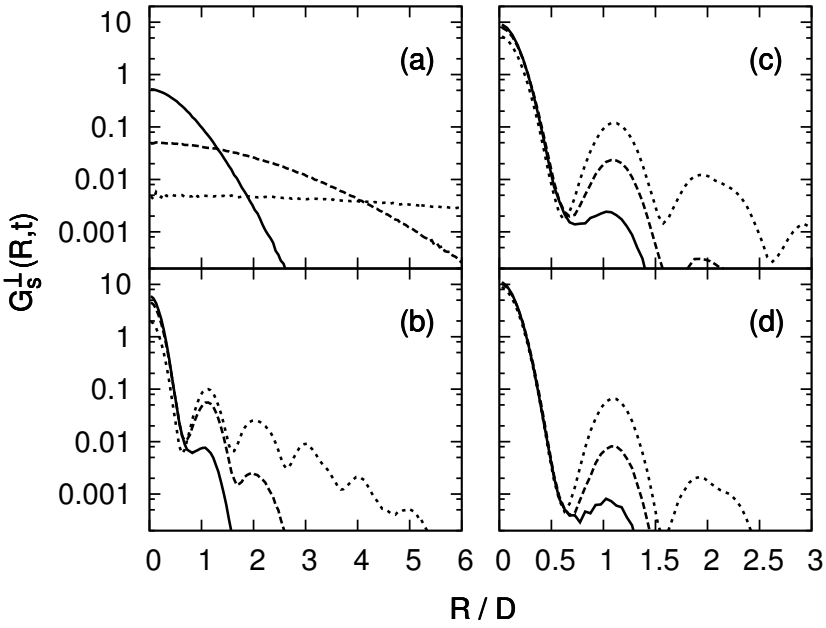

Figure 6.5: Transverse component of the self-part of the van Hove function $G_s^{\perp}(R,t)$ as a function of the in-plane distance $R = \sqrt{x^2 + y^2}$ for a binary mixture of perfectly aligned hard spherocylinders with length-to-diameter ratio $L_1^* = 2.1$ and $L_2^* = 1.0$ and relative concentrations $x_1 = 0.375$ and $x_2 = 0.625$ at $t/\tau = 1$ (solid lines), $t/\tau = 10$ (dashed lines) and $t/\tau = 100$ (dotted lines) for a system at reduced osmotic pressure (a) $P^* = 2.5$, (b) $P^* = 3.0$, (c) $P^* = 3.5$ and (d) $P^* = 4.0$.

single-particle diffusion by considering the self-part of the van Hove function (SVHF), then we concentrate on the collective character of the diffusion by studying its distinct-part (DVHF). As highlighted in Sec. 6.3, it is worth analyzing separately the transverse (xy) and longitudinal (z) components of the van Hove functions. In such a way, one can study the effect of the spontaneous symmetry breaking (present in the xy plane, absent along the z axis) on the dynamics of the system. In other words, one can analyze separately the role of the "permanent" (in the xy plane) and "transient" (along the z axis) dynamic caging phenomena on the overall heterogeneous dynamics.

In order to analyze the details of the single-particle diffusion, we report in Fig. 6.5 and 6.6 the self-part of the van Hove function (SVHF) at different times. Let us start by focusing in Fig. 6.5 on the SVHF in its transverse component. The comparison between the transverse SVHF in the nematic (Fig. 6.5(a)) and in the columnar (Fig. 6.5(b)-(d)) phase reveals a drastic change in the dynamics associated

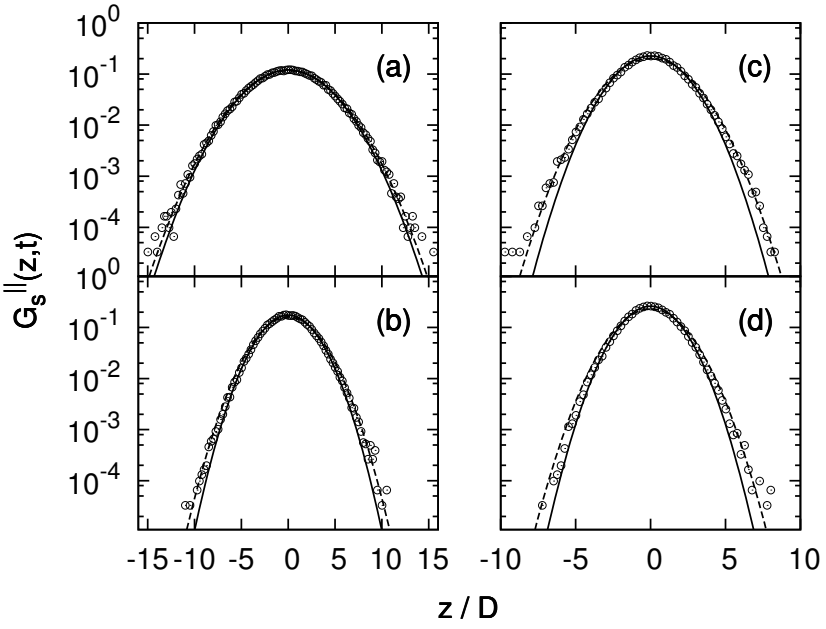

Figure 6.6: Longitudinal component of the self-part of the van Hove function $G_s^{\parallel}(z,t)$ as a function of z/D for $t/\tau = 20$ and pressure (a) $P^* = 2.5$, (b) $P^* = 3.0$, (c) $P^* = 3.5$ and (d) $P^* = 4.0$. The curves refer to Gaussian fits over points near the origin (solid lines) and the tails (dashed lines).

with the phase transition. The transverse SVHF in the nematic phase is a monotonic function which broadens with time. By entering the columnar phase one observes the appearance of peaks, which manifest the long-range hexagonal order in the xy plane. As expected, the number and height of the peaks after a given time decreases with the packing fraction due to the higher free-energy barriers (cf. Sec. 6.4).

In the density-functional theory analysis of Ref. [173] it was shown that, in order to properly describe the equilibrium dynamics of a liquid-crystal phase, it is not sufficient to consider the effect of the "permanent" caging barriers. One has also to take into account the "transient" caging effect in the direction(s) where the translational symmetry is not broken. In fact, the overall heterogeneous dynamics develops as a result of the coupling between these two different caging phenomena [173]. Therefore, let us move our attention to the self diffusion in the z direction, along which the system is homogeneous. A careful analysis of the longitudinal component of the SVHF in Fig. 6.6 confirms the presence of a weakly heterogeneous diffusion even along the z axis. In fact, if along the z axis the diffusion was Gaussian, it would be possible to fit the points in Fig. 6.6 with a single Gaussian function. On the

contrary, by performing this fit on different intervals on the z axis, i.e., in the region near the origin (solid line in Fig. 6.6) and the tails (dashed line), two different curves are obtained. Although the deviations between the two sets of curves are limited, this behavior manifests interesting resemblances with the heterogeneous dynamics of some non-equilibrium amorphous systems, such as supercooled liquids and gels. For such systems the two-Gaussian fitting is used to distinguish between "slow" and "fast" particles [187, 188]. The columnar structure of the system should not be considered the primary cause for this dynamic heterogeneity, since analogous deviations can be detected also for the nematic phase in Fig. 6.6(a). Instead, the high packing fraction should be considered the reason for these small discrepancies from Gaussian diffusion.

The study of the SVHF gave us many insights on the single-particle diffusion. We turn now our attention to the DVHF in order to analyze the time evolution of the nearest-neighbor (solvation) shell. In fact, it is the structure of the fluid around a particle that determines the (permanent or transient) cage that frustrates the single-particle diffusion. We report in Fig. 6.7 the DVHF Eq. (6.6) in its transverse (left column) and longitudinal (right column) component at time $t/\tau = 0.02$, 2 and 20. At time $t = 0$ the DVHF coincides with the pair-distribution function, and it is thus characterized by a region around the origin where its value is equal to zero due to the excluded volume interactions. In the opposite limit, that is when $t \to \infty$, the DVHF of a homogeneous state is expected to be a constant due to the decay of the positional correlations. This does not happen in the presence of spontaneous translational-symmetry breaking due to the long-range positional ordering.

In each graph of Fig. 6.7 at $t/\tau = 0.02$ (dotted line) a region around the origin where the DVHF is close to zero suggests that each particle is still rattling around its initial position. A series of peaks developing away from the origin indicates the preferential positions of the neighboring particles. In the nematic phase at $t/\tau = 0.02$ one can recognize in both the transverse (Fig. 6.7(a)) and longitudinal (Fig. 6.7(e)) components a liquid-like structure. The lack of long-range order is testified by the rapid decay of the peaks by moving away from the origin. Interestingly, the DVHF assumes a functional dependence close to a constant already at $t/\tau = 2$ (dashed line). This means that on average in the time interval $t/\tau = 2$ a given particle i can escape the trapping cage formed by its nearest neighbors j, and the space originally occupied by i is filled by one of the j particles.

The picture changes appreciably when passing to the columnar phase (Fig. 6.7(b)-(h)). The most visible change with respect to the nematic phase consists of the long-range modulations in the transverse component of the DVHF (Fig. 6.7(b)-(d)) due to the columnar structure. On the other hand, the form of the longitudinal component (Fig. 6.7(f)-(h)) does not display any qualitative change linked to the nematic-columnar transition. However, one can in this case observe a quantitative change in the dynamics. In fact, the time a particle needs to leave its initial position within a column (z component) increases considerably in the columnar phase. Whereas the relaxation times of the longitudinal DVHF in the three columnar systems are comparable (Fig. 6.7(f)-(h)), a much faster relaxation in the nematic phase

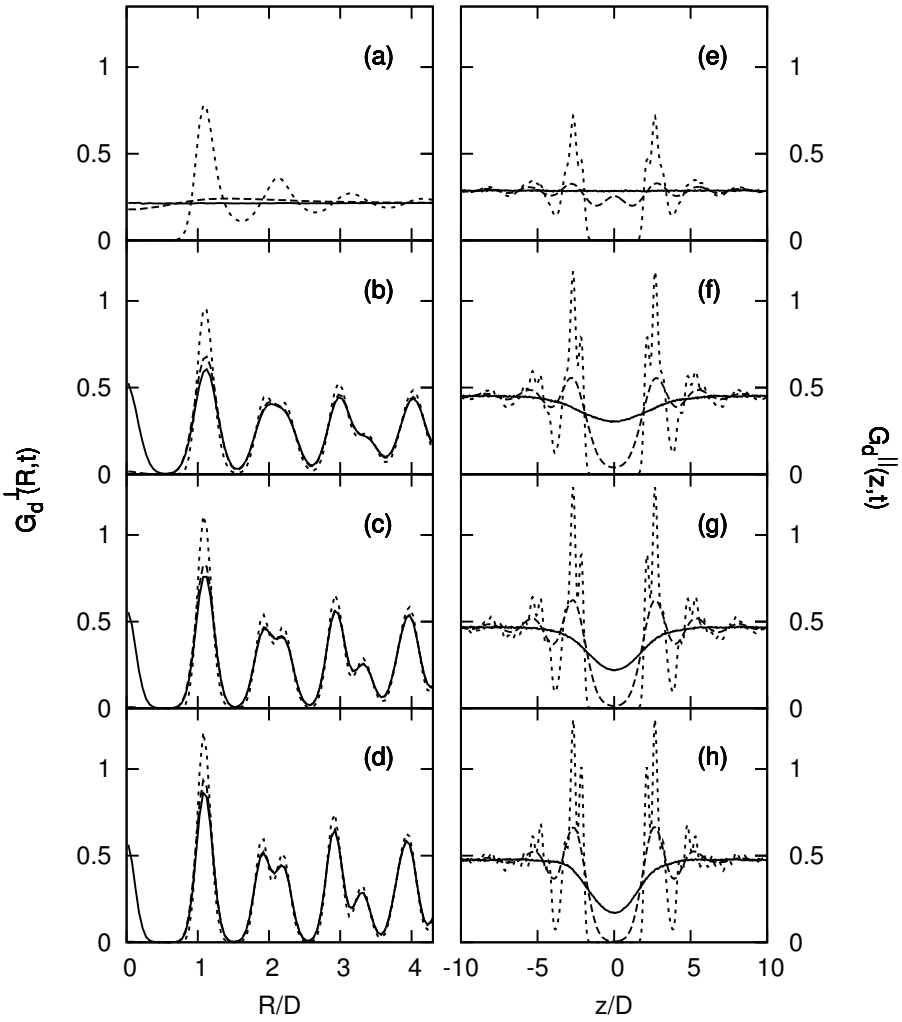

Figure 6.7: Transverse $G_d^{\perp}(R,t)$ ((a)-(d)) and longitudinal $G_d^{\parallel}(z,t)$ ((e)-(h)) component of the distinct-part of the van Hove function evaluated for the same system and state points as in Figs. 6.5 and 6.6 and at $t/\tau = 0.02$ (dotted lines), $t/\tau = 2$ (dashed lines), $t/\tau = 20$ (solid lines) at $P^* = 2.5$, 3.0, 3.5 and 4.0 (from top to bottom).

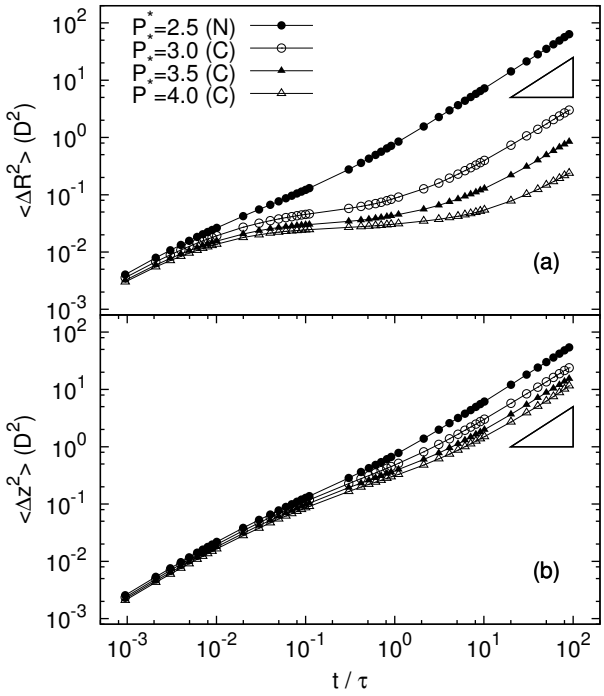

Figure 6.8: Mean square displacement in the direction (a) perpendicular $\langle \Delta R^2 \rangle$ and (b) parallel $\langle \Delta z^2 \rangle$ to the nematic director in units of D^2 as a function of t/τ for the same system and state points as in Figs. 6.5-6.7. The triangles in each plot show the slope characterizing a linear dependence on t.

is detected (Fig. 6.7(e)). The difference in packing fraction alone cannot explain such a slowing down of the longitudinal dynamics. We argue that such an effect is due to a coupling between the in-column and in-plane dynamics. In other terms, the higher in-plane mobility of the nematic phase with respect to the columnar phase affects the mobility along the nematic director. This confirms the results of Ref. [173], that is, that permanent and transient caging are in effect coupled phenomena.

6.6 Non-Gaussian diffusion

An effective way to identify dynamical heterogeneities consists of individuating deviations from linearity of the mean square displacement in time. It is well known that the statistics of the displacements of an isolated colloid follows a Gaussian distribution, whose mean square displacement varies linearly with time [3]. The

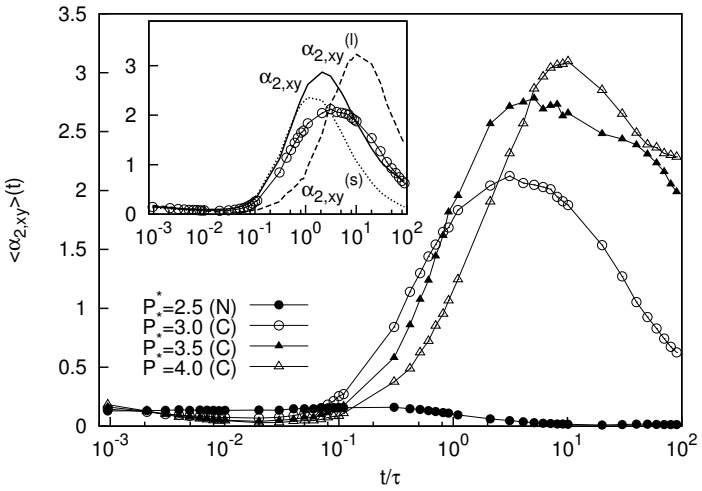

Figure 6.9: Non-Gaussian parameter $\langle \alpha_{2,xy} \rangle(t)$ of the diffusion in the plane perpendicular to the nematic director as a function of t/τ for the same system and state points as in Figs. 6.5–6.8. In the inset we compare at $P^* = 3.0$ the non-Gaussian parameter averaged over the concentrations (open circles) with those relative to species 1 ($\alpha^{(l)}_{2,xy}$, dashed line), to species 2 ($\alpha^{(s)}_{2,xy}$, dotted line) and of the whole system ($\alpha_{2,xy}$, solid line).

situation can change appreciably in the presence of other particles. The local cage trapping in systems close to dynamical arrest and the partial long-range order in liquid crystals determine an intermediate time regime, where the dynamics is strongly subdiffusive. This means that in this regime the mean square displacement has a power-law dependence on time with an exponent smaller than one. In Fig. 6.8 we show the MSD both (a) in the xy plane and (b) along the z direction. In the plane perpendicular to the nematic director (Fig. 6.8(a)) one can appreciate the almost linear trend of the MSD in the nematic phase. On the other hand, by increasing the pressure and going to the columnar phase, an intermediate plateau region appears. The deviations from linearity associated with this plateau are tightly related to the non-Gaussian features of the self-part of the van Hove function, and can be quantitatively estimated by the non-Gaussian parameter defined in Eq. (6.9). In Fig. 6.9 we report the NGP in the xy plane after averaging over the species concentrations, as described in Eq. (6.10). This parameter takes an almost constant value close to zero in the nematic phase. On the contrary, in the columnar phase the NGP displays a peak at intermediate times, thus indicating deviations from Gaussianity. Along the z direction (not shown here) the NGP does not deviate significantly from zero in either the nematic or the columnar phase. The choice of calculating the NGP by performing a weighted average over the two components of the mixture allows to take into account the effects related to the structure of the system only, while neglecting

trivial non-Gaussianity due to the size asymmetry of the species [186]. For the sake of completeness, we show in the inset of Fig. 6.9 a comparison between the NGP at the reduced osmotic pressure $P^* = 3.0$ for each species, their weighted average and for the system as a whole. The operation of averaging does not affect significantly the position of the peak, that is, the duration of the non-Gaussian regime, but has the only effect of decreasing the peak height. This suggests that by means of this operation the non-Gaussianity due to the particles size difference is subtracted.

The dynamic inhomogeneities, as captured by both the MSD and the NGP in the transverse component of the columnar phase, allow to identify three different time regimes. There is a short-time regime, where the MSD follows the linear trend typical of weakly-interacting fluids and the NGP maintains a value close to zero. During this regime the particles diffuse freely on length-scales smaller than the average column radius and do not feel the trapping cage due to the surrounding particles yet. On an intermediate time regime the MSD becomes strongly subdiffusive and the NGP is characterized by a monotonic growth: the free diffusion is inhibited by the columnar structure of the fluid. At this stage one can distinguish between particles that still rattle within their column (slow particles), and others that succeeded in overcoming the energetic barrier and jumped to another column (fast particles). At the end of the subdiffusive plateau a third time regime starts, where the MSD returns to a linear time dependence and the NGP reaches a peak. When the peak of the NGP starts decreasing monotonically to zero, most of the particles succeeded in leaving their initial column. A deeper inspection on the pressure dependence of the NGP shows that the degree of non-Gaussianity, i.e., the height of the peak, and the duration of the caging regime, i.e., the position of the peak, increase with the packing fraction. It is reasonable to explain this fact by considering that the cage escape is related to a rearrangement of the surrounding particles, which becomes slower at higher packing, as it involves more of them. Finally, the small deviations from linearity in the longitudinal MSD (Fig. 6.8(b)) confirm the presence of a weakly heterogeneous dynamics, as already pointed out in the analysis of the longitudinal self-part of the van Hove function in Sec. 6.5.

6.7 Structural relaxation

Finally, the structural relaxation of the system is analyzed in terms of the transverse and longitudinal components of the self-part of the intermediate scattering function (SISF). Along the z axis, where the system is homogeneous, the pairwise correlations are characterized by a single-step decay at each pressure independently of the phase, as depicted in Fig. 6.10(b). On the other hand, Fig. 6.10(a) shows that a plateau region in the transverse SISF appears when the system develops the columnar ordering. This plateau, whose value increases with pressure, indicates the duration of the caging regime and is expected to divide a short-time decay (β-relaxation) from a long-time one (α-relaxation). As previously observed in recent work on smectic liquid crystals [175–177] and in out-of-equilibrium supercooled

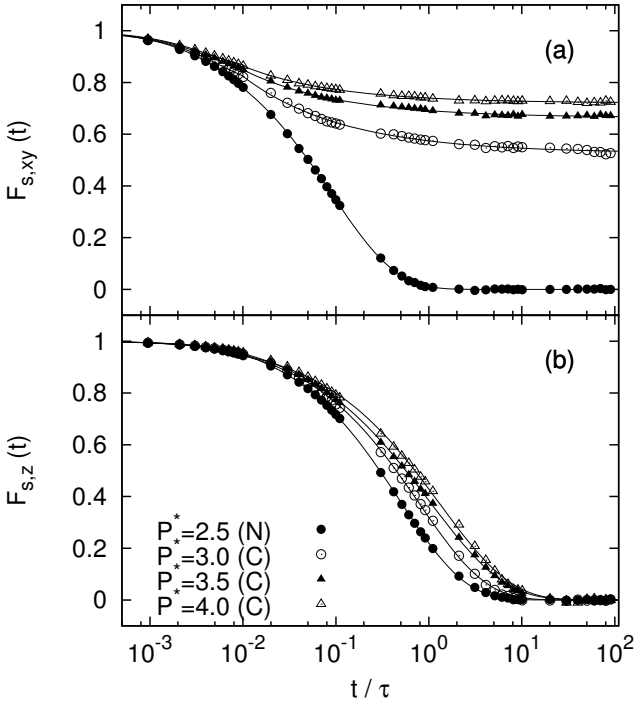

Figure 6.10: Self-part of the intermediate scattering function $F_{s,xy}(t)$ and $F_{s,z}(t)$ evaluated at wave vectors corresponding to the first peak of the structure factor (a) in the plane perpendicular to the nematic director and (b) along it. The data correspond to the same system and state points as in Fig. 6.5-6.9. The solid lines are fits (see text).

liquids [189], the SISF is expected to decay to zero at long times due to the loss of density autocorrelations. This kind of behavior was observed for the smectic phase in Refs. [175–177], where the α-relaxation decay was fitted by a stretched exponential function of the form $\exp[(t/t_r)^{\beta}]$ with $\beta \simeq 0.6$ and t_r the characteristic relaxation time. In the present simulations we did not observe any α-relaxation, as the relaxation time of the systems exceeds our simulation time. From the available data it is possible to observe a close accordance between the features of the columnar structural relaxation with that characterizing smectic states. In particular, the β-relaxation in the xy plane is accurately described by an exponential decay due to the weak interactions with the nearest neighbor particles at short times. Moreover, the relaxation along the z axis resembles accurately the in-layer relaxation of smectic states. In fact, in both the longitudinal columnar and transverse smectic SISF, the particle-particle correlations appear to depend weakly on the pressure and the long-time decay is

well approximated by a stretched exponential with $\beta \simeq 0.6$.

6.8 Conclusions

In summary, we used Monte Carlo simulations to analyze the presence of dynamical heterogeneities in a columnar liquid crystal of perfectly aligned hard spherocylinders. The effect of the long-range hexagonal order in the plane perpendicular to the nematic director can be interpreted in terms of an effective mean-field potential. Such a mean-field potential tends to confine the particles inside a column, while preventing them to occupy positions in between two columns. In analogy with previous analyses on the smectic phase, the height of the free-energy barriers associated with a column-to-column jump increases with the packing and the particle anisotropy. As a consequence, in the columnar plane the dynamics of a rod develops in quasi-quantized steps: particles rattle around the position of a column, while jumping to another column only when the configuration of the surrounding particles allows it.

The in-plane rattling-and-jumping dynamics gives rise to three different time regimes. At very short times, the particles diffuse almost freely, while not feeling the presence of the surrounding particles yet. At this stage the behavior of the system is that typical of a simple fluid, characterized by a Gaussian distribution of displacements, a linear mean square displacement and an exponential structural relaxation. A second stage starts when particles begin experiencing the cage due to the long-range columnar structure. As a result, the mean square displacement as well as the self-intermediate scattering function develop a plateau, whose duration increases with the packing. Correspondingly, the distribution of displacements shows marked deviations from Gaussianity with the appearance of peaks corresponding to the hexagonal lattice positions. Nonetheless, after longer time intervals the number of "fast" particles, which succeeds in overcoming the energetic barrier, increases with respect to the "slow" ones. When most of the particles succeeds in leaving their initial column, a second diffusive regime starts, indicating the end of the cage regime.

While studying the longitudinal in-column dynamics of the columnar phase, we observed interesting analogies with the heterogeneous dynamics of smectic states. Along the nematic director of our columnar phase the system does not develop any long-range order, and it is thus expected to behave like a liquid. Even in the absence of long-range positional order, we noticed interesting, although slight, deviations from Gaussian diffusion both in the distribution of displacements and in the mean square displacement. As far as the structural relaxation is concerned, this fact is testified by a self-intermediate scattering function well approximated by a stretched-exponential, as occurs in dense liquids close to a dynamical arrest transition. For these reasons we confirm previous studies on the smectic phase: along the direction in which a liquid crystal does not develop any long-range order the dynamics is close to that of a dense liquid. These results should be compared with recent

experiments on the columnar phase of a suspension of *fd* virus particles [178]. In these experiments huge deviations from Gaussian diffusion were observed in the direction perpendicular to the columnar plane. This happens to be in striking contrast with our observations, which testify only slight deviations from Gaussian diffusion. However, a recent analysis seems to suggest that such a strongly heterogeneous dynamics was determined by the multi-domain structure of the experimental columnar system [190] and was therefore not observable in the present study, where the columnar phase is investigated in the bulk.

Acknowledgements

It is a pleasure to thank M. P. Lettinga, E. Grelet and E. Pouget for sharing preliminary experimental results that motivated this work and D. El Masri, P. van der Schoot and S. Naderi for stimulating and useful discussions.

Chapter 7

A minimalist microscopic theory for capillary forces between colloids

Abstract

The control of thermosensitive solvent-induced interactions offers a simple and practical way to reversibly manipulate the aggregation between colloids. In this chapter we focus on the effective interactions arising when the solvent is close to a fluid-fluid phase separation. Starting from a framework of density functional theory, we develop the simplest theory aimed at predicting from first principles such effective interactions. The quality of this theory in the planar geometry is assessed by comparing its predictions with other numerically exact theories. Although this simplified approach does not account correctly for the long-distance decay of the local particle density, the description of the capillary-condensation force between two planar surfaces is globally more than satisfactory. However, inconsistencies arise when approaching the fluid critical temperature.

7.1 Introduction

One of the most striking features of colloids is their ability to self-assemble into a virtually infinite variety of macroscopic structures. This happens to be the case since the interactions between colloids can be tuned almost at will [9]. Tailoring the "bare" (i.e., in vacuum) interactions is a daunting task, which involves the manipulation of the colloids' chemical properties. It is often much easier and convenient to adjust their "effective" interactions, i.e., those interactions arising due to the presence of the solvent. Typical examples through which effective interactions are manipulated comprise the modification of the solvent's electrostatic properties [191, 192] and the addition to the suspension of a non-adsorbing depletant [71, 72]. All these approaches involve an irreversible change in the composition of the system. On the other hand, the perspective of adjusting the effective colloid-colloid interactions by a change in temperature alone, that is, without any change in composition, is particularly appealing. In fact, these thermosensitive effective interactions would offer a simple yet effective way to control colloidal aggregation in a reversible way.

The subject of this chapter are the thermosensitive effective interactions induced by the inhomogeneities of a molecular solvent in the vicinity of the colloids. In most situations the equilibrium behavior of a colloidal suspension is deduced by treating the solvent as a "passive actor" on the scene. According to this approximation, one assumes the properties of the solvent to be the same in each point of the system and identical to those of the bulk. This assumption grossly fails when the solvent state point is in the proximity of a fluid-fluid phase separation, where solvent inhomogeneities can become non-negligible. In colloidal suspensions this situation arises when the solvent consists of a binary mixture, whose phase diagram contains a demixing region. Systems of this type have been first studied by Beysens and Estéve, who showed that silica colloids tend to aggregate when the solvent, a binary mixture of 2,6-lutidine and water, is close to demixing [193]. Such a phenomenon is known to be related to the formation of wetting layers of one of the two components of the solvent on the colloid due to a surface preferential adsorption. However, there is not univocal agreement on the specific mechanism involved in the process [194–198]. More recently, the study of colloidal aggregation in binary solvents found renewed attention for solvent state points close to the demixing critical point [199, 200], where long-range critical Casimir forces are expected [201, 202].

In this chapter we focus on the effective interactions arising between colloids when the solvent is close to a fluid-fluid phase separation, but far enough from the critical point. These colloid-colloid effective interactions arise due to solvent inhomogeneities, which in turn develop as a consequence of the preferential adsorption of one of the solvent components on the colloid's surface. Since the seminal work of Cahn it is known that such preferential adsorption can give rise to an adsorbed layer of macroscopic size (wetting transition) [203–205]. Understanding the surface phase behavior of a fluid is of fundamental relevance to deduce its properties in confinement [206–208]. Under given conditions the confining surfaces can stabilize phases otherwise metastable, leading to a *capillary condensation* phase transition. This phenomenon can lead to the appearance of *capillary forces* between the elements that confine the fluid [207]. In the past decades density functional theory has proven its effectiveness in the study of the surface phase behavior of fluids, shedding light on the role of ingredients, such as, the adsorption surface curvature [209–211] and the range of the solvent-solvent interactions [211–213]. More importantly, density functional theory offers an approximate way to evaluate from first principles the solvent-mediated interactions between colloids due to solvent inhomogeneities [214–216]. However, these studies are often based on lengthy computations associated with the numerical minimization of a functional with respect to a function defined on a two-dimensional space [215, 216]. This fact poses severe practical limitations to the application of the theory to more complex configurations.

The goal of this chapter is to develop the simplest density functional theory for the solvent-mediated effective interactions between colloids due to a solvent preferential adsorption. In fact, a simplified and quickly-solvable theory could furnish an efficient way to calculate effective interactions in configurations, such as in the presence of more than two particles, where the application of the full theory would

require appreciably more complex and time-consuming computations. The starting point of this work is a density functional theory that treats the short-range repulsion between the solvent particles by means of a local density approximation (LDA, cf. Sec. 2.3.4), while the long-range van der Waals attraction is introduced by means of a non-local mean-field term (MF, cf. Sec. 2.3.4). The theory developed in this chapter is *minimalist* since it involves the least number of scalar parameters to be (numerically) minimized. This procedure of reduction of the theory degrees of freedom is implemented by imposing a specific functional form to the inhomogeneous single-particle density, namely the so-called sharp-kink parameterization. In other words, instead of allowing for a "free" minimization of the density functional, we consider a "constrained" minimization over a subset of functions. The process of reduction of the free parameters of the theory is expected to introduce deviations from its exact predictions. In order to quantify these deviations, we analyze the reliability of the theory in the simplest geometry, characterized by planar symmetry. We consider here (i) a fluid in contact with a single wall and (ii) a fluid confined between two walls. We compare the outcome of this minimalist theory with those obtained by means of the free minimization of the same theory (LDA-MF) and of an even more sophisticated theory based on the fundamental measure theory (FMT-MF) [26]. We show that in the single-wall configuration the sharp-kink parameterization approach fails to account for the wetting transition, which is instead well described by the two freely minimized theories. On the other hand, we demonstrate that such an approach works very well in reproducing the behavior of a fluid confined by two planar walls. We obtain predictions for the effective interaction between the walls which are in good quantitative agreement with the freely minimized theory. Relevant deviations, however, develop at high temperature in proximity of the critical point. The findings described in this chapter prove the validity of the minimalist approach for the description of the effective interactions between colloids induced by the capillary condensation. Such an analysis opens perspectives for the study of more complex and interesting configurations and geometries.

7.2 Solvent-mediated potential

In order to introduce the concept of solvent-mediated potential, let us consider a colloidal suspension in equilibrium at temperature T in a volume V. We indicate with μ_c and μ_s the chemical potential of colloids and solvent, respectively. We denote with $\mathbf{X}_c$ the generalized coordinates of the colloids, and with $\mathbf{X}_s$ those of the solvent molecules. Let $\mathcal{U}_{cc}(\mathbf{X}_c)$ be the potential energy of N_c colloids, $\mathcal{U}_{ss}(\mathbf{X}_s)$ that of N_s solvent molecules and, finally, $\mathcal{U}_{cs}(\mathbf{X}_s, \mathbf{X}_c)$ the interaction potential energy between N_c colloids and N_s solvent molecules. The grand canonical partition function of the system reads

$$\Xi(T,V,\mu_c,\mu_s)=\sum_{N_c,N_s=0}^{\infty}\frac{\exp(\beta\mu_c N_c+\beta\mu_s N_s)}{\mathcal{V}_c^{N_c}\mathcal{V}_s^{N_s}N_c!N_s!}\int d\mathbf{X}_c d\mathbf{X}_s \exp\left[-\beta(\mathcal{U}_{cc}+\mathcal{U}_{ss}+\mathcal{U}_{cs})\right], \tag{7.1}$$

where $\mathcal{V}_c$ and $\mathcal{V}_s$ are the thermal volume of colloids and solvent, respectively. By performing a partial integration over the solvent degrees of freedom, Eq. (7.1) can be expressed as

$$\Xi(T,V,\mu_c,\mu_s)=\sum_{N_c=0}^{\infty}\frac{\exp(\beta\mu_c N_c)}{\mathcal{V}_c^{N_c}N_c!}\int d\mathbf{X}_c \exp\left[-\beta\left(\mathcal{U}_{cc}(\mathbf{X}_c)+\Omega_s(T,V,\mu_s,\mathbf{X}_c)\right)\right], \tag{7.2}$$

where $\Omega_s(T,V,\mu_s,\mathbf{X}_c)$ is the grand potential of the solvent *in the presence* of the external force field exerted on the solvent molecules by the N_c colloids with coordinates $\mathbf{X}_c$. Eq. (7.2) expresses explicitly the fact that, if one is interested in the equilibrium properties of the colloids only, the suspension can be regarded as a pure collection of colloids interacting via an additional *solvent-mediated* potential.

The transition from Eq. (7.1) to (7.2) is merely cosmetic, and the evaluation of the potential $\Omega_s(T,V,\mu_s,\mathbf{X}_c)$ is expected to be at least as difficult as the solution of the thermodynamics of the system as a whole. However, the procedure offers great advantages if approximations for $\Omega_s(T,V,\mu_s,\mathbf{X}_c)$ can be applied. In such cases, in fact, one can hope to properly account for the effect of the solvent by means of relatively simple two-body interaction terms. Well-known examples of approaches of this type in colloidal science comprise the DLVO theory for charged colloids in ionic solutions [191, 192] and the Asakura-Oosawa potential to account for the presence of non-adsorbing depletants [71, 72]. In this chapter we focus on the effective interaction between two colloids, modeled as two parallel planes. By denoting with $\Omega_s(T,V,\mu_s,d)$ the grand potential of a solvent confined between two planar walls separated by a distance d, the solvent-mediated potential between the walls is conveniently redefined as

$$U(d)=\Omega_s(T,V,\mu_s,d)-\Omega_s(T,V,\mu_s,d\to\infty), \tag{7.3}$$

which satisfies the condition $U(d\to\infty)=0$. Since in what follows we focus on the solvent degrees of freedom only, with the colloids treated as external force-fields sources, from now on each thermodynamic quantity will implicitly be referred to the solvent, and the subscript *"s"* will be dropped.

7.3 Model

The subject of this work is the solvent-induced aggregation of colloids when the solvent is close to a fluid-fluid phase separation. In experiments such a fluid-fluid

phase separation appears as a demixing instability of the two species composing a binary solvent [193]. Therefore, a theoretical work aimed at faithfully reproducing the experimental system would require as a starting point a good microscopic theory for such a demixing transition. Although this kind of theories for specific model systems exist [215, 216], we are interested in considering the phenomenon in generality. The main requirement we ask to the present model is that of developing a thermodynamic instability between two distinct isotropic and homogeneous phases. In other words, we require the model to undergo a phase transition belonging to the Ising universality class [217]. The simplest among such models is a pure system of particles characterized by a short-range repulsion and a long-range attraction, which since the pioneering work of van der Waals is known to undergo a gas–liquid phase separation [218]. We do not expected the particular parameterization of the short-range repulsion to appreciably influence the thermodynamics of the system [16], thus we model it as a simple hard-sphere repulsion. On the contrary, it is known that the details of the attractive part of the pair potential strongly affect the surface phase behavior of the system [204]. In order to reproduce the properties of real molecular fluids, we model the long-range attraction with an inverse power-law tail typical of dispersion forces. In summary, the pairwise potential between solvent molecules is

$$u(r) = \begin{cases} \infty & \text{if } r < \sigma, \\ u_{\text{att}}(r) & \text{if } r \geq \sigma, \end{cases} \tag{7.4}$$

where σ is the molecular diameter and the attractive component is given by

$$u_{\text{att}}(r) = -4\epsilon \left(\frac{\sigma}{r} \right)^6, \tag{7.5}$$

with ϵ a parameter which sets the microscopic energy scale.

We assume that also the interaction between solvent and colloids are governed by dispersion forces. The interaction between a solvent molecule and a colloid molecule is supposed to be of the Lennard-Jones type. By integrating over the positions of the colloid's molecules, which in the planar geometry are assumed to be homogeneously distributed in the region $z < 0$, it follows that the external potential experienced by the solvent particles due to a planar wall takes the form

$$V_w(z) = 4\epsilon_w \left[\frac{2}{15} \left(\frac{\sigma_w}{z} \right)^9 - \left(\frac{\sigma_w}{z} \right)^3 \right], \tag{7.6}$$

which is also known as the "Lennard-Jones 9-3 potential". Without loss of generality, in this work we analyze the specific choice of parameters $\epsilon_w/\epsilon = 1.6$ and $\sigma_w/\sigma = 1$.

7.4 Density functional theory

In Sec. 7.2 we explicitly showed that the solvent-mediated potential is essentially the grand potential of the solvent in the presence of the force field exerted by the colloids. The task of this chapter, which amounts to calculating the grand potential of a solvent in a general external potential field $V(\mathbf{r})$, is conveniently accomplished within the framework of density functional theory.

In density functional theory the grand potential of a system of particles at temperature T and chemical potential μ in an external potential $V(\mathbf{r})$ is calculated as the minimum of the functional $\Omega_v[\rho]$, defined as

$$\beta\Omega_v[\rho] = \beta\mathcal{F}[\rho] - \int d\mathbf{r}\beta\big(\mu - V(\mathbf{r})\big)\rho(\mathbf{r}), \tag{7.7}$$

where $\beta = (k_B T)^{-1}$, k_B is the Boltzmann constant and $\mathcal{F}[\rho]$ is the intrinsic free-energy functional. The function $\rho(\mathbf{r})$ minimizing the functional is the equilibrium single-particle density. The intrinsic free-energy functional $\mathcal{F}[\rho]$ is the sum of an ideal part

$$\beta\mathcal{F}^{\text{id}}[\rho] = \int d\mathbf{r}\rho(\mathbf{r})\big\{\log\big[\rho(\mathbf{r})\mathcal{V}\big] - 1\ \big\}, \tag{7.8}$$

and an excess part $\mathcal{F}^{\text{exc}}[\rho]$ which is not known exactly and must be approximated.

A reliable density functional theory able to treat in a unified way the short-range repulsion and the long-range attraction between particles (cf. Sec. 7.3) does not at present exist. On the other hand, very good theories were developed for the description of both homogeneous [219] and inhomogeneous [28] hard-sphere fluids. Therefore, we build a density functional theory starting from the excess free energy of a reference hard-sphere system, to which the van der Waals attractive tail is added as a mean-field (MF) perturbation. The simplest density functional theory for hard spheres involves a local-density approximation (LDA) of the excess free energy for homogeneous states. The resulting LDA-MF theory reads

$$\beta\mathcal{F}^{\text{exc}}_{\text{LDA-MF}}[\rho] = \int d\mathbf{r}\bigg[f^{\text{exc}}_{hs}\big(\rho(\mathbf{r})\big) + \frac{1}{2}\int d\mathbf{r}'\beta u_{\text{att}}(|\mathbf{r}-\mathbf{r}'|)\rho(\mathbf{r})\rho(\mathbf{r}')\bigg], \tag{7.9}$$

where $f^{\text{exc}}_{hs}(\rho)$ is an approximation for the excess free energy per unit volume of the homogeneous hard-sphere fluid. For reasons that will be made explicit in what follows, we choose for $f^{\text{exc}}_{hs}(\rho)$ the excess free energy given by the scaled particle theory [220], according to which

$$f^{\text{exc}}_{hs}(\rho) = -\rho\log\big[1-v\rho\big] + \frac{\rho\big(6v\rho - 3(v\rho)^2\big)}{2\big(1-v\rho\big)^2}, \tag{7.10}$$

where $v = \pi\sigma^3/6$ is the hard-sphere volume. In spite of its simplicity due to the local-density approximation, the LDA-MF functional of Eq. (7.9) is expected to be

reliable enough, especially if the description focuses on length-scales appreciably larger than the molecular dimension σ. Nevertheless, we want to assess the validity of this assumption by comparing the LDA approximation for the reference system with a more sophisticated one based on the fundamental measure theory (FMT). In FMT even the hard-core repulsion is treated in a non-local fashion in order to reproduce the density modulations typical of high-density hard spheres. The FMT based functional reads

$$\beta\mathcal{F}^{\text{exc}}_{\text{FMT-MF}}[\rho] = \int d\mathbf{r}\Big[\Phi[\rho] + \frac{1}{2}\int d\mathbf{r}'\beta u_{\text{att}}(|\mathbf{r}-\mathbf{r}'|)\rho(\mathbf{r})\rho(\mathbf{r}')\Big], \tag{7.11}$$

where in the original formulation given by Rosenfeld [26]

$$\Phi[\rho] = -n_0\log\big[1-n_3\big] + \frac{n_1 n_2 - \mathbf{n}_1\cdot\mathbf{n}_2}{1-n_3} + \frac{n_2^3 - 3n_2\mathbf{n}_2\cdot\mathbf{n}_2}{24\pi\big(1-n_3\big)^2}, \tag{7.12}$$

and the weighted densities $\{n_\alpha(\mathbf{r})\}$ are obtained as convolutions of the single-particle density with geometry-inspired weight functions $w_\alpha(\mathbf{r})$ as

$$n_\alpha(\mathbf{r}) = \int d\mathbf{r}'\rho(\mathbf{r}')w_\alpha(\mathbf{r}-\mathbf{r}'). \tag{7.13}$$

The weight functions are

$$\begin{aligned} w_3(\mathbf{r}) &= \theta\Big(\frac{\sigma}{2}-|\mathbf{r}|\Big), & w_2(\mathbf{r}) &= \delta\Big(\frac{\sigma}{2}-|\mathbf{r}|\Big), \\ w_1(\mathbf{r}) &= \frac{w_2(\mathbf{r})}{2\pi\sigma}, & w_0(\mathbf{r}) &= \frac{w_2(\mathbf{r})}{\pi\sigma^2}, \\ \mathbf{w}_2(\mathbf{r}) &= \frac{\mathbf{r}}{r}\delta\Big(\frac{\sigma}{2}-|\mathbf{r}|\Big), & \mathbf{w}_1(\mathbf{r}) &= \frac{\mathbf{w}_2(\mathbf{r})}{2\pi\sigma}. \end{aligned} \tag{7.14}$$

In the homogeneous case the FMT functional $\Phi[\rho]$ reduces to the scaled-particle theory excess free energy, i.e., to Eq. (7.10). Although better approximations for the equation of state of homogeneous hard spheres exist [219], our choice for $f^{\text{exc}}_{hs}(\rho)$ in Eq. (7.9) fell on the scaled-particle theory in order to be consistent with the homogeneous-state limit of the fundamental measure theory.

7.5 The sharp-kink parameterization

Once an expression for the excess free-energy functional is known, the grand potential of the solvent under the effect of a given external potential can be calculated by numerically minimizing the functional Eq. (7.7). Such a minimization is typically performed by means of a discretization of the function $\rho(\mathbf{r})$ on a grid of points. This procedure is feasible in the case of highly symmetric geometries, where $\rho(\mathbf{r})$ can be reduced to a function of a single scalar variable. On the other hand, the complexity

of the problem and the time necessary for its numerical solution increases in less symmetric cases.

Starting from the density functional theory introduced in the previous section, we develop a simplified theory for the description of capillary forces. This approach is based on a drastic reduction of the free parameters of the theory, which allows for an appreciable increase in the calculation speed. The procedure of reduction of the free parameters consists of imposing a specific functional form to the single-particle density $\rho(\mathbf{r})$, while keeping undetermined a limited number of variational parameters defining it. This *ansatz* for the single-particle density is inserted into the functional Eq. (7.7), which in turn is minimized only with respect to the variational parameters. The parameterization adopted consists of assuming that the local density of a fluid under the effect of an external potential takes everywhere the bulk value ρ, but in a region $\mathcal{W}$ where the local density takes the value ρ_w. In summary, the ansatz for the single-particle density reads

$$\rho(\mathbf{r}) = \begin{cases} \rho_w & \text{if } \mathbf{r} \in \mathcal{W}, \\ \rho & \text{if } \mathbf{r} \in \overline{\mathcal{W}}, \end{cases} \tag{7.15}$$

where $\overline{\mathcal{W}} = \mathcal{D} \setminus \mathcal{W}$ and $\mathcal{D}$ is the total domain accessible to the fluid. Besides the density ρ_w, the other free parameters of the theory are those defining the region $\mathcal{W}$. By inserting the ansatz Eq. (7.15) into the LDA-MF theory defined in the previous section, we obtain for Eq. (7.7) the expression

$$\begin{aligned} \beta\Omega_v(\rho, \mathcal{W}) = V(\mathcal{W})\,\omega(\rho_w) + V(\overline{\mathcal{W}})\,\omega(\rho) + \beta a(\mathcal{W})\,\rho_w + \\ + \beta b(\mathcal{W}, \mathcal{W})\,\frac{\rho_w^2}{2} + \beta b(\mathcal{W}, \overline{\mathcal{W}})\,\rho\rho_w + \beta b(\overline{\mathcal{W}}, \overline{\mathcal{W}})\,\frac{\rho^2}{2}, \end{aligned} \tag{7.16}$$

where

$$\omega(\rho) = \rho[\log(\rho\mathcal{V}) - 1] + f_{hs}^{\text{exc}}(\rho) - \beta\mu\rho, \tag{7.17}$$

$$V(\mathcal{A}) = \int_{\mathcal{A}} d\mathbf{r}, \tag{7.18}$$

$$a(\mathcal{A}) = \int_{\mathcal{A}} d\mathbf{r}\, V(\mathbf{r}), \tag{7.19}$$

and

$$b(\mathcal{A}, \mathcal{B}) = \int_{\mathcal{A}} d\mathbf{r} \int_{\mathcal{B}} d\mathbf{r}'\, u_{att}(|\mathbf{r} - \mathbf{r}'|). \tag{7.20}$$

The explicit evaluation of the above-defined coefficients for the configurations studied in this chapter is reported in Appendix 7.A.

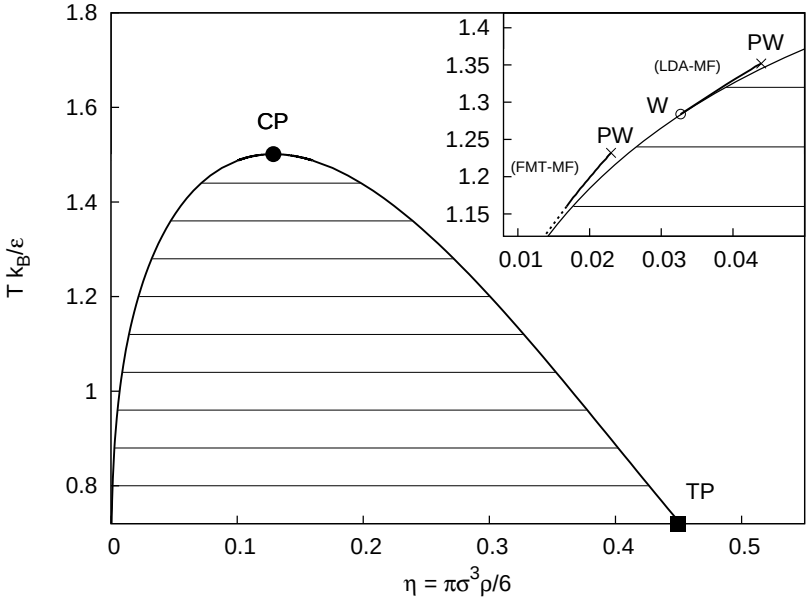

Figure 7.1: Bulk phase diagram of a homogeneous fluid with pairwise interactions defined by Eqs. (7.4)-(7.5) obtained by means of the approximate excess free-energy functional Eqs. (7.9)-(7.10), which in the homogeneous case coincides with Eqs. (7.11)-(7.12). The dashed area represents state points of gas-liquid phase separation, CP indicates the critical point and TP the triple point. The region of fluid-crystal coexistence is not shown here. Inset: surface phase transitions undergone by the fluid in contact with a planar wall exerting an energy potential described by Eq. (7.6) with $\epsilon_w/\epsilon = 1.6$ and $\sigma_w/\sigma = 1$. The top prewetting line in the inset is the prediction of the LDA-MF theory (cf. Eqs. (7.9)-(7.10)), the bottom line is the prediction of the FMT-MF theory (cf. Eqs. (7.11)-(7.12)). The dashed line serves as a guide to the eye for the identification of the wetting transition point of the FMT-MF theory, which could not be identified exactly. The wetting transition point (W) of the LDA-MF theory is highlighted by a circle. In both cases a cross identifies the critical pre-wetting point (PW).

7.6 Adsorption on a single wall

This section is devoted to an analysis that is preliminary with respect to the calculation of the solvent-mediated colloid-colloid potential. We concentrate on the simpler, but not trivial [204], situation of a solvent in contact with a single wall exerting the potential Eq. (7.6). The aim is to compare the physical description offered by the three density functional theories introduced in Sec. 7.4 and 7.5. The outcome of such an analysis will give us important insights on the reliability of each theory. In fact, some of the elements present in the single-wall configuration, such as the features

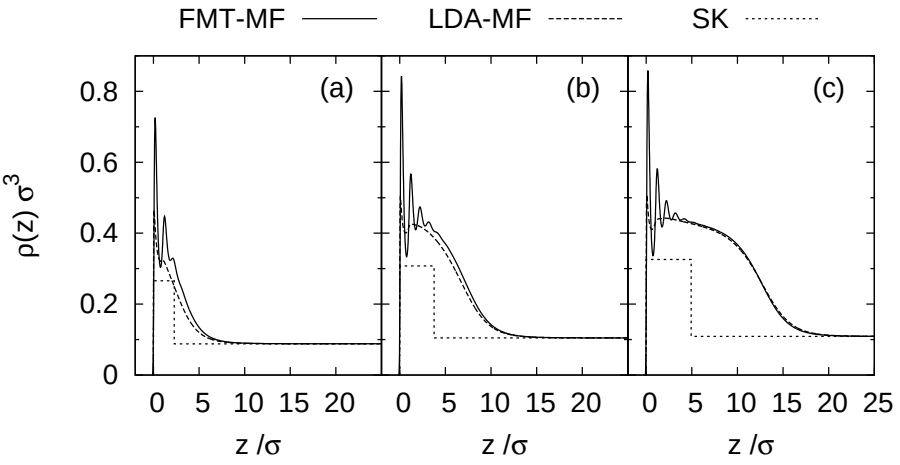

Figure 7.2: Single particle density profile $\rho(z)$ of a fluid with pairwise interactions defined by Eqs. (7.4)-(7.5) under the effect of the external potential Eq. (7.6). The profiles are calculated at temperature $k_B T/\epsilon = 1.40$ at values of the fluid chemical potential corresponding to a bulk density of (a) $\rho = 0.8\rho_{sat}$, (b) $\rho = 0.95\rho_{sat}$ and (c) $\rho = 0.99\rho_{sat}$, where ρ_{sat} is the gas saturation density. The different curves in each plot represent the outcome of different theoretical approaches: the free minimization of the FMT-MF functional (FMT-MF), the free minimization of the LDA-MF functional (LDA-MF), and the sharp-kink parameterization of the single-particle density of the LDA-MF functional (SK).

of the density long-distance decay and the existence of surface phase transitions, appear also in the presence of two confining walls. As a reminder, the theories we compare in this section are based on (a) a free minimization of the FMT-MF functional (cf. Eqs. (7.11)-(7.12)), (b) a free minimization of the LDA-MF functional (cf. Eqs. (7.9)-(7.10)) and (c) its sharp-kink (SK) parameterization (cf. Sec. 7.5).

Before addressing the case of a fluid in contact with a single planar wall, it is worth considering the bulk phase behavior of the homogeneous fluid. In Fig. 7.1 we report the bulk phase diagram of the fluid in terms of temperature T vs. packing fraction $\eta = \pi\rho\sigma^3/6$. The phase behavior of the system is that typical of a molecular fluid. In fact, the phase diagram is characterized by a curve of gas-liquid coexistence, a critical point (CP) at the top of this curve and a triple point (TP) of gas-liquid-crystal coexistence. The position of the triple point is approximate, and deduced from the simulations of the homogeneous Lennard-Jones fluid of Ref. [221].

In the presence of an interface with another phase the thermodynamic potential of a fluid can develop singularities that are not present in the bulk. In this case one talks about "surface phase transitions". The wetting transition is a typical example of such surface phase transitions. It is convenient to introduce the adsorption Γ of a fluid on a surface, defined as the excess amount of adsorbed particles with respect

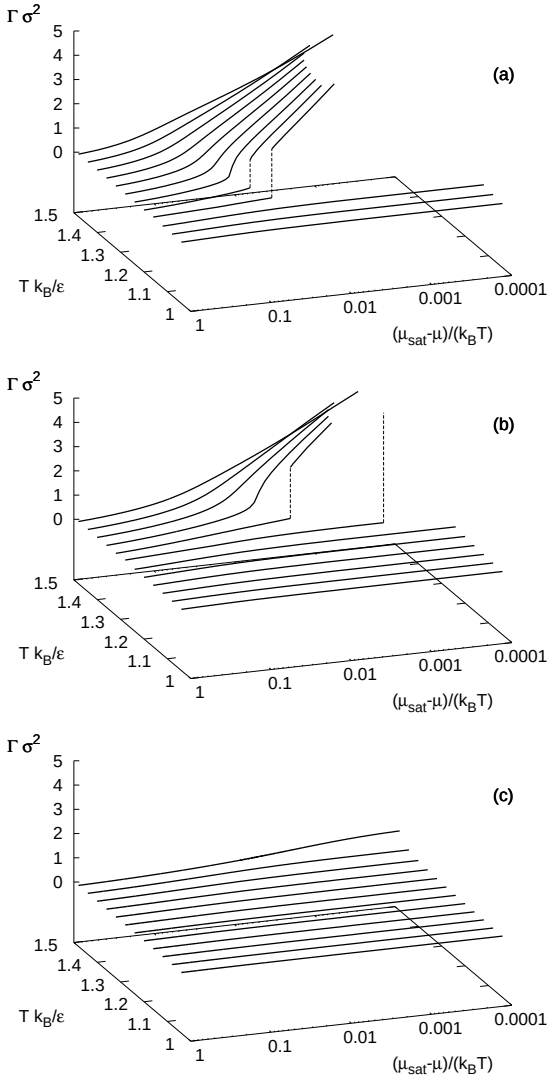

Figure 7.3: Adsorption Γ isotherms of a gas in contact with a wall exerting the potential Eq. (7.6) for different values of the gas chemical potential μ. The saturation value of the chemical potential μ_{sat} is defined as the chemical potential at which the bulk gas coexists with the liquid. The three graphs represent the calculations obtained by (a) the FMT-MF theory, (b) the LDA-MF theory and (c) the LDA-MF theory with the sharp-kink (SK) parameterization.

to the bulk per unit area. In terms of the equilibrium density profile $\rho(z)$ in the presence of a planar wall at position z_0, the adsorption can be expressed as

$$\Gamma = \int_{z_0}^{\infty} dz \left[\rho(z) - \rho\right], \tag{7.21}$$

where ρ is the density of the (bulk) fluid far from the wall, i.e., $\rho = \rho(z \to \infty)$. Let us consider the adsorption of a gas in contact with an attractive wall. In general, one observes a finite positive adsorption, which manifests as a thin dense fluid layer in contact with the wall. One could wonder what happens when the gas is brought isothermally towards saturation, i.e., coexistence with the high-density liquid. At low enough temperature one expects the adsorption to stay finite (partial wetting) [203]. On the other end, there is a wetting transition temperature, above which at saturation the adsorption diverges (complete wetting) [203]. In this case one expects the formation of a liquid-like layer, whose thickness diverges upon approaching bulk saturation. This situation is reported in Fig. 7.2 for a value of the temperature $Tk_B/\epsilon = 1.40$.

In Fig. 7.3 we report the adsorption of the fluid on a wall exerting the potential Eq. (7.6) at different values of the temperature T and chemical potential μ. We indicate with μ_{sat} the saturation chemical potential at which gas and liquid coexist at temperature T. The three plots correspond to the predictions of the three theories we aim at comparing: the freely minimized density functional theories FMT-MF (Fig. 7.3(a)) and LDA-MF (Fig. 7.3(b)) and the sharp-kink parameterization (SK) of the LDA-MF theory (Fig. 7.3(c)).

Let us first focus on the adsorption Γ of the two freely-minimized density functional theories as shown in Fig. 7.3(a) and (b). Note the logarithmic scale on the $\mu_{sat} - \mu$ axis. Qualitatively, the outcome of the two density functional theories coincide. In both Fig. 7.3(a) and (b) the adsorption at coexistence stays finite at sufficiently low temperature. However, at high enough temperature the adsorption diverges while approaching bulk coexistence, i.e., $\mu_{sat} - \mu = 0$. At first sight, the adsorption seems to diverge logarithmically upon approaching coexistence. This type of divergence is expected for short-range interactions (i.e., with finite range or exponentially decaying), and not for the long-range potential considered here. However, a closer inspection based on a fit analysis (not shown) demonstrates that the adsorption diverges algebraically with an exponent between -0.28 and -0.35, which is compatible with the mean-field prediction of $-1/3$ [204]. Besides the divergence at coexistence, the adsorption isotherms manifest another well-known phenomenon in the surface thermodynamics of molecular fluids. There is a range of temperature in which the transition from thin to thick adsorption layer develops in a discontinuous way. A jump in the adsorption vs. the chemical potential plots is observed in this case. The state points where this first-order surface phase transition develops define the so-called prewetting line. A more detailed inspection of the adsorption isotherms predicted by the two theories is given in Fig. 7.4. These plots allow to compare the predictions of the FMT-MF and the LDA-MF theory. A part from

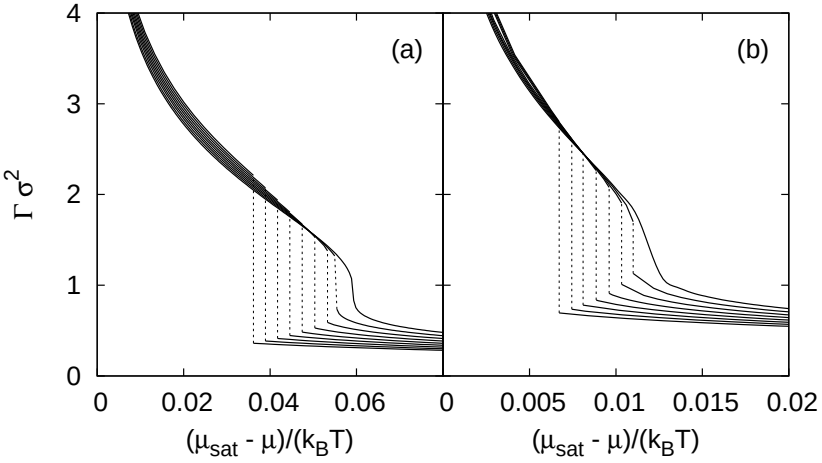

Figure 7.4: Adsorption Γ of a gas in contact with a wall exerting the potential Eq. (7.6) as a function of the chemical potential μ with respect to the gas-liquid coexistence chemical potential μ_{sat}. The discontinuity in the adsorption curves highlights the existence of a pre-wetting transition, also observable in Fig. 7.3, according to (a) the FMT-MF theory and (b) the LDA-MF theory. In both cases different lines correspond to adsorption isotherms at different temperature, corresponding to (from left to right) (a) $k_BT/\epsilon = 1.168, 1.176, 1.184, 1.192, 1.200, 1.208, 1.216, 1.224, 1.232$ and (b) $k_BT/\epsilon = 1.324, 1.328, 1.332, 1.336, 1.340, 1.344, 1.348, 1.352, 1.356$.

relevant quantitative deviations, particularly in the prewetting critical chemical potential and the adsorption discontinuities associated with the prewetting transition, the qualitative picture offered by the two theories is the same.

From the analysis of the adsorption isotherms of Figs. 7.3 and 7.4, one can draw the surface phase diagram of the model. Such surface phase diagram is shown in the inset of Fig. 7.1, where we report the prewetting line, critical prewetting point (PW), and wetting point (W) of the LDA-MF theory. Due to complications with the numerics we could not identify unambiguously the position of the wetting point of the FMT-MF theory, and we report the position of the prewetting critical point and the upper part of the prewetting line only. In this work both the FMT-MF and LDA-MF theories treat the long-range dispersion attraction in the same way, while differentiating in dealing with the hard-core repulsion. In the study of wetting phenomena one often assumes that, in order to characterize the surface phase behavior of the system, one can focus the analysis on length scales much larger than the molecular size. In such conditions one expects the properties of the solvent to be mainly governed by the long-range attraction. The effect of the short-range repulsion, on the other hand, is supposed to play a minor role only. Our analysis confirms this picture. The qualitative surface phase behavior described by the two

theories does not differentiate appreciably, a part from quantitative discrepancies in the location of the surface phase transitions.

To conclude this section, we finally address Fig. 7.3(c), where the adsorption predicted by the sharp-kink parameterization introduced in Sec. 7.5 is reported. An inspection of the figure shows a striking disagreement with the results of the free minimization of both FMT-MF and LDA-MF theories. In fact, no wetting transition is observed, since the adsorption keeps a finite value for each temperature arbitrarily close to coexistence $\mu_{sat} - \mu = 0$. Therefore, we conclude that the sharp-kink parameterization of the single-particle density as introduced in this chapter appears to be extremely unreliable for the description of the wetting transition. On the other hand, the mechanism behind wetting phenomena is expected to be closely related to that of capillary condensation, which is the main topic of investigation of this chapter. Understanding whether this strong limit of the sharp-kink approach forbids a meaningful description of capillary forces is the aim of the following section.

7.7 Capillary forces between parallel surfaces

We focus in this section on the calculation of the grand potential of a gas at temperature T and chemical potential μ under the effect of the confining potential

$$V_{\text{conf}}(z) = V_w(z) + V_w(d - z), \tag{7.22}$$

where $V_w(z)$ is the solvent-wall potential of Eq. (7.6) and d is the separation between the walls. We compare the predictions of the free minimization of the LDA-MF functional (cf. Eqs. (7.9)-(7.10)) with its sharp-kink (SK) parameterization (cf. Sec. 7.5). Contrarily to the analysis described in the previous section, we will not consider here the FMT-MF theory. There are two reasons behind this choice. First, deviations between the FMT-MF and LDA-MF theories are relevant only at length-scales of the order of the molecular size, as it was shown in Sec. 7.6. Therefore, we do not expect these deviations to play major roles at the length-scales where our attention focuses. Second, the higher complexity of the FMT-MF theory requires an appreciably more demanding numerical effort with respect to the LDA-MF theory.

Let us consider the case of two walls separated by a distance $d \gg \sigma$. If the state of the gas is far enough from saturation, i.e., $\mu \ll \mu_{sat}$, one expects the molecular adsorption on each wall not to deviate appreciably from the case of isolated walls. However, a dramatic change can develop when the two walls are brought close to each other or, alternatively, the state of the gas is moved towards saturation. A minimum distance d^* can exist, below which it is thermodynamically more favorable for the system to fill the space in between the walls with a dense liquid phase [207, 208]. Notice that in the absence of the walls this liquid phase would be metastable with respect to the gas. The phenomenon according to which a metastable phase is stabilized by confining surfaces is named "capillary condensation". A graphic representation of the discontinuous change in the particle distribution associated with such a phase transition is reported for a particular fluid state point in Fig. 7.5.

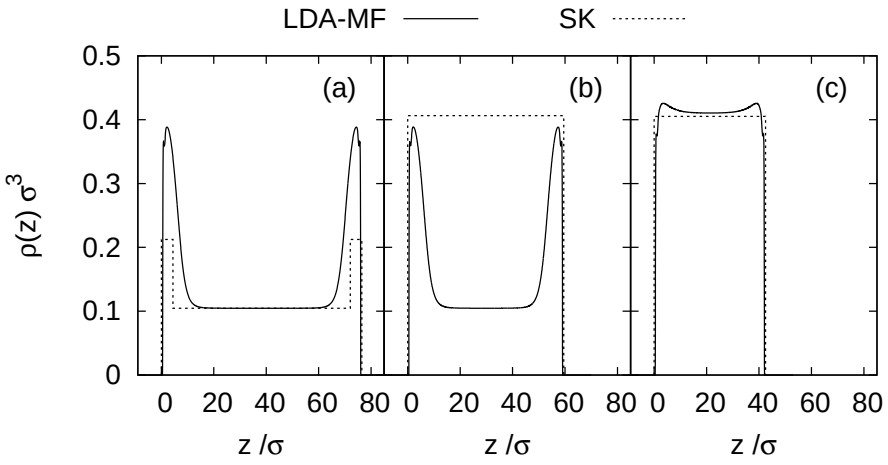

Figure 7.5: Single particle density profile $\rho(z)$ of a fluid with pairwise interactions defined by Eqs. (7.4)-(7.5) under the effect of the external potential $V_w(z)+V_w(d-z)$, where $V_w(z)$ is given by Eq. (7.6). The state of the fluid is characterized by a temperature $k_BT/\epsilon = 1.40$ and a value of the chemical potential corresponding to a bulk density $\rho = 0.95\rho_{sat}$, with ρ_{sat} the gas saturation density. The different pictures correspond to different values of the wall-wall distance: (a) $d/\sigma = 77$, (b) $d/\sigma = 60$ and (a) $d/\sigma = 43$. In each plot the solid curves are obtained via the free minimization of the LDA-MF functional (LDA-MF), whereas the dashed ones are calculated via the sharp-kink parametrization (SK) of the single-particle density for the same functional.

Importantly, the capillary-condensation transition determines a marked change in the functional dependence of the grand potential vs. the distance d between the walls with respect to the non-condensed state. This change, which is accompanied by a discontinuity in the first derivative of the grand potential with respect to d, is related to a sharp change in the solvent-mediated potential, giving rise to so-called "capillary-condensation forces" [207, 208].

In Fig. 7.6 we report calculations for the solvent-mediated potential per unit area $W(d)$ between two walls at a distance d, calculated in terms of the grand potential Ω of the solvent as

$$W(d) = \frac{\Omega(T,V,\mu,d) - \Omega(T,V,\mu,d\to\infty)}{A}, \tag{7.23}$$

where A is the transverse area of the system. The data obtained by means of the free minimization of the LDA-MF functional are displayed on the left column of Fig. 7.6, whereas those relative to the sharp-kink parameterization on the right one. The three values of temperature we choose to investigate are $k_BT/\epsilon = 1.16$ (below the wetting transition temperature, Fig. 7.6(a)-(b)), $k_BT/\epsilon = 1.32$ (above the

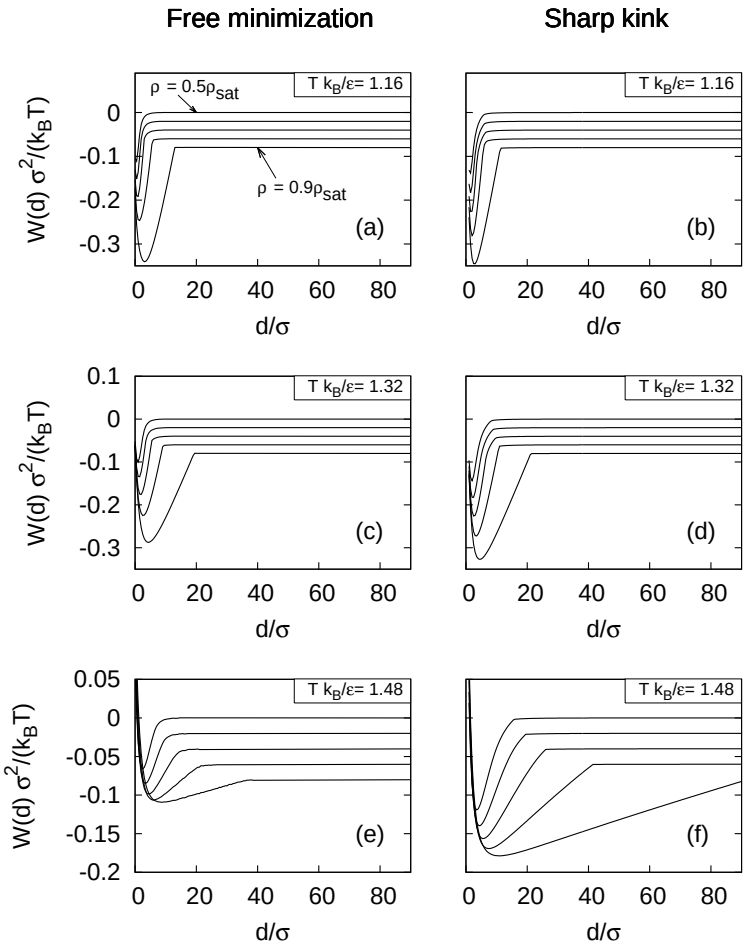

Figure 7.6: Solvent-mediated potential per unit surface $W(d)$ between two parallel walls placed at a distance d. The left figures ((a), (c) and (e)) represent calculations obtained by means of the free minimization of the LDA-MF functional, whereas the right figures ((b), (d) and (f)) are obtained by means of the sharp-kink parameterization of the LDA-MF theory. The data on top ((a)-(b)) correspond to gas state points obtained at temperature $k_BT/\epsilon = 1.16$, those in the middle ((c)-(d)) at $k_BT/\epsilon = 1.32$ and those at the bottom ((e)-(f)) at $k_BT/\epsilon = 1.48$. In each plot each line corresponds to the solvent-mediated potential per unit area (plus a constant to ease the visualization) at different values of the fluid chemical potential. By indicating with ρ_{sat} the density of the gas coexisting with the liquid at temperature T, the values of the gas chemical potential considered correspond to a bulk gas density (from the top to the bottom curve in each plot) $\rho/\rho_{sat} = 0.5, 0.6, 0.7, 0.8, 0.9$.

wetting temperature and below the prewetting critical temperature, Fig. 7.6(c)-(d)) and $k_BT/\epsilon = 1.48$ (above the critical prewetting temperature and just below the fluid critical temperature $k_BT_c/\epsilon = 1.50$, Fig. 7.6(e)-(f)). In each plot we show the solvent-mediated potential at different values of the chemical potential, corresponding to bulk gas densities $\rho/\rho_{sat} = 0.5, 0.6, 0.7, 0.8, 0.9$ and ρ_{sat} is the saturation density of the gas at a given temperature.

Let us start the analysis of the solvent-mediated potential with the numerically exact predictions of the LDA-MF theory (left column of Fig. 7.6). There is a trend in the solvent-mediated potentials that is common to the three values of temperature considered. There is a characteristic wall-to-wall distance d^*, such that when $d < d^*$ the potential develops a markedly attractive well. On the other hand, for $d > d^*$ the potential appears constant on this scale, signaling almost the absence of any force between the walls. Actually, for $d > d^*$ a solvent-mediated force between the walls not observable on this scale is still present as a consequence of the long-range character of both the wall-particle and particle-particle interactions. The attractive well appearing for $d < d^*$ is characterized by a deep minimum, which takes the value of a few tenths of k_BT per unit area σ^2. The minimum is a result of a balance between the attractive capillary condensation force and the short-range repulsion exerted by the walls. With the exception of Fig. 7.6(e), which will be discussed in the following, in each plot the depth of the well increases with the gas density. The range of this sharp attraction is limited to a few molecular diameters for bulk densities below $\rho/\rho_{sat} = 0.8$. When approaching coexistence, however, the range of the solvent-mediated potential considerably increases, reaching values of tens of molecular diameters for gas bulk densities as low as $\rho/\rho_{sat} = 0.9$. By moving our attention on the temperature dependence of the solvent-mediated potential, increasing the temperature has the effect of increasing the range of the potential, while decreasing the depth of the minimum. This seems to show that the higher the temperature, the more easily the capillary condensation transition establishes, i.e., the higher d^*.

Let us now compare the outcome of the free LDA-MF functional minimization with the sharp-kink theory (right column of Fig. 7.6). Globally one finds good overall quantitative agreement between the two methods. At temperature $k_BT/\epsilon = 1.16$ and $k_BT/\epsilon = 1.32$ the solvent-mediated potential is described in an excellent way in its general features, with only minor deviations in the depth of the attractive well. There is a conceptually relevant difference between the results obtained within the two methods. As one can observe in Fig. 7.6(a), (c) and (e), a discontinuity in the first derivative of the grand potential with respect to d is detectable in the case of free minimization only for state points close enough to saturation (curves at the bottom of each plot). Far from saturation (curves at the top of each plot) the attractive well develops continuously in d, manifesting the absence of a phase transition. This does not happen to be the case for the sharp-kink parameterization. In the latter case, as shown in Fig. 7.6(b), (d) and (f), the appearance of the potential well is always accompanied by a discontinuity in d, even for state points far from gas-liquid coexistence. It is reasonable to motivate this disagreement with

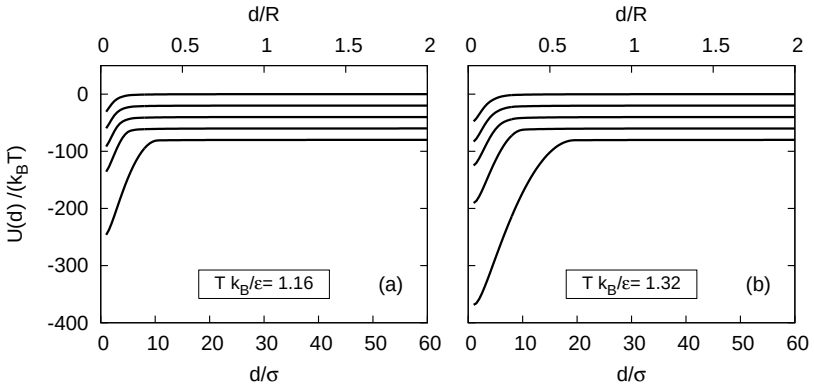

Figure 7.7: Solvent-mediated potential between two spheres of radius $R/\sigma = 30$ as a function of the surface-to-surface distance d. The potentials are deduced from those obtained by the sharp-kink parameterization of the LDA-MF theory for the slit geometry (cf. Fig. 7.6) after application of the Derjaguin approximation. The plots represent the same state points considered in Fig. 7.6)(a)-(d), that is, gas state points at temperature (a) $k_BT/\epsilon = 1.16$ and (b) $k_BT/\epsilon = 1.32$. In each plot the different curves correspond to different values of the gas chemical potential, which takes values corresponding to bulk gas density (from top to bottom) $\rho/\rho_{sat} = 0.5, 0.6, 0.7, 0.8, 0.9$, where ρ_{sat} is the gas saturation density at a given temperature.

the poor parameterization of the density profiles in the sharp-kink approximation, which determines artificial discontinuities in the equilibrium single-particle density. Nevertheless, this fact does not spoil the good agreement between the two methods. However, the situation appears to be less favorable when comparing the results of the two procedures at temperature $k_BT/\epsilon = 1.48$ close to the critical temperature in Fig. 7.6(e)-(f). In this case one can observe a marked disagreement: the sharp-kink approximation appreciably overestimates both the range and the depth of the solvent-mediated potential. This limitation of the sharp-kink approach is clearly due to the poor description of the non capillary- condensed phase, and it is probably related to the absence of a wetting transition, as highlighted in Sec. 7.6. In fact, a sharp-kink profile cannot reproduce a slowly decaying profile (cf. Fig. 7.2), like that governed by the long-range correlations of a fluid in the proximity of criticality. As a result, this approximation strongly overestimates the grand potential of the non capillary-condensed phase, giving rise to an artificially strong and long-range interaction.

Finally, we are interested in estimating the strength of capillary forces in colloidal systems. We calculate the interaction potential between two spherical colloids of radius R immersed in a gas at temperature $k_BT/\epsilon = 1.16$ and $k_BT/\epsilon = 1.32$. In the limit of small surface separation d between the colloids, the colloid-colloid solvent-mediated potential $U(d)$ can be deduced from the potential between two planar

surfaces $W(d)$ by means of the Derjaguin approximation [9],

$$U(d) = \pi R \int_d^\infty dx\, W(x). \tag{7.24}$$

In Fig. 7.7 we report the results of this calculation, deduced from the data obtained by means of the sharp-kink approximation in Fig. 7.6(b) and (d). The radius of the two colloids is chosen to be $R/\sigma = 30$, so that if the fluid is composed by water molecules, for which $\sigma = 0.3\,\mathrm{nm}$, the colloid has a radius $R \simeq 10\,\mathrm{nm}$. The range of the potential coincides with that of Fig. 7.6. However, the most striking element of Fig. 7.7 is the depth of the attraction potential, which takes values of hundreds of $k_B T$. This estimate makes manifest the strong role capillary forces can have on colloidal systems.

7.8 Conclusion

We apply density functional theory to the study of the solvent-mediated interactions between colloids when the solvent is close to a fluid-fluid phase separation. In the presence of preferential adsorption the confinement of the solvent due to the colloids can induce the local stabilization of a phase otherwise metastable. Associated with this capillary condensation transition one expects the emergence of a solvent-induced capillary force between the colloids. Such an effective interaction has the advantage of being adjustable by a simple change in temperature, thus allowing for a reversible control of colloidal aggregation. The microscopic description of these effective interactions starting from first principles has been widely performed in the past. However, its main disadvantage is related to its numerical complexity, which requires a time-consuming functional minimization.

In this chapter we develop a minimalist theory for the microscopic description of capillary forces by means of a reduction of the free parameters of the density functional theory. The approximated theory on which this study is based treats the short-range repulsion between solvent molecules by means of a local-density approximation, while the effect of the van der Waals attraction is introduced by means of a non-local mean-field term (LDA-MF). The reduction of the free parameters of the theory is achieved by imposing the sharp-kink functional form to the local density of the solvent. In the simple planar geometry studied here, this approximation reduces the number of free parameters to only two. We analyze the reliability of such an approach by comparing the predictions of the minimalist theory in the planar geometry with those obtained by means of the free, i.e., numerically exact, minimization of the same functional. Moreover, in order to assess the quality of the LDA-MF functional, we compare its predictions with those of a more refined density functional theory, in which the hard-core repulsion is treated non-locally within the fundamental measure theory (FMT-MF).

As a preliminary analysis we study the adsorption of the fluid on an attractive wall. We show that the outcome of the freely-minimized LDA-MF and FMT-MF

theories are qualitatively the same, and are characterized by a first-order wetting transition. Deviations between their results only involve the position of the surface phase transitions on the phase diagram. This proves the limited role of the excluded-volume repulsion in determining the wetting behavior of the fluid. On the other hand, we show that the sharp-kink approximation strongly affects the surface phase behavior of the fluid by suppressing the wetting transition.

The poor description of the fluid adsorption by the sharp-kink parameterization does not however manifest so dramatically in the predictions of the solvent-mediated potential between two planar surfaces. In fact, the capillary-condensed state appears to be very well reproduced by the sharp-kink approximation. As a result, we observe very good quantitative agreement with the predictions of the freely minimized theory. On the other hand, important deviations between the two theories appear in the description of the non-capillary-condensed phase. This fact is due to the inability of the sharp-kink approximation to account for slowly decaying density profiles. The negative effect of such deviations on the description of the solvent-mediated potential becomes evident in proximity of the critical temperature.

In conclusion, we show in this chapter that a sharp-kink parameterization can offer a simple and reliable way to predict solvent-induced interactions in the planar geometry. It would be even more interesting to apply such a method to more complex geometries, where the free minimization of the theory is much more challenging. For example, it could be interesting to study the many-body character of these interactions by calculating the three-body interaction term. Additionally, it would be appealing to apply such a theory in combination with a molecular-dynamics algorithm, thus following an approach similar in spirit to the Car-Parrinello method for ion-electron systems [222] and its classical version for charged colloids [223]. Within this *ab-initio* approach the colloids, modeled as spheres, move in space and interact through an effective potential which is calculated by solving the theory at each configuration. We believe that the theory introduced in this chapter, due to its limited number of free parameters, would offer the simplest method to observe in a simulation this type of solvent-induced colloidal aggregation.

7.A Appendix

In this appendix we report the explicit expression for the coefficients $a(\mathcal{A})$ and $b(\mathcal{A},\mathcal{B})$ (cf. Eqs. (7.19)-(7.20)) for the two planar geometries analyzed in Sec. 7.6 and 7.7. The attractive component of the interparticle potential is given by Eq. (7.5), whereas the external potential exerted by the single wall is a slight variation of Eq. (7.6) introduced for convenience, namely

$$V_w(z) = \begin{cases} \infty & \text{if } z < 0, \\ 4\epsilon_w \left[\frac{2}{15} \left(\frac{\sigma_w}{z+\sigma_w} \right)^9 - \left(\frac{\sigma_w}{z+\sigma_w} \right)^3 \right] & \text{if } z \geq 0. \end{cases} \tag{7.25}$$

In the following we indicate with $\mathcal{S}$ the two-dimensional surface of each wall, whose area $A \to \infty$ in the thermodynamic limit.

7.A.1 Single-wall configuration (1w)

In this configuration we parameterize the wetting region as $\mathcal{W} = [0,l] \times \mathcal{S}$ and its complementary with respect to the region of space accessible to the fluid is $\overline{\mathcal{W}} = [l,\infty] \times \mathcal{S}$. Notice that the thickness of the adsorption layer l is, with ρ_w, the only free parameter of the grand potential Eq. (7.16). The explicit evaluation of the integrals leads to

$$\frac{a(\mathcal{W})}{A} = \frac{a_{1w}(l)}{A} = \epsilon_w \sigma_w \left[\frac{2\sigma_w^2}{(l+\sigma_w)^2} - \frac{\sigma_w^8}{15(l+\sigma_w)^8} - \frac{29}{15} \right], \tag{7.26}$$

$$\frac{b(\mathcal{W},\mathcal{W})}{A} = \frac{b_{1w}(l)}{A} = \begin{cases} -2\pi\epsilon\sigma^2 l^2 & \text{if } l < \sigma, \\ -\frac{2\pi\epsilon\sigma^4}{3} \left[\frac{8l}{\sigma} + \frac{\sigma^2}{l^2} - 6 \right] & \text{if } l \geq \sigma, \end{cases} \tag{7.27}$$

$$\frac{b(\mathcal{W},\overline{\mathcal{W}})}{A} = \begin{cases} -2\pi\epsilon\sigma^4 \left[\frac{4l}{3\sigma} - \frac{l^2}{2\sigma^2} \right] & \text{if } l < \sigma, \\ -2\pi\epsilon\sigma^4 \left[1 - \frac{\sigma^2}{6l^2} \right] & \text{if } l \geq \sigma. \end{cases} \tag{7.28}$$

Notice than in this case the terms $a(\overline{\mathcal{W}})$ and $b(\overline{\mathcal{W}},\overline{\mathcal{W}})$ can be dropped from Eq. (7.16) by subtracting the bulk grand potential to it.

7.A.2 Double-wall configuration (2w)

We consider here the case of the solvent confined by the external potential $V_w(z) + V_w(d-z)$. For the evaluation of the coefficients $a(\mathcal{A})$ and $b(\mathcal{A},\mathcal{B})$ we must consider separately the two situations of capillary-condensed and non capillary-condensed phase.

Non capillary-condensed phase

We parameterize the wetting region as $\mathcal{W} = \mathcal{W}_1 \cup \mathcal{W}_2$, where $\mathcal{W}_1 = [0, l] \times \mathcal{S}$, $\mathcal{W}_2 = [d - l, d] \times \mathcal{S}$ and consequently $\overline{\mathcal{W}} = [l, d - l] \times \mathcal{S}$. Here it is implicitly assumed that $l < d/2$, otherwise one has a capillary-condensed state. The evaluation of the integrals Eq. (7.19) gives

$$\frac{a(\mathcal{W})}{A} = 2\frac{a_{1w}(l)}{A} + 2\epsilon_w\sigma_w\left[\frac{\sigma_w^8}{15}\left((d-l+\sigma_w)^{-8} - (d+\sigma_w)^{-8}\right) - \right.$$
$$\left. - 2\sigma_w^2\left((d-l+\sigma_w)^{-2} - (d+\sigma_w)^{-2}\right)\right], \quad (7.29)$$

where $a_{1w}(l)$ is defined in Eq. (7.26), and

$$\frac{a(\overline{\mathcal{W}})}{A} = 2\epsilon_w\sigma_w\left[\frac{\sigma_w^8}{15}\left((l+\sigma_w)^{-8} - (d-l+\sigma_w)^{-8}\right) - \right.$$
$$\left. - 2\sigma_w^2\left((l+\sigma_w)^{-2} - (d-l+\sigma_w)^{-2}\right)\right]. \quad (7.30)$$

The integrals of the type of Eq. (7.20) are

$$\frac{b(\mathcal{W}, \mathcal{W})}{A} = 2\frac{b_{1w}(l)}{A} + \frac{b_{2w}(l,d)}{A}, \quad (7.31)$$

where $b_{1w}(l)$ is given in Eq. (7.27) and the function $b_{2w}(l,d)$ is defined as follows

$$\frac{b_{2w}(l,d)}{A} = -\frac{\pi\epsilon\sigma^4}{3}\begin{cases} \frac{\sigma^2}{(d-2l)^2} - \frac{2\sigma^2}{(d-l)^2} + \frac{\sigma^2}{d^2} & \text{if } l < \frac{d-\sigma}{2} \wedge d > \sigma, \\ \frac{3(d-2l)^2}{\sigma^2} - \frac{8(d-2l)}{\sigma} - \frac{2\sigma^2}{(d-l)^2} + \frac{\sigma^2}{d^2} + 6 & \text{if } \frac{d-\sigma}{2} < l < d-\sigma \wedge d > \sigma, \\ \frac{6l^2}{\sigma^2} - \frac{3d^2}{\sigma^2} + \frac{8d}{\sigma} + \frac{\sigma^2}{d^2} - 6 & \text{if } l > d-\sigma \wedge d > \sigma, \\ \frac{6l^2}{\sigma^2} & \text{if } d < \sigma, \end{cases} \quad (7.32)$$

$$\frac{b(\mathcal{W}, \overline{\mathcal{W}})}{A} = \begin{cases} \frac{b_{2w}^{(-)}(l,d)}{A} & \text{if } l < \frac{d}{3}, \\ \frac{b_{2w}^{(+)}(l,d)}{A} & \text{if } l > \frac{d}{3}, \end{cases} \quad (7.33)$$

with the functions $b_{2w}^{(-)}(l,d)$ and $b_{2w}^{(+)}(l,d)$ given by

$$\frac{b_{2w}^{(-)}(l,d)}{A} = -\frac{\pi\epsilon\sigma^4}{3}\begin{cases} -\frac{\sigma^2}{(d-2l)^2} + \frac{\sigma^2}{(d-l)^2} - \frac{\sigma^2}{l^2} + 6 & \text{if } l > \sigma, \\ \frac{\sigma^2}{(d-l)^2} - \frac{\sigma^2}{(d-2l)^2} - \frac{3l^2}{\sigma^2} + 8\frac{l}{\sigma} & \text{if } l < \sigma \wedge l < \frac{d-\sigma}{2}, \\ \frac{\sigma^2}{(d-l)^2} + \frac{12dl-3d^2-15l^2}{\sigma^2} + \frac{8d-8l}{\sigma} - 6 & \text{if } \frac{d-\sigma}{2} < l < d-\sigma, \\ \frac{6ld-2l^2}{\sigma^2} & \text{if } d-\sigma < l < \sigma, \end{cases} \tag{7.34}$$

and

$$\frac{b_{2w}^{(+)}(l,d)}{A} = -\frac{\pi\epsilon\sigma^4}{3}\begin{cases} -\frac{\sigma^2}{(d-2l)^2} + \frac{\sigma^2}{(d-l)^2} - \frac{\sigma^2}{l^2} + 6 & \text{if } l < \frac{d-\sigma}{2}, \\ \frac{8(d-2l)}{\sigma} - \frac{d\sigma^2(d-2l)}{l^2(d-l)^2} - \frac{3(d-2l)^2}{\sigma^2} & \text{if } l > \sigma \wedge l > \frac{d-\sigma}{2}, \\ \frac{\sigma^2}{(d-l)^2} + \frac{12dl-3d^2-15l^2}{\sigma^2} + \frac{8d-8l}{\sigma} - 6 & \text{if } l > d-\sigma, \\ \frac{6ld-2l^2}{\sigma^2} & \text{if } d-\sigma < l < \sigma, \end{cases} \tag{7.35}$$

and finally

$$\frac{b(\overline{\mathcal{W}},\overline{\mathcal{W}})}{A} = \frac{b_{1w}(d-2l)}{A}. \tag{7.36}$$

Capillary-condensed phase

In this situation the domain accessible to the fluid coincides with the wetting region, therefore $\mathcal{W} = [0,d]\times\mathcal{S}$ and the only free parameter of the theory is ρ_w. In this case the coefficients in Eq. (7.16) can be related to those obtained for the single-wall configuration as

$$\frac{a(\mathcal{W})}{A} = 2\frac{a_{1w}(d)}{A}, \tag{7.37}$$

$$\frac{b(\mathcal{W},\mathcal{W})}{A} = \frac{b_{1w}(d)}{A}, \tag{7.38}$$

and $a(\overline{\mathcal{W}}) = b(\mathcal{W},\overline{\mathcal{W}}) = b(\overline{\mathcal{W}},\overline{\mathcal{W}}) = 0$.

Bibliography

[1] R.J. Hunter, *Foundations of Colloid Science*, Oxford University Press, 2nd ed., 2001.
[2] D.H. Everett, *Basic Principles of Colloid Science*, Royal Society of Chemistry, 1988.
[3] J.K.G. Dhont, *An Introduction to Dynamics of Colloids*, Elsevier, 1996.
[4] *IUPAC Compendium of Chemical Terminology (http://goldbook.iupac.org)*.
[5] T. Graham, *Phil. Trans. R. Soc. Lond.* **151**, 183 (1861).
[6] A. Einstein, *Ann. Phys. (Leipz.)* **17**, 549 (1905).
[7] W. Sutherland, *Phil. Mag.* **9**, 781 (1905).
[8] P. Langevin, *C. R. Acad. Sci. (Paris)* **146**, 530 (1908).
[9] J.N. Israelachvili, *Intermolecular and Surface Forces*, Academic Press, 3rd ed., 2011.
[10] R. Brown, *Phil. Mag.* **4**, 161 (1828).
[11] J.B. Perrin, *Ann. Chim. Phys.* **18**, 5 (2012).
[12] L.D. Landau and E.M. Lifshitz, *Statistical Physics: Part 1*, Elsevier, 3rd ed., 1980.
[13] H.B. Callen, *Thermodynamics and an Introduction to Thermostatistics*, John Wiley and Sons, 2nd ed., 1985.
[14] D.A. McQuarrie, *Statistical Mechanics*, University Science Books, 2000.
[15] J.E. Lay, *Statistical Mechanics and Thermodynamics of Matter*, Harper and Row Publishers, 1990.
[16] J.P. Hansen and I.R. McDonald, *Theory of Simple Liquids*, Academic Press, 3rd ed., 2006.
[17] P.G. de Gennes and J. Prost, *The Physics of Liquid Crystals*, Clarendon, Oxford, 2nd ed., 1993.
[18] P.J. Collings, *Liquid crystals: Nature's delicate phase of matter*, Princeton University Press, 2002.
[19] H. Goldstein, *Classical Mechanics*, Addison-Wesley, 2nd ed., 1980.
[20] M.P. Allen, G.T. Evans, D. Frenkel, and B.M. Mulder, *Adv. Chem. Phys.* **86**, 1 (1993).
[21] R. Evans, *Adv. Phys.* **28**, 143 (1979).
[22] R.F. Kayser and H.J. Raveché, *Phys. Rev. A* **17**, 2067 (1978).
[23] B. Mulder, *Phys. Rev. A* **35**, 3095 (1987).
[24] L. Onsager, *Ann. N. Y. Acad. Sci.* **51**, 627 (1949).
[25] G. Parisi, *Statistical Field Theory*, Addison Wesley, 1988.
[26] Y. Rosenfeld, *Phys. Rev. Lett.* **63**, 980 (1989).
[27] Y. Rosenfeld, M. Schmidt, H. Löwen, and P. Tarazona, *Phys. Rev. E* **55**, 4245 (1997).
[28] P. Tarazona, J. Cuesta, and Y. Martínez-Ratón, in *Theory and Simulation of Hard-Sphere Fluids and Related Systems*, Springer, Berlin/Heidelberg, 2008.
[29] R. Roth, *J. Phys.: Condens. Matter* **18**, 8413 (2010).
[30] N. Metropolis, A.W. Rosenbluth, M.N. Rosenbluth, A.N. Teller, and

E. TELLER, *J. Chem. Phys.* **21**, 1087 (1953).
[31] D. FRENKEL and B. SMIT, *Understanding Molecular Simulations: From Algorithms to Applications*, Academic Press, San Diego, 2nd ed., 2001.
[32] M.J. FREISER, *Phys. Rev. Lett.* **24**, 1041 (1970).
[33] R. ALBEN, *Phys. Rev. Lett.* **30**, 778 (1973).
[34] J.P. STRALEY, *Phys. Rev. Lett.* **10**, 1881 (1974).
[35] C. TSCHIERSKE and D.J. PHOTINOS, *J. Mater. Chem.* **20**, 4263 (2010).
[36] R. BERARDI, L. MUCCIOLI, S. ORLANDI, M. RICCI, and C. ZANNONI, *J. Phys.: Condens. Matter* **20**, 463101 (2008).
[37] R. BERARDI, L. MUCCIOLI, and C. ZANNONI, *J. Chem. Phys.* **128**, 024905 (2008).
[38] G.R. LUCKHURST, *Nature* **430**, 413 (2004).
[39] L. J. YU and A. SAUPE, *Phys. Rev. Lett.* **45**, 1000 (1980).
[40] L.A. MADSEN, T.J. DINGEMANS, M. NAKATA, and E.T. SAMULSKI, *Phys. Rev. Lett.* **92**, 145505 (2004).
[41] B.R. ACHARYA, A. PRIMAK, and S. KUMAR, *Phys. Rev. Lett.* **92**, 145506 (2004).
[42] M.P. TAYLOR and J. HERZFELD, *Phys. Rev. A* **44**, 3742 (1991).
[43] R. VAN ROIJ and B. MULDER, *J. Phys. (France) II* **4**, 1763 (1994).
[44] F.M. VAN DER KOOIJ and H.N.W. LEKKERKERKER, *Phys. Rev. Lett.* **84**, 781 (2000).
[45] E. VAN DEN POL, A.V. PETUKHOV, D.M.E. THIES-WEESIE, D.V. BYELOV, and G.J. VROEGE, *Phys. Rev. Lett.* **103**, 258301 (2009).
[46] G.J. VROEGE and H.N.W. LEKKERKERKER, *J. Phys. Chem.* **97**, 3601 (1993).
[47] B. MULDER, *Phys. Rev. A* **39**, 360 (1989).
[48] A.G. VANAKARAS, M.A. BATES, and D.J. PHOTINOS, *Phys. Chem. Chem. Phys.* **5**, 3700 (2003).
[49] P.J. CAMP and M.P. ALLEN, *J. Chem. Phys.* **106**, 6681 (1997).
[50] R. ZWANZIG, *J. Chem. Phys.* **39**, 1714 (1963).
[51] R. VAN ROIJ, M. DIJKSTRA, and R. EVANS, *Europhys. Lett.* **43**, 350 (2000).
[52] Y. MARTÍNEZ-RATÓN, S. VARGA, and E. VELASCO, *Phys. Chem. Chem. Phys.* **13**, 13247 (2011).
[53] P. SOLLICH and M.E. CATES, *Phys. Rev. Lett.* **80**, 1365 (1998).
[54] P.B. WARREN, *Phys. Rev. Lett.* **80**, 1369 (1998).
[55] N. CLARKE, J. CUESTA, R. SEAR, P. SOLLICH, and A. SPERANZA, *J. Chem. Phys.* **113**, 5817 (2000).
[56] D. FRENKEL, *J. Phys. Chem.* **92**, 3280 (1988).
[57] N. BOCCARA, R. MEJDANI, and L. DE SEZE, *J. Phys.* **38**, 149 (1977).
[58] Y. MARTÍNEZ-RATÓN and J.A. CUESTA, *Phys. Rev. Lett.* **89**, 185701 (2002).
[59] S. VARGA, A. GALINDO, and G. JACKSON, *Phys. Rev. E* **66**, 011707 (2002).
[60] G. DE MATTEIS, S. ROMANO, and E.G. VIRGA, *Phys. Rev. E* **72**, 041706 (2005).
[61] L. LONGA, G. PAJAK, and T. WYDRO, *Phys. Rev. E* **76**, 011703 (2007).
[62] D. ALLENDER and L. LONGA, *Phys. Rev. E* **78**, 011704 (2008).
[63] M.P. ALLEN, *Liq. Cryst.* **8**, 449 (1990).
[64] R. BERARDI and C. ZANNONI, *Mol. Cryst. Liq. Cryst.* **396**, 177 (2003).
[65] M.A. BATES and G.R. LUCKHURST, *Phys. Rev. E* **72**, 051702 (2005).
[66] M.A. BATES, *Chem. Phys. Lett.* **437**, 189 (2007).

[67] A. Cuetos and B. Martinez-Haya, *J. Chem. Phys.* **129**, 214706 (2008).
[68] J.L. Barrat and J.P. Hansen, *J. Phys. (Paris)* **47**, 1547 (1986).
[69] R. McRae and A.D. Haymet, *J. Chem. Phys.* **88**, 1114 (1988).
[70] M.A. Bates and D. Frenkel, *J. Chem. Phys.* **109**, 6193 (1998).
[71] S. Asakura and F. Oosawa, *J. Chem. Phys.* **22**, 1255 (1954).
[72] A. Vrij, *Pure and Appl. Chem.* **48**, 471 (1976).
[73] R. Tuninier and H.N.W. Lekkerkerker, *Colloids and the Depletion Interaction*, Springer, 2011.
[74] T. Odijk, *Biophys. Chem.* **73**, 4635 (1998).
[75] R. Piazza, *Curr. Opinion Colloid Interface Sci.* **5**, 38 (2000).
[76] G. Odriozola, F. Jiméenez-Ángeles, and M. Lozada-Cassou, *J. Chem. Phys.* **129**, 111101 (2008).
[77] S. Sacanna, W.T.M. Irvine, P.M. Chaikin, and D.J. Pine, *Nature* **464**, 575 (2010).
[78] A. Gast, W.B. Russel, and C.K. Hall, *J. Colloid Interface Sci.* **109**, 161 (1986).
[79] S. Auer and D. Frenkel, *Nature* **409**, 1020 (2001).
[80] V.J. Anderson and H.N.W. Lekkerkerker, *nature* **416**, 811 (2002).
[81] E. Weeks, J.C. Crocker, A.C. Levitt, A. Schofield, and D.A. Weitz, *Science* **287**, 627 (2000).
[82] H.N.W. Lekkerkerker and A. Stroobants, *Nuovo Cimento D* **16**, 949 (1994).
[83] J. Buitenhuis, L.N. Donselaar, P.A. Buining, A. Stroobants, and H.N.W. Lekkerkerker, *J. Colloid Interface Sci.* **175**, 46 (1995).
[84] P. Bolhuis and D. Frenkel, *J. Chem. Phys.* **106**, 666 (1997).
[85] Z. Dogic, K.R. Purdy, E. Grelet, M. Adams, and S. Fraden, *Phys. Rev. E* **69**, 051702 (2004).
[86] S.V. Savenko and M. Dijkstra, *J. Chem. Phys.* **124**, 234902 (2006).
[87] S. Jungblut, R. Tuinier, K. Binder, and T. Schilling, *J. Chem. Phys.* **127**, 244909 (2007).
[88] M.A. Bates and D. Frenkel, *Phys. Rev. E* **62**, 5225 (2000).
[89] F.M. van der Kooij, M. Vogel, and H.N.W. Lekkerkerker, *Phys. Rev. E* **62**, 5397 (2000).
[90] S.D. Zhang, P.A. Reynolds, and J.S. van Duijneveldt, *J. Chem. Phys.* **117**, 9947 (2002).
[91] D. Kleshchanok et al., *Soft Matter* **8**, 191 (2012).
[92] M. Dijkstra, R. van Roij, and R. Evans, *Phys. Rev. E* **59**, 5744 (1999).
[93] M. Dijkstra, J.M. Brader, and R. Evans, *J. Phys.: Condens. Matter* **11**, 10079 (1999).
[94] B. Götzelmann, R. Evans, and S. Dietrich, *Phys. Rev. E* **57**, 6785 (1998).
[95] W.W. Wood and J.D. Jacobson, *J. Chem. Phys.* **27**, 1207 (1957).
[96] B.J. Alder and T.E. Wainwright, *J. Chem. Phys.* **27**, 1208 (1957).
[97] R.W. Zwanzig, *J. Chem. Phys.* **24**, 855 (1956).
[98] W.G. Hoover and A.G. Rocco, *J. Chem. Phys.* **34**, 1059 (1961).
[99] W.G. Hoover and A.G. Rocco, *J. Chem. Phys.* **36**, 3141 (1962).
[100] A.L. Beyerlein, W.G. Rudd, Z.W. Salsburg, and M. Buynoski, *J. Chem. Phys.* **53**, 1532 (1970).

[101] W.G. RUDD and H.L. FRISCH, *J. Comp. Phys.* **7**, 394 (1971).
[102] C. CARLIER and H.L. FRISCH, *Phys. Rev. A* **6**, 1153 (1972).
[103] F.H. REE and T. REE, *J. Chem. Phys.* **56**, 5434 (1972).
[104] H.L. FRISCH et al., *Phys. Rev. A* **22**, 740 (1980).
[105] W.G. HOOVER, C.G. HOOVER, and M.N. BANNERMAN, *J. Stat. Phys.* **136**, 715 (2009).
[106] A. BEYERLEIN, *J. Comp. Phys.* **7**, 403 (1971).
[107] E.A. JAGLA, *Phys. Rev. E* **58**, 4701 (1998).
[108] B. GROH and B. MULDER, *J. Chem. Phys.* **114**, 3653 (2001).
[109] M. DIJKTRA and D. FRENKEL, *Phys. Rev. Lett.* **72**, 298 (1994).
[110] M. DIJKSTRA, D. FRENKEL, and J.P. HANSEN, *J. Chem. Phys.* **101**, 3179 (1994).
[111] J.A. CUESTA and Y. MARTÍNEZ-RATÓN, *J. Chem. Phys.* **107**, 6379 (1997).
[112] Y. MARTÍNEZ-RATÓN and J.A. CUESTA, *J. Chem. Phys.* **111**, 317 (1999).
[113] L. ROSSI, S. SACANNA, W.T.M. IRVINE, P.M. CHAIKIN, D.J. PINE, and A.P. PHILIPSE, *Soft Matter* **7**, 4139 (2011).
[114] K. ZHAO, R. BRUINSMA, and T.G. MASON, *Proc. Natl. Acad. Sci. U.S.A.* **108**, 2684 (2011).
[115] F. SMALLENBURG, L. FILION, M. MARECHAL, and M. DIJKSTRA, *Proc. Natl. Acad. Sci. U.S.A.* **109**, 17886 (2012).
[116] X. ZHANG, Z. ZHANG, and S.C. GLOTZER, *J. Phys. Chem. C* **111**, 4132 (2007).
[117] R.D. BATTEN, F.H. STILLINGER, and S. TORQUATO, *Phys. Rev. E* **81**, 061105 (2010).
[118] C. A. NO and F.A. ESCOBEDO, *Soft Matter* **8**, 4675 (2012).
[119] R. NI, A.P. GANTAPARA, J. DE GRAAF, R. VAN ROIJ, and M. DIJKSTRA, *Soft Matter* **8**, 8826 (2012).
[120] M. MARECHAL, U. ZIMMERMANN, and H. LÖWEN, *J. Chem. Phys.* **136**, 144506 (2012).
[121] H. HANSEN-GOOS and K. MECKE, *Phys. Rev. Lett.* **102**, 018302 (2009).
[122] H. HANSEN-GOOS and K. MECKE, *J. Phys.: Condens. Matter* **22**, 364107 (2010).
[123] P. TARAZONA, *Mol. Phys.* **52**, 81 (1984).
[124] R. ROTH, R. EVANS, A. LANG, and G. KAHL, *J. Phys.: Condens. Matter* **14**, 12063 (2002).
[125] B.B. LAIRD, J.D. MCCOY, and A.D.J. HAYMET, *J. Chem. Phys.* **87**, 5449 (1987).
[126] R. OHNESORGE, H. LÖWEN, and H. WAGNER, *Europhys. Lett.* **22**, 245 (1993).
[127] M. OETTEL, S. GÖRIG, A. HÄRTEL, H. LÖWEN, M. RADU, and T. SCHILLING, *Phys. Rev. E* **82**, 051404 (2010).
[128] R. ROTH, K. MECKE, and M. OETTEL, *J. Chem. Phys.* **136**, 081101 (2012).
[129] WWW.FFTW.ORG.
[130] W.H. PRESS, S.A. TEUKOLSKY, W.T. VETTERLING, and B.P. FLANNERY, *Numerical Recipes in Fortran 77: The Art of Scientific Computing*, Cambridge University Press, 2nd ed., 1992.
[131] R.E. PEIERLS, *Annales de l'Institut Henri Poincaré* **5**, 177 (1935).
[132] L.D. LANDAU, *Phys. Z. Sowjet Union* **2**, 26 (1937).
[133] N.D. MERMIN and H. WAGNER, *Phys. Rev. Lett.* **17**, 1133 (1966).

[134] J.T. Toner and D.R. Nelson, *Phys. Rev. B* **23**, 316 (1981).
[135] K.W. Wojciechowski and D. Frenkel, *Comput. Methods Sci. Technol.* **10**, 235 (2004).
[136] P. Tarazona, *Phys. Rev. Lett.* **84**, 694 (2000).
[137] P. Tarazona, *Physica A* **306**, 243 (2002).
[138] A. Parola and L. Reatto, *Phys. Rev. Lett.* **53**, 2417 (1984).
[139] J.N. Israelachvili and B.W. Ninham, *J. Colloid Interface Sci.* **58**, 14 (1977).
[140] P.A. Forsyth, S. Marcelia, D.J. Mitchell, and B.W. Ninham, *Adv. Colloid Interface Sci.* **9**, 37 (1978).
[141] P.J. Flory, *Macromolecules* **11**, 1138 (1978).
[142] D. Frenkel, H. N. W. Lekkerkerker, and A. Stroobants, *Nature* **332**, 822 (1998).
[143] A. Stroobants, H.N.W. Lekkerkerker, and D. Frenkel, *Phys. Rev. Lett.* **57**, 1452 (1986).
[144] A. Stroobants, H.N.W. Lekkerkerker, , and D. Frenkel, *Phys. Rev. A* **36**, 2929 (1987).
[145] J.A.C. Veerman and D. Frenkel, *Phys. Rev. A* **43**, 4334 (1991).
[146] A. Stroobants, *Phys. Rev. Lett.* **69**, 2388 (1992).
[147] S.M. Cui and Z.Y. Chen, *Phys. Rev. E* **50**, 3747 (1994).
[148] Y. Martínez-Ratón, E. Velasco, and L. Mederos, *J. Chem. Phys.* **123**, 104906 (2005).
[149] S. Varga, E. Velasco, L. Mederos, and F.J. Vesely, *Mol. Phys.* **107**, 2481 (2009).
[150] D. Frenkel, *Liquid Crystals* **5**, 929 (1989).
[151] J.A.C. Veerman and D. Frenkel, *Phys. Rev. A* **45**, 5632 (1992).
[152] L. Filion, M. Marechal, B. van Oorschot, D. Pelt, F. Smallenburg, and M. Dijkstra, *Phys. Rev. Lett.* **103**, 188302 (2009).
[153] A.M. Bohle, R. Holyst, and T. Vilgis, *Phys. Rev. Lett.* **76**, 1396 (1996).
[154] H.H. Wensink, *J. Chem. Phys.* **126**, 194901 (2007).
[155] R. Hentschke and J. Herzfeld, *Phys. Rev. A* **44**, 1148 (1991).
[156] R.P. Sear, *Phys. Rev. E* **55**, 5820 (1997).
[157] G. Cinacchi and L. De Gaetani, *Phys. Rev. E* **77**, 051707 (2008).
[158] E. Grelet, *Phys. Rev. Lett.* **100**, 168301 (2008).
[159] S. Hess, D. Frenkel, and M.P. Allen, *Mol. Phys.* **74**, 765 (1991).
[160] H. Löwen, *Phys. Rev. E* **59**, 1989 (1999).
[161] M.A. Bates and G.R. Luckhurst, *J. Chem. Phys.* **120**, 394 (2004).
[162] M. Cifelli, G. Cinacchi, and L. De Gaetani, *J. Chem. Phys.* **125**, 164912 (2006).
[163] Z. Bu, P.S. Russo, D.L. Tipton, and I.I. Negulescu, *Macromolecules* **27**, 6871 (1994).
[164] M.P.B. van Bruggen, H.N.W. Lekkerkerker, and J.K.G. Dhont, *Phys. Rev. E* **56**, 4394 (1997).
[165] M.P.B. van Bruggen, H.N.W. Lekkerkerker, G. Maret, and J.K.G. Dhont, *Phys. Rev. E* **58**, 7668 (1998).
[166] R.C. Cush and P.S. Russo, *Macromolecules* **23**, 8659 (2002).

[167] M.P. LETTINGA, E. BARRY, and Z. DOGIC, *Europhys. Lett.* **71**, 692 (2005).
[168] M.P. LETTINGA and E. GRELET, *Phys. Rev. Lett.* **99**, 197802 (2007).
[169] W. KOB, C. DONATI, S. PLIMPTON, P.H. POOLE, and S.C. GLOTZER, *Phys. Rev. Lett.* **79**, 2827 (1997).
[170] A. GRAY-WEALE and P.A. MADDEN, *J. Phys. Chem. B* **108**, 6624 (2004).
[171] A.M. PUERTAS, M. FUCHS, and M.E. CATES, *J. Chem. Phys.* **121**, 2813 (2004).
[172] Y. GAO and M.L. KILFOIL, *Phys. Rev. E* **79**, 051406 (2009).
[173] M. BIER, R. VAN ROIJ, M. DIJKSTRA, and P. VAN DER SCHOOT, *Phys. Rev. Lett.* **101**, 215901 (2008).
[174] E. GRELET, M.P. LETTINGA, M. BIER, R. VAN ROIJ, and P. VAN DER SCHOOT, *J. Phys.: Condens. Matter* **20**, 494213 (2008).
[175] R. MATENA, A. PATTI, and M. DIJKSTRA, *Phys. Rev. E* **81**, 021704 (2010).
[176] A. PATTI, D. EL MASRI, R. VAN ROIJ, and M. DIJKSTRA, *J. Chem. Phys.* **132**, 224907 (2010).
[177] A. PATTI, D. EL MASRI, R. VAN ROIJ, and M. DIJKSTRA, *Phys. Rev. Lett.* **103**, 248304 (2009).
[178] E. POUGET, E. GRELET, and M.P. LETTINGA, (2009), private communication.
[179] A. PATTI and A. CUEOTS, *Phys. Rev. E* **86**, 011403 (2012).
[180] V. PRYAMITSYN and V. GANESAN, *J. Chem. Phys.* **128**, 134901 (2008).
[181] E. SANZ and D. MARENDUZZO, *J. Chem. Phys.* **132**, 194102 (2010).
[182] M.M. TIRADO and G.C. DE LA TORRE, *J. Chem. Phys.* **71**, 2581 (1979).
[183] M.M. TIRADO and G.C. DE LA TORRE, *J. Chem. Phys.* **81**, 2047 (1984).
[184] L. VAN HOVE, *Phys. Rev.* **95**, 249 (1954).
[185] A. RAHMAN, *Phys. Rev.* **136**, A405 (1964).
[186] B. DOLIWA and A. HEUER, *J. Phys.: Condens. Matter* **11**, A277 (1999).
[187] W.K. KEGEL and A. VAN BLAADEREN, *Science* **287**, 5451 (2000).
[188] E.R. WEEKS and D.A. WEITZ, *Chem. Phys.* **284**, 361 (2002).
[189] L. BERTHIER and W. KOB, *J. Phys.: Condens. Matter* **19**, 205130 (2007).
[190] S. NADERI and P. VAN DER SCHOOT, (2012), private communication.
[191] B.V. DERJAGUIN and L.D. LANDAU, *Acta Physico Chemica URSS* **14**, 633 (1941).
[192] E.J.W. VERWEY and J.T.G. OVERBEEK, *Theory of the stability of lyophobic colloids*, Elsevier, Amsterdam, 1948.
[193] D. BEYSENS and D. ESTÈVE, *Phys. Rev. Lett.* **54**, 2123 (1985).
[194] D. BEYSENS and T. NARAYANAN, *J. Stat. Phys.* **95**, 997 (1999).
[195] T. SLUCKIN, *Phys. Rev. A* **41**, 960 (1990).
[196] B.M. LAW, J.M. PETIT, and D. BEYSENS, *Phys. Rev. E* **57**, 5782 (1998).
[197] H.T. DOBBS, G.A. DARBELLAY, and J.M. YEOMANS, *Europhys. Lett.* **18**, 439 (1992).
[198] H.T. DOBBS and J.M. YEOMANS, *J. Phys. Condens. Matter* **4**, 10133 (1992).
[199] C. HERTLEIN, L. HELDEN, A. GAMBASSI, S. DIETRICH, and C. BECHINGER, *Nature* **451**, 172 (2008).
[200] D. BONN, J. OTWINOWSKI, S. SACANNA, H. GUO, G. WEGDAM, and P. SCHALL, *Phys. Rev. Lett.* **103**, 156101 (2009).
[201] M.E. FISHER and P.G. DE GENNES, *Acad. Sci. (Paris) Ser. B* **287**, 207 (1978).
[202] M. KRECH, *The Casimir Effect in Critical Systems*, World Scientific, Singapore,

1994.
[203] J.W. Cahn, *J. Chem. Phys.* **66**, 3667 (1976).
[204] M. Schick, Introduction to wetting phenomena, in *1988 Proceedings of the Les Houches Summer School Lectures, Session XLVIII*, edited by J. J. J. Charvolin and J. Zinn-Justin, p. 416, Elsevier, Amsterdam, 1990.
[205] K. Binder, D. Landau, and M. Müller, *J. Stat. Phys.* **110**, 1411 (2003).
[206] R. Evans, U. Marini Bettolo Marconi, and P. Tarazona, *J. Chem. Phys.* **84**, 2376 (1985).
[207] R. Evans and U. Marini Bettolo Marconi, *J. Chem. Phys.* **86**, 7138 (1987).
[208] R. Evans, *J. Phys.: Condens. Matter* **2**, 8989 (1990).
[209] T. Bieker and S. Dietrich, *Physica A* **252**, 85 (1997).
[210] R. Evans, R. Roth, and P. Bryk, *Europhys. Lett.* **62**, 815 (2003).
[211] M.C. Stewart and R. Evans, *Phys. Rev. E* **71**, 011602 (2005).
[212] R.J.F. Leote de Carvalho, R. Evans, D.C. Hoyle, and J.R. Henderson, *J. Phys.: Condens. Matter* **6**, 9275 (1994).
[213] R. Evans and J.R. Henderson, *J. Phys.: Condens. Matter* **21**, 474220 (2009).
[214] C. Bauer, T. Bieker, and S. Dietrich, *Phys. Rev. E* **62**, 5324 (2000).
[215] A.J. Archer and R. Evans, *J. Chem. Phys.* **118**, 9726 (2003).
[216] P. Hopkins, A.J. Archer, and R. Evans, *J. Chem. Phys.* **131**, 124704 (2009).
[217] N. Goldenfeld, *Lectures On Phase Transitions And The Renormalization Group*, Westview Press, 1992.
[218] J.D. van der Waals, *Over de Continuiteit van den Gas- en Vloeistoftoestand*, PhD thesis, Leiden University.
[219] N.F. Carnahan and K.E. Starling, *J. Chem. Phys.* **51**, 635 (1969).
[220] H. Reiss, H.L. Frisch, and J.L. Lebowitz, *J. Chem. Phys.* **31**, 369 (1959).
[221] E.A. Mastny and J.J. de Pablo, *J. Chem. Phys.* **127**, 104504 (2007).
[222] R. Car and M. Parrinello, *Phys. Rev. Lett.* **55**, 2471 (1985).
[223] H. Löwen, P.A. Madden, and J.P. Hansen, *Phys. Rev. Lett.* **68**, 1081 (1993).

Summary

Colloids are nano to micrometer aggregates of atoms and molecules suspended in a solvent. Since they are permanently subject to collisions with the thermally agitated solvent molecules, colloids diffuse following random trajectories (Brownian motion). Thanks to their solvent-induced motion, macroscopic many-particle systems of colloids can be studied by means of *statistical mechanics*. Similarly to atoms and molecules, colloids appear in extremely different thermodynamic phases, such as gas, liquid, crystals and liquid crystals. However, the mutual interactions between colloids can be tailored with much more freedom than those between atoms and molecules. This gives rise to the much wider variety of macroscopic phases colloids develop.

This thesis focuses on the equilibrium thermodynamics of suspensions of *anisotropic* colloids, that is, colloids with a marked non-spherical shape. The mutual interactions between non-spherical particles are anisotropic and explicitly dependent on the orientations of the colloids in space. Under these circumstances, phases otherwise not observable are expected. In particular, these phases are identified with the peculiar type of ordering in space that colloids assume, or, in more technical terms, with their degree of spontaneous *symmetry breaking*. The aim of this thesis consists of describing and understanding various aspects of the symmetry-broken phases generated by anisotropic colloids: the conditions for *phase transitions*, the character of the equilibrium *diffusion*, and the features of different *effective interactions*. The bare interactions between colloids are modeled as hard anisotropic repulsions. Besides reproducing experimental conditions common in colloid science, hard-particle models have gained a primary role in liquid-state theory. In fact, steep repulsive interactions allow us to investigate the many-body behavior of a system in purely entropic terms, that is, independently of energy. Our study is based on the application of equilibrium classical statistical mechanics in the formulations of *Density Functional Theory* and *Monte Carlo simulation*.

We start in Chapter 3 by addressing one of the most controversial questions in liquid-crystal science: do stable biaxial nematic phases exist? Like the common

uniaxial nematic, the biaxial nematic is a liquid-crystal phase which is homogeneous, but anisotropic, as a consequence of the preferred orientations its particles assume. Due to the higher orientational ordering with respect to uniaxial nematics, the biaxial nematic phase is expected to manifest peculiar optical properties associated with biaxial birefringence. Our analysis is inspired by recent experiments on a suspension of colloids with the shape of bricks (a.k.a., boardlike particles), where a surprisingly stable biaxial nematic phase was observed. In order to interpret these puzzling results, we develop a density functional theory based on discrete orientations (Zwanzig model) to study the effect of polydispersity on the phase behavior of hard boardlike particles. We start from the simplest polydisperse system, namely a binary mixture of big and small boardlike particles. We show that under specific conditions such a size asymmetry leads to the appearance in the phase diagram of two Landau critical points, and a consequent opening-up of the biaxial nematic stability regime. Moreover, we show that a similar effect develops when size polydispersity is modeled more faithfully. Finally, we give quantitative predictions that are compatible with the experimental data.

The problem of the biaxial-nematic stability is addressed in Chapter 4 under a rather different perspective. We study the effect of adding a non-adsorbing depletant to a suspension of boardlike particles. In such a situation the depletant induces an effective attraction between boardlike colloids, whose intensity can be adjusted via the depletant concentration. Following a density functional theory approach similar to that of Chapter 3, we calculate the phase diagram of monodisperse boardlike particles as a function of the concentration of the depletant. Modeling the depletant as a collection of non-mutually-interacting hard cubes allows us to analytically calculate the board-board effective interaction. We show that the non-adsorbing depletant can lead to an increased stability of biaxial nematics. More surprisingly, our results share many similarities with those deduced in Chapter 3. This allows us to furnish a clear explanation for the entropic mechanism behind polydispersity-induced biaxial nematic stability.

In Chapter 5 we study the crystallization transition (freezing) of parallel hard squares and cubes in two and three dimensions, respectively. We are mainly interested in the theoretical predictions concerning the stability of the crystal against smectic and columnar phases, and their relation with recent simulation and experimental work. Our density functional theory is based on the fundamental measure theory, the best available theoretical framework for inhomogeneous hard-sphere phases. We confirm previous work about the presence of a vacancy-rich freezing transition in hard-cubes systems. On the other hand, our predictions for the phase behavior of hard squares appear to be far more controversial. In fact, in between the low-density fluid and the high-density crystal our theory predicts a smectic phase, which is however expected to be unstable due to equilibrium fluctuations. We can therefore highlight an important limit of the theory in describing low-dimensional systems. Although various qualitative features of the two models are well described, work in improving the quantitative predictions of the theory is still needed.

We focus in Chapter 6 on the equilibrium dynamics of colloidal liquid crystals.

More specifically, we study a system of parallel colloidal rods, that is known to manifest a nematic-columnar phase transition. The transition to the columnar phase is associated with the alignment of the rods along one-dimensional columns, which are themselves distributed on a two-dimensional hexagonal lattice (columnar plane). The diffusive single-particle dynamics in the presence of nematic and columnar ordering is reproduced by means of a Monte Carlo simulation algorithm. Due to the columnar ordering, the diffusion of the particles in the columnar plane develops in quasi-quantized steps. This gives rise to a microscopic heterogeneous dynamics, which is interpreted in terms of permanent and temporary dynamic "cages". We characterize such a heterogeneous dynamics by measuring the non-Gaussian properties of the diffusion and the non-exponential features of the structural relaxation.

Finally, we study in Chapter 7 the solvent-mediated interactions between colloids. Manipulating the effective interactions between colloids by means of a change in temperature is a simple yet practical way to reversibly control colloidal self-assembly. Capillary-condensation forces constitute an example of such thermosensitive interactions. These type of forces arise when the solvent of a suspension is composed by two species with different adsorption affinities with the surface of the colloids. The main problem associated with these interactions is due to the fact that their quantitative description involves a complicated and time-consuming numerical process. We propose a simplified theory aimed at capturing the essential physics of the problem, while reducing its numerical complexity to the lowest terms. We analyze the outcome of our minimalist theory in the planar geometry and compare its results with those of more refined theoretical approaches. Although strong limitations appear while considering temperatures close to the solvent critical point, we show our approach to be more than satisfying. This suggests that our method could allow for the study of more complex and less investigated geometries.

Samenvatting

Colloïden zijn aggregaten van atomen of moleculen ter grootte van een nanometer tot een micrometer en worden vaak bestudeerd in een oplosmiddel. Door botsingen met de oplosmiddelmoleculen bewegen deze deeltjes zich voort langs willekeurige paden of trajectoriën, een proces dat bekend staat als Brownse beweging. Deze eigenschap maakt het mogelijk om de macroscopische veel-deeltjes eigenschappen van de colloïden te beschrijven met methoden uit de *statistische mechanica*. Hiermee kan een rijk scala aan thermodynamische fasen worden beschreven waarin de colloïden zich kunnen bevinden: denk hierbij aan een gas, vloeistof, kristal of vloeibaar kristal. Dit zijn allemaal fasen die ook voorkomen in atomistische of moleculaire systemen, maar het essentiële verschil is dat de onderlinge wisselwerkingen tussen de colloïden met veel meer vrijheid kunnen worden gemanipuleerd. Dit maakt het macroscopische fasegedrag erg rijk en divers, zoals we ook in deze dissertatie zullen zien.

In dit proefschrift wordt de nadruk gelegd op de thermodynamische eigenschappen van colloïdale suspensies in evenwicht. De deeltjes die we gaan onderzoeken zijn anisotroop, en kunnen dus in tegenstelling tot bollen verschillende voorkeursrichtingen aannemen. Deze anisotropie uit zich bovendien in de onderlinge interacties van de colloïden, die dus expliciet van de oriëntatie afhangen. Het fasegedrag is hierdoor erg anders dan in systemen bestaande uit bolvormige deeltjes, omdat er meer vrijheid is om bepaalde symmetrieën spontaan te breken of te behouden. Hierdoor zijn diverse ruimtelijke en orientationele ordeningen mogelijk die gekarakteriseerd kunnen worden aan de hand van hun symmetrie ten opzichte van de wanordelijke fase. Het doel van deze dissertatie is dan ook om deze verschillende aspecten in het fasegedrag van anisotrope colloïden te beschrijven en te begrijpen. We zullen hierbij niet alleen de aandacht vestigen op de condities waarop de *faseovergangen* plaatsvinden, maar we gaan ook kijken naar de *diffusie* van de deeltjes in evenwicht. Tot slot onderzoeken we de verschillende aspecten van de *effectieve interacties*. Hierbij starten we met harde, anisotrope repulsies om te bekijken welke effectieve interacties hieruit voortvloeien. Dit is van belang omdat harde interacties vaak voorkomen in experimenten binnen de colloïdale wetenschappen. Ook is het van fundamenteel belang omdat dit soort interacties vaak wordt bestudeerd in de

theorie van vloeistoffen. Als de repulsieve interacties sterk genoeg zijn, wordt het zelfs mogelijk om de veel-deeltjes eigenschappen te beschrijven met slechts entropische bijdragen en deze hangen dus niet af van de energie. Om dit te bewerkstelligen gebruiken we verschillende methoden uit de statistische mechanica, zoals klassieke *dichtheidsfunctionaaltheorie* en *Monte Carlo simulaties*.

In hoofdstuk 3 starten we met een erg controversieel probleem binnen het vakgebied van de vloeibare kristallen. We vragen ons namelijk af of stabiele, biaxiale nematische fasen bestaan. Net zoals de wellicht bekendere uniaxiale nemaat, is deze fase anisotroop en homogeen. De anisotropie is hier het gevolg van de deeltjes die door hun vorm verschillende voorkeursrichtingen kunnen aannemen. Doordat er meerdere mogelijkheden zijn om de deeltjes in een bepaalde richting op te lijnen is er biaxiale dubbelbrekendheid en hierdoor zijn de optische eigenschappen exotischer dan in de uniaxiale nematen. In ons onderzoek laten we ons voornamelijk inspireren door recente experimenten aan colloïdale suspensies bestaande uit deeltjes met de vorm van een baksteen (de zogenaamde bordachtige deeltjes), waar verrassend genoeg stabiele, biaxiale nematische fasen zijn waargenomen. Om dit bijzondere resultaat te interpreteren hebben we een dichtheidsfunctionaaltheorie ontwikkeld waarbij de deeltjes slechts enkele, discrete oriëntaties kunnen aannemen (het zogenaamde Zwanzig model). Deze passen we vervolgens toe om de invloed van polydispersiteit te onderzoeken op het fasegedrag van deze harde deeltjes. Eerst beginnen we met het meest simpele systeem, namelijk een binair mengsel van grote en kleine bordachtige deeltjes. Onder specifieke omstandigheden, zoals een asymmetrie in grootte, verschijnen er twee Landau kritieke punten in het fasediagram. Deze gaan vervolgens over in een regime waarin de biaxiale nemaat stabiel is. We vinden een vergelijkbaar resultaat als we polydispersiteit explicieter meenemen in ons model. Het hoofdstuk wordt afgesloten met kwantitatieve voorspellingen die consistent zijn met de experimentele data.

De vraag of een biaxiale nemaat stabiel is, wordt vanuit een ander oogpunt beschreven in hoofdstuk 4. We beschrijven hier het effect van een niet-adsorberend depletant in een suspensie van bordachtige deeltjes. Onder deze omstandigheden induceert het depletant een effectieve interactie tussen de bordachtige deeltjes, waarvan de sterkte afhankelijk is van de concentratie van deze stof. Door een vergelijkbare dichtheidsfunctionaaltheorie te gebruiken als in hoofdstuk 3, wordt het fasediagram van monodisperse, bordachtige deeltjes in kaart gebracht als functie van de depletantconcentratie. Het depletant wordt hierbij gemodelleerd als een verzameling van kubussen die onderling niet wisselwerken, waardoor het mogelijk wordt om de effectieve interacties tussen twee bordachtige deeltjes analytisch uit te rekenen. We laten zien dat het niet-adsorberende depletant kan leiden tot een hogere stabiliteit van de biaxiale nematische fase. Deze resultaten hebben veel eigenschappen gemeen met de bevindingen uit hoofdstuk 3 en hierdoor kunnen we het entropisch mechanisme uitleggen waarom biaxiale nematen gestabiliseerd worden door polydispersiteit.

In hoofdstuk 5 beschrijven we het kristalliseren, ofwel het bevriezen, van parallele harde vierkanten en kubussen in respectievelijk twee en drie dimensies. Hierbij zijn

we voornamelijk geïnteresseerd in de stabiliteit van de kristallijne fase ten opzichte van de smectische en/of columnaire fasen en we vergelijken onze resultaten met die van experimenten en simulaties. We gebruiken een dichtheidsfunctionaaltheorie gebaseerd op fundamentele maattheorie, één van de best beschikbare methoden om inhomogene fasen van harde bollen te beschrijven. Door dit formalisme toe te passen vinden we een kristallisatieovergang van harde kubussen die al bekend is in de literatuur, waarbij het kristallijne rooster rijk is aan vacatures. De voorspellingen voor het fasegedrag van harde vierkanten zijn echter controversiëler. Hier vinden we tussen het regime van een vloeistof met een lage dichtheid en een kristal met een hoge dichtheid een smectische fase die instabiel is onder evenwichtsfluctuaties. Hieruit kunnen we concluderen dat we ons model niet altijd kunnen toepassen op laagdimensionale systemen. Desalniettemin zijn we wel in staat om de verscheidene kwalitatieve eigenschappen van de twee modellen te beschrijven, maar deze zijn zeker nog niet kwantitatief.

Het onderwerp van hoofdstuk 6 is de dynamica van colloïdale vloeibare kristallen in evenwicht. Hierbij beschouwen we een systeem van parallele colloïdale staven, dat een faseovergang kan ondergaan van een nematische naar een columnaire fase. De overgang naar de columnaire fase wordt gekarakteriseerd door een oplijning van staven langs ééndimensionale kolommen, die zich onderling ordenen in een tweedimensionaal, hexagonaal rooster (het columnaire vlak). We reproduceren de diffusieve ééndeeltjesdynamica in de aanwezigheid van nematische en columnaire ordening met behulp van Monte Carlo simulaties. Door de columnaire ordening wordt de diffusie van deeltjes beschreven in termen van quasi-gekwantiseerde stappen. Dit geeft aanleiding tot een microscopische, heterogene dynamica, die we kunnen interpreteren in termen van permanente en tijdelijke dynamische "kooien". Deze heterogene dynamica karakteriseren we met behulp van niet-Gaussische eigenschappen van het diffusieve gedrag en de niet-exponentiële karakteristieken van de structurele relaxaties.

In het laatste hoofdstuk beschrijven we interacties tussen colloïden die ontstaan door de aanwezigheid van een oplosmiddel. Door middel van veranderingen in de temperatuur is het erg makkelijk en praktisch om op een reversibele manier colloïdale zelfassemblage te beïnvloeden in dit soort systemen. Een voorbeeld van dit type interacties is de zogenaamde capillaire condensatiekracht in colloïdale suspensies. Deze krachten komen voor als het oplosmiddel bestaat uit twee typen deeltjes met elk een andere affiniteit om op een colloïdaal oppervlak te adsorberen. Het vergt echter veel tijd om dit type interacties kwantitatief te beschrijven met behulp van bestaande numerieke algoritmen. We kiezen daarom voor een simpele theorie die slechts de essentiële fysica bevat, zodat de numerieke complexiteit minimaal is. Deze minimale theorie passen we vervolgens toe op een vlakke geometrie en de resultaten worden vergeleken met bestaande, complexere modellen. Ondanks het feit dat we sterke beperkingen van onze theorie verwachten nabij het kritieke punt van het oplosmiddel, zien we toch dat onze resultaten erg bevredigend zijn. We hopen daarom dat onze methode ook gebruikt kan worden in het bestuderen van complexere geometrieën die nog niet vaak zijn onderzocht.

Acknowledgements

Even though within a PhD program only the candidate gets the degree, the work and energy of many more people contribute to the final result. Therefore, I cannot accept this degree without acknowledging all those people who, by leading, supporting, suggesting, criticizing, amusing and loving me, brought me here.

First of all, there is no PhD student without PhD advisors. My deepest gratitude goes to Marjolein and René. Working with you during the last four years has been a pleasure and an honor. There is no doubt that if I can call myself a scientist, I largely owe it to you and everything I learned from (and with) you. However, what you taught me goes far beyond science, but unfortunately there aren't enough pages in a PhD thesis to include that.

Many thanks to all the people of the Institute for Theoretical Physics, in particular to all the professors who keep its research at the top international level: you have made me proud to be one of its members. I would like to acknowledge those working behind the scenes, without whom nothing could work: Joost, Olga, Els, Marion, Riny. Additionally, I would like to thank Rembert Duine for the beautiful course of Statistical Field Theory. A warm thanks also to Bob Evans for the precious insights on liquid-state theory given while occupying the Kramers chair.

During this four years I had the pleasure to work in close contact with the Soft Condensed Matter group of the Debye Institute for Nanomaterials Science. The high-level experimental research led by Alfons van Blaaderen and Arnout Imhof determined the ideal environment for me to learn what colloids, and more in general soft matter, actually are. For the many lessons, I am deeply thankful to both of them and all their collaborators. For the intense scientific exchange I would also like to acknowledge the Physical and Colloid Chemistry group, and in particular Gert Jan Vroege, with whom I had the pleasure to collaborate.

Thanks to the colleagues of the ITF, with whom I shared most of the challenges of the PhD life: the Soft Matter buddies Niels, Thomas, and Beppe; Jildou for the fun experience of the SFT teaching assistantship; Marcolino for the time spent in the vain attempt of learning Dutch; Chiara for helping organizing the PLaneTs;

the officemates Dima, Maarten, and Clement; Eric, Jan, Jogundas, Vivian, Joris, Ralph, Jasper, Riccardo, Anne, Drazen, Ivano, Alessandro, Wilke, Stijn, Chris, Pietro, Roberto. Special thanks to Jeffrey for translating the summary of this thesis *in het Nederlands*. Thanks also to all the colleagues of the SCM group: Anjan, Marlous and Nina for the coolest summer school ever; the fellow immigrants Simone and Guido, with whom it's impossible to miss Italy; John, Ran, Doug, Frank and Laura for the precious scientific inputs; Jissy, Thijs, Bo, Joost, Bart, Rao, Bas, Kristina, Marjolein, Teun, Henriette, Wessel, Weikai, Wiebke, Johan, Jamal, Peter, Judith. Thanks to Ale Patti for the good old times. From each one of you I learnt something: thanks for that!

I am deeply indebted to Giorgio Pastore, who introduced me to colloid physics, referred me to the Utrecht group and sponsored me for the "Fontana" prize.

Un pensiero alla ghenga di amici italiana, grazie a cui il tempo che passa sembra solo un'illusione. Grazie agli amicozzi tuen-clesiani Ale e Met, alla Ba, al Rudi e alla Martina, alla Lisa, al Miguel, al Pasto. Grazie alla Dina: superyeah!! Grazie alla Elenotti, sempre vicina. Grazie a Sandro, Antonio e Roberta, perché se trasferirsi a Trieste è valso a qualcosa, lo è stato a conoscere voi, e a Giova, perché in fondo la nebbia in casa mi manca. Grazie al Puppo per il gran week end berlinese.

Thanks to all the people I hung out with in Utrecht. It could have been a warm living room or a freezing night along a canal. It was still a lot of fun. Thanks to all my house mates, which have never made me feel bored. Thanks to Ricardo, Diana, Fra, Zhao Yue (and Ole), and Thomas. Even to Carl, thanks. I am thankful with Daniel twice: for his friendship and for his friends' friendship ;) And thanks to the lovely Tianji, *cuore di nonna*. Thanks to Pat, because it's a lot of fun every time.

I would like to address a special acknowledgement to Sue and Peter, for the warm welcome into their family, as much as for the best holiday ever!

Grazie infine alla mia famiglia, il cui supporto incondizionato non mi è mai mancato. Grazie alla big sis *Roberta, la cui forza e carattere sono semplicemente un esempio costante. Grazie ai miei vecchi, Guido e Dina, perché vi devo tutto quello che ho.*

Finally, for your love, the only thing I really need: thanks Kat.

About the author

Simone Belli was born in Cles (Trento, Italy) on April 2nd 1985. After completing high school in Cles, he moved to Trieste. At the University of Trieste he received a Bachelor in 2007 and a Master in Physics in 2009, the latter after discussing a thesis on the integral-equations theory for liquids under the supervision of Prof. G. Pastore. In 2009 he started a PhD in Physics at Utrecht University under the supervision of Prof. M. Dijkstra and Prof. R. van Roij. His research focused on the theoretical description of colloidal suspensions and is exposed in this thesis. He presented his work to the scientific community in both national and international conferences, while publishing his results in peer-reviewed journals. For his work on biaxial nematic liquid crystals he received in 2012 the "M. Fontana" prize for young researchers in Soft Matter awarded by the Italian Physical Society.

Publications

This thesis is partly based on the following publications.

S. Belli, M. Dijkstra, and R. van Roij
Free Minimization of the Fundamental Measure Theory Functional: Freezing Transition of Parallel Hard Squares and Cubes
The Journal of Chemical Physics **137** 124506 (2012)
(Chapter 5)

S. Belli, M. Dijkstra, and R. van Roij
Depletion-induced Biaxial Nematic States of Boardlike Particles
The Journal of Physics: Condensed Matter **24** 284128 (2012)
(Chapter 4)

S. Belli, A. Patti, M. Dijkstra, and R. van Roij
Polydispersity stabilizes Biaxial Nematic Liquid Crystals
Physical Review Letters **107** 148303 (2011)
(Chapter 3)

S. Belli, A. Patti, R. van Roij, and M. Dijkstra
Heterogeneous Dynamics in Columnar Liquid Crystals of Parallel Hard Rods
The Journal of Chemical Physics **133** 154514 (2010)
(Chapter 6)

Other publications by the author.

A. Patti, S. Belli, R. van Roij, and M. Dijkstra
Relaxation Dynamics in the Columnar Liquid Crystal Phase of Hard Platelets
Soft Matter **7** 3533 (2011)

R. Ni, S. Belli, R. van Roij, and M. Dijkstra
Glassy Dynamics, Spinodal Fluctuations, and the Kinetic Limit of Nucleation in Suspensions of Colloidal Hard Rods
Physical Review Letters **105** 088302 (2010)